Influence of the Architecture and Interfaces in Perovskite Solar Cells

José Ignacio Uribe

Supervisors:
Prof. Jaime Osorio, Prof. Franklin Jaramillo

Submitted this Thesis in partial fulfillment of the requirements for the degree of
Doctor in Physics

Universidad de Antioquia
Facultad de Ciencias Exactas y Naturales
Instituto de Física
Medellín
2017

Abstract

Perovskite solar cells (PSCs) have reached a surprising high performance in the last few years due to the large research effort. Some of this effort has focused on optimizing the architecture, selective layer properties, and the interaction between the different components of the cell. Nevertheless, the effect of the architecture and selective layers on some physical properties of the perovskite itself, and in the complete cell has not been completely understood. Moreover the improvement of the carrier dynamics at the interface and through different surface treatment is one most interesting topic in the PSCs community.

In this work, I present a study of the influence of the architecture, selective layers, and interfaces treatments in metal halide PSCs.

In order to analyze the influence of the architecture and different selective contacts, first it was implemented different hole transporting layers (HTL). To do that, was studied the influence of nickel oxide (NiO_x), copper thiocyanate (CuSCN) and copper oxide (CuO_x) in a planar structure. The PSCs with NiO_x presented superior performance than the PSCs with CuO_x and CuSCN. Their performance (solar cells with CuSCN and CuO_x) was similar to the cells without HTL. The low photovoltaic response of the cells with CuO_x CuSCN as HTL was due to poor morphology, bad transport properties, and deficient band alignment with perovskite. In another way, the band alignment, high coverage area, and good morphology make the cells fabricated with NiO_x superior.

Afterward differences in the band bending and work function of the perovskite as is grown on NiO_x in planar architecture or NiO_x-Al_2O_3 in a mesoporous configuration were obtained. A facet dependence on the photoluminiscence (PL) and lifetime of the charges through Scanning Intensity modulated kelvin probe microscopy (IM-KPFM) was obtained.

The influence of the surface modifications in selective layers in perovskite solar cells were worked in three cases.

In first instance the role of rhodamine interface between the 61-butyric acid methyl ester (PCBM) and the Ag electrode was carefully studied. Through kelvin Probe force microscopy (KPFM) was found a flattening of the PCBM surface after rhodamine treatment, and a change in the Ag electrode work function after its interaction with the rhodamine. As a consequence the fill factor (FF) and the short circuit current (Jsc) increase and the performance of the cells was improved.

As another example of interface modification, a nanoparticle-based solution-processed TiO_2 layer (TiO_2-NP) was implemented. I studied the influence of TiO_2- PCBM treatment in a n-i-p solar cell. Through SKPFM I found a band bending present in an p-i-n structure without PCBM which means that TiO_2-NP layer does not block the holes in the film due to pinholes in the films, meanwhile after the PCBM treatment the band bending changes the direction, and the performances of the PSCs is improved significantly.

Additionally, I analyzed the influence of MACl treatment in a scalable process for perovskite fabrication based on the acetonitrile crystallization route (ACN). Using surface photovoltage (SPV) was studied the change in morphology and electronic properties of the ACN perovskite when MACl treatment is implemented. I found that after MACl treatment, grain size changes, and a passivation of the boundaries under illumination, moreover the PL response is clearly superior with MACl, proving the increase of the radiative recombination, and a decrease of trap states assisted recombination. Those results explain the improvement of all the photovoltaic parameters and performance of the PSCs when the perovskite is fabricated through the ACN route under MACl treatment.

Agradecimientos

Esta tesis doctoral se realizó en el marco del proyecto 2013000100184 del sistema general de regalías titulado *Celdas solares nanoestructuradas: desarrollo y aplicación de las tecnologías en escuelas no interconectadas o de intermitencia energética del departamento de Antioquia* .

Este trabajo de investigación no hubiera sido posible sin la ayuda de muchas personas. Le agradezco de gran manera a los profesores Jaime Osorio, y Franklin Jaramillo quiénes me han guiado en todo este proceso, me ha brindado una gran cantidad de enseñanzas que no sólo me han ayudado a crecer como profesional si no como persona. A los compañeros del laboratorio de celdas solares (Rafael betancur, Juan Felipe Montoya, Mario Mejía, John Ciro, Jhony Jaramillo, Santiago Mesa, Juan Felipe Tirado y Daniel Ramirez) quienes me han ayudado en todos los procesos, discusiones y trabajo de laboratorio. También agradezco a los compañeros del instituto de física y del grupo de estado sólido, particularmente a Marcos por las discuciones realizadas. También a los profesores del grupo de Estado sólido particularmente a Jorge Mario Osorio.

A los compañeros en el Ginger-Lab quienes me acogieron en el proceso de pasantía y especialmente a Raj y al profesor David Ginger por las enseñansas en todas las técnicas relacionadas con microscopía de Fuerza Atómica. Quisiera también agradecer de gran manera a los evaluadores de este trabajo (Juan Pablo Correa , Cristina Roldán y Katherine Gross), quienes con sus observaciones y sugerencias han hecho que se mejore y enriquezca profundamente.

Mis padres y hermanos han sido el soporte emocional en días difíciles, y me han apoyado en todas mis decisiones, a mis sobrinos que me han alegrado mis días, a Sharira qué es mi compañia y mi soporte y que me ha aguantado todos los momentos.

Contents

List of Figures

List of Tables

Abbreviations

PSC	**P**erovskite **S**olar **C**ell
AFM	**A**tomic **F**orce **M**icroscopy
KPFM	**K**elvin **P**robe **F**orce **M**icroscopy
SPV	**S**urface **P**hoto **F**voltage
IMKPFM	**I**ntensity **M**odulated **K**elvin **P**robe **F**orce **M**icroscopy
ACN	**AC**etoN**i**trile
HTL	**H**ole **T**ransporting **L** ayer
ETL	**E**lectron **T**ransporting **L** ayer
TC	**T**ransparent **C**onductor
PCE	**P**ower **C**onversion **E**fficiency
EQE	**E**xternal **Q**uantum **E**fficiency
SPO	**S**tabilized **P**ower **O**utput
SCR	**S**pace **C**harge **R**egion
SE	**S**olvent **E**ngineering

Dedicado a mis padres, Sharira y Agustín

List of Publications

1. John Ciro, Santiago Mesa, **José Ignacio Uribe**, Mario Alejandro Mejía-Escobar, Daniel Ramirez, Juan Felipe Montoya, Rafael Betancur, Hyun-Seok Yoo, Nam-Gyu Parkc, and Franklin Jaramilloa. *Optimization of the Ag/PCBM interface by Rhodamine interlayer to enhance efficiency and stability of perovskite solar cells.* Nanoscale. Vol 9, pp 9440-9446,2017.

2. **José Ignacio Uribe**, Daniel Ramirez,Jorge Mario Osorio-Guillen, Jaime Osorio, and Franklin Jaramillo. *$CH_3NH_3CaI_3$ Perovskite: Synthesis, Characterization, and FirstPrinciples Studies.*The jornal of Physical Chemestry C. Vol 120, pp 16393-16398, 2017

3. John Ciro, Santiago Mesa, Juan Felipe Montoya, **José Ignacio Uribe**, Rafael Betancur, and Franklin Jaramillo. *Simultaneous Top and Bottom Perovskite Interface Engineering by Fullerene Surface Modification of Titanium Dioxide as Electron Transport Layer.* ACS Applied Materials and Interfaces. Vol 9, pp 29654-29659, 2017

4. **José Ignacio Uribe**, John Ciro, Juan Felipe Montoya, Jaime Osorio, and Franklin Jaramillo. *Enhancement of morphological and optoelectronic properties of perovskite films by CH_3NH_3Cl treatment for efficient solar mini-modules.* ACS Applied Energy Materials. Vol 1 (3), pp 1047-1052, 2018

5. Daniel Ramirez, **José Ignacio Uribe**, Luca Francavigliac, Pablo Romero-Gomezc, Anna Fontcuberta, and Franklin Jaramillo. *Photophysics behind High Luminescent Two-dimensional Hybrid Perovskite (CH3(CH2)2NH3)2(CH3NH3)2Pb3Br10 thin films.* Accepted Journal of Materials Chemistry C

q

Chapter 1

General Introduction

This chapter is divided into three sections. In the first one, an overview of the perovskite technology in the framework of the photovoltaic generations is presented. Afterward, is included a brief overview of the metal halide perovskite structure and their physical properties. Moreover a description of the PSCs, their basic physic operation, and a description of the different configuration and structures of PSCs is exposed. The last part of this introduction summarizes the contents of the other chapters of this Thesis.

1.1 Perovskite into the Photovoltaic Technologies

Since the emergence of the first solar cell in 1954 different materials and photovoltaic technologies have been developed [1]. Due to differences in structure and fabrication methods the photovoltaic technologies have been divided in generations.

The first generation is related to solar cells made by highly crystalline materials (with very low density of electronic and crystal defects, which can affect dramatically the transport properties) as monocrystalline, polycrystalline silicon and the GaAs family. The processing of these kind of materials requires high temperature, ultra high vacuum process and specific clean rooms to produce extremely high quality materials. Currently, most manufactured solar cells are based on multicrystalline silicon where modest efficiencies of around 10-16 % [2] are compensated by a reduction in manufacturing costs. Contrary multi junctions GaAs based solar cells is the most efficient technology reaching 40 % efficiency, but their high manufacturing cost, make them only useful in satellites (due to the cost is not comparable with of the launching and working cost) [2].

The second generation is related with devices made basically from thin films deposited on substrates by high vacuum processing (physical and chemical vapor deposition process

(PVD and CVD)), some of the technologies are III-V / II-VI semiconductor solar cells, such as $Cu(In,Ga)Se_2$, (CIGS) and amorphous silicon [2], this materials have higher optical absorption coefficient as compared with crystalline semiconductors [3]. Until now efficiencies of 22.6% for laboratory cells have been reached (see Figure 1.1).

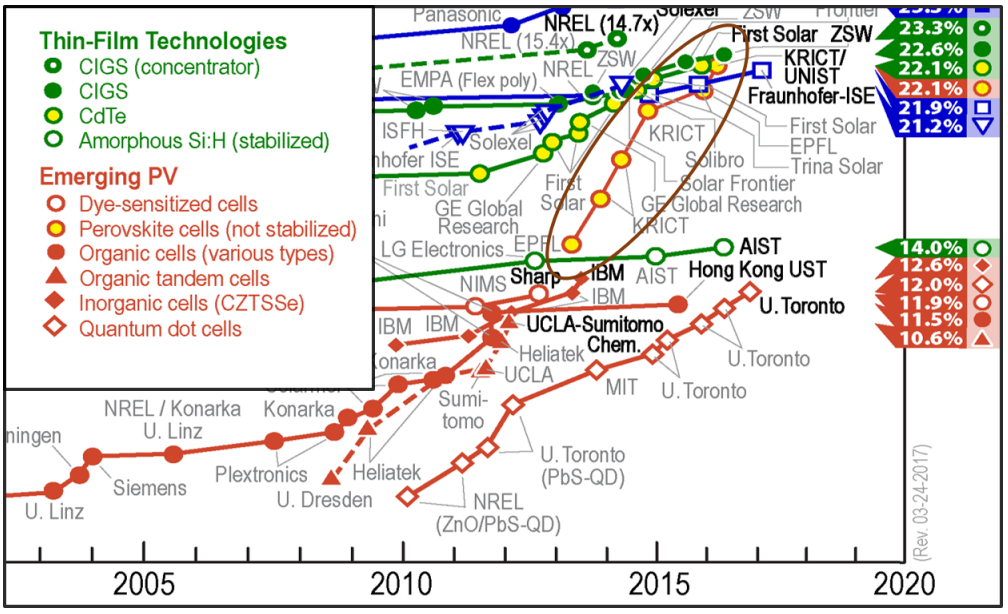

FIGURE 1.1: Solar energy conversion efficiencies for benchmark solar cells from 1976-2016- data assembled by National Renewable Energy Lab, the image is modified to take a zoom for second (Thin film technologies) and third generation (Emerging PV) solar cells

In another way, the progress in solution processing methods has allowed the development of easily processed solar cells (third generation), including, dye-sensitized, small molecule, quantum dot, polymer, and perovskite solar cell [4]. The third generation has attracted a massive increase in research effort over the last 27 years, which has led to tremendous advances in efficiency, reproducibility, and stability, and the first commercial products are being sold in niche markets to power consumer electronics and low-power applications in buildings.

Particularly perovskite solar cells have had an unprecedented development. In only 7 years reached performances as high as 22% [5], making them one of the most promising photovoltaic technologies. The perovskite solar cell technology combines low cost and high efficiency, as a difference of the other third generation solar cells, which until now reach modest efficiencies [6, 7]. In the Figure 1.1 is observed the trend of the perovskite solar cells compared to some second and third generation solar cell. It is very clear the rapid progress of the perovskite respect the other ones [8, 9].

1.2 Metal Halide Perovskites, and Perovskite Solar Cells

Organo-lead-halide perovskite has emerged as the most promising material for photovoltaic solar cell applications [8–10]. The success of this material in photovoltaic applications is due a combination of its extraordinary physical, chemical properties and their easy processing.

Studying their physical properties, and its function in different configuration of solar cells is highly justified. In this section I described the basic physical properties and the general configurations and operational mechanism of perovskite solar cells. Appendix C presents the information about the working principles of a solar cell, and the photovoltaic parameters used to characterize the performance of a solar cell.

1.2.0.1 Metal Halide Perovskites

Perovskites cover a large family of compounds with the general formula ABX_3 [11]. The most extensively studied hybrid perovskite material is $CH_3NH_3PbI_3$ and its analogous mixed-halide formulation $CH_3NH_3PbI_{1-x}Cl_x$ [8–10, 12, 13]. Initially, the term perovskite was used to refer to a calcium titanium oxide mineral with the chemical formula $CaTiO_3$, but as many materials can adopt this structure, it is now used for any material with similar structure [11]. The ideal crystalline structure is cubic, with A and B being two different cations and X an anion (see Figure 1.2). For the case of metal halide perovskite, the A component can be a monovalent organic cation. The most explored until now, have been the Methylammonium CH_3NH_3 and the formamidium CH_5N_2. As the inorganic cation Pb has been more successful than Sn [14–16]. Have been some efforts to try to replace the Pb by other elements like Ca, Ni and Sr [17]. As the anion components the halides I, Cl, Br and their mix have been used in order to tune the band gap in combination with a suitable use of Formamidinium and Methylammonium [18, 19].

Characteristics of Lead Halide Perovskites The great success of the lead triiodide perovskite $CH_3NH_3PbI_3$, the mix (with chlorine) $CH_3NH_3PbI_{3-x}Cl_x$ and their Br counterpart is due their appropriate physical properties. They are direct band gap semiconductors which can be tunable (depending of the halide) between 1.5, 1.8 eV. They have a high absorption coefficient (10^5 cm^{-1}) [20] with a broad spectrum of photoenergy [21] and low binding energy [22]. Their electron/hole diffusion lengths have been measured a to be longer than 100 nm [23, 24]. The electron/hole mobilities are in the order of of 1 - 10 cm^2/Vs [25], which enable a large portion of the photo-excited

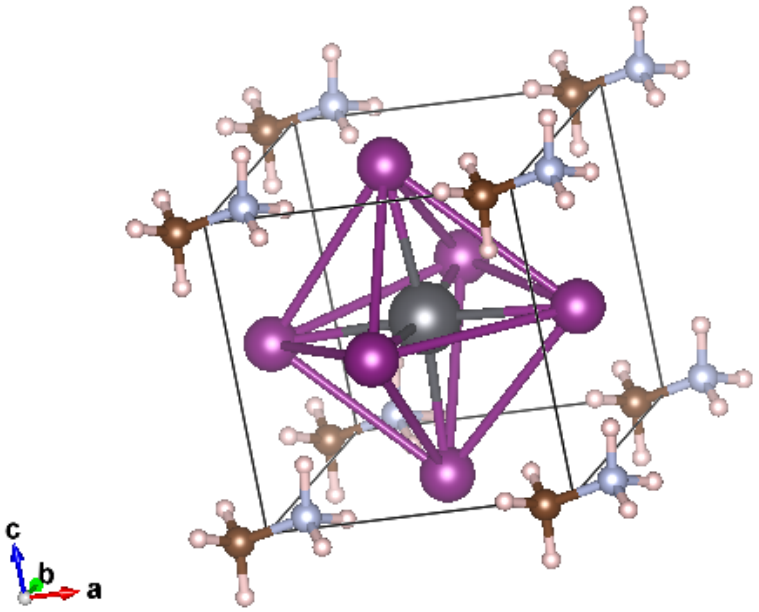

FIGURE 1.2: Crystal structure for $CH_3NH_3PbI_3$. Gray spheres represent Pb atoms; purple, I atoms; brown, C atoms; gray, N atoms; and pink, H atoms.

charge carriers moving to the interfaces between the perovskite and the hole/electron transporting materials (HTM/ETM) and being extracted efficiently, therefore producing sufficiently large photocurrent. Also because its band gap, a high open circuit voltage have been obtained (exceeds 1 eV)[26]. This is particularly interesting because the maximum voltage obtained until now is very near to the maximum value equal to the band gap, but always there is a loss in the voltage as a product of recombination in middle gap states. In the case of perovskite, the type of recombination allows to reduce this kind of losses. All these characteristics makes the perovskite an amazing material for application in photovoltaics.

1.2.0.2 Perovskite Solar Cells

In PSCs different configurations and architectures with similar performances have successfully been improved, indicating the versatility of this technology [8, 9, 27].

PSCs generally consists of several layers: the absorber layer (perovskite), the hole-transporting (HTL), the electron-transporting (ETL), and the electrodes, of which at least one must be transparent see Figure 1.3 and Figure 1.4.

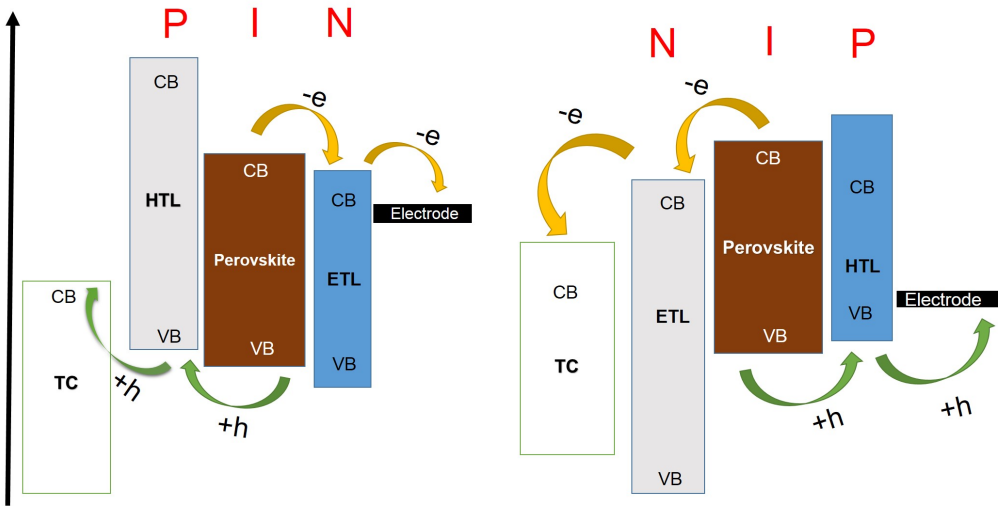

FIGURE 1.3: Band diagram of the perovskite solar cell, left p-i-n structure and in the right is shown the n-i-p structure.

The absorber material is responsible of harvests the light and produce free charges, but having an available charge is a necessary condition, but is not enough to generate photovoltage and photocurrent. A force to carry the charges towards the electrodes is the other condition, this force can be produced by an electric field or thermodynamic force by difference in chemical potentials. In order to get a net current, the electrons must go to one electrode and the holes to the other (in other words should be a direction of the charier transport). To make possible this internal force in the PSCs, selective layers should be included in the device (In this case a Thermodynamic force is established).

HTLs should be materials that have electronic properties that allow the transport of holes in its valence band toward one of the electrodes. Moreover, it should not carry electrons in its conduction band. To do that, the bands of energy should have an adequate bands position. In the Figure 1.3 the minimum of the conduction band of the perovskite should not be higher (in energy terms) that the correspondent of the HTL, and their valence band should be a little higher than the HTL in order to block electrons and receive holes. Moreover, the HTL should have available states in the valence band to transport carriers, and have good mobility to avoid recombination in this layer.

The characteristics of the electron transporting layers should be similar to the HTL, but the main difference lies in the alignment with the perovskite. This layer should receive electrons from the conduction band of the perovskite, to do that, the minimum of the conduction band should be lower that the minimum of the conduction band of the perovskite, and to avoid carry holes from the perovskite, their valence band should be higher than the perovskite see Figure 1.3.

To fabricate PSCs with the layers described above, there have been developed several architectures and configurations of PSCs. They can be planar, infiltrated in a mesostructure, with geometry direct p-i-n, or inverted n-i-p depending of the direction of the current as shown in Figure 1.3.

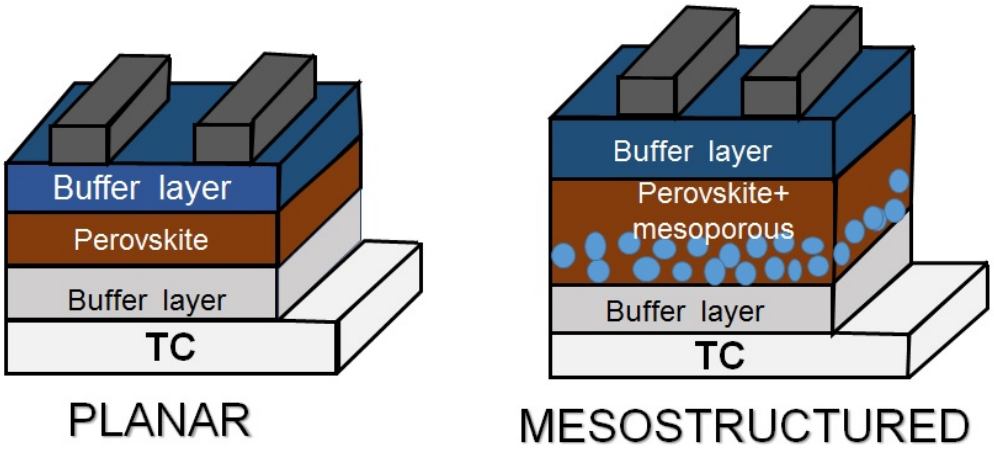

FIGURE 1.4: Characteristic structures of perovskite solar cells.

In a mesostructured architecture, a layer that serves as a scaffold for the perovskite is implemented. The most common scaffolds have been the mesoporous layer of TiO_2 and Al_2O_3. The last one is an insulator and does not take part in the carrier transport, but has an influence in the perovskite growing, electronic properties and help to avoid shunt paths [25, 28, 29]. Moreover, the influence of this mesoporous layers in local properties of the perovskite and additional changes in its electronic behavior is still under development.

Either planar or mesostructured perovskite, p-i-n and n-i-p configurations could be designed. p-i-n means that the perovskite is grown on a HTL that usually is a p-type semiconductor, a n-type semiconductor is grown on the perovskite and to complete the structure a back contact is used. In another way in the n-i-p configuration the perovskite is grown on the ETL and the hole transporting layer is grown on the perovskite. However, many groups have developed PSCs without HTLs or ETLs and have obtained good photovoltaic response. [30].

All these structures have reached high PCE performances [30]. The good performance of the PSCs depends of the physical-chemical characteristics of the HTL, ETL, perovskite film, and their interaction. In many cases to get better interaction between the layers interface treatments should be necessary. In this work we studied the influence of different layers, structures and their interface treatments in perovskite solar cells.

1.3 This Work

The main results of this work are presented in the chapters 2 and 3, and there are 3 Appendix of additional and supplementary information that can help to the reader in the basic concepts treated in this work.

In chapter 2 is analyzed the influence of hole transporting layers and the structure in the microstructure of the perovskite $CH_3NH_3PbI_3$ and how this produces different photovoltaic parameters and performances. As buffer layers we used nickel oxide NiO_x, copper oxide CuO_x and copper thiocianate CuSCN. Moreover is showed through functional scanning probe techniques changes in the surface and sub gap recombination process of the $CH_3NH_3PbI_3$ in three configurations: Hole-free (perovskite grown on top of ITO), planar p-i-n with NiO_x as a hole transporting layer (HTL) and a mesoporous p-i-n with two Al_2O_3 different thickness (100 and 200 nm). Through surface photo voltage, intensity-modulated kelvin probe force microscopy and local photoluminescence we showed the effect of the architecture (configurations) in the surface properties and recombination process. Was found an improve in the stability of the emission with the local photoluminescence images and a decrease in the intensity modulate rate recombination times when a mesoporous structure is included.

In chapter 3 was studied in a deep fashion through AFM techniques the influence of surface in the interface treatment in perovskite solar cells, particularly 3 cases were analyzed:

- Influence of the rhodamine as PCBM-Ag interface in a p-i-n structure.
- PCBM as a interface treatment of TiO_2 layer in a n-i-p structure.
- MACl as a surface treatment in acetonitrile perovskite solar cell.

Next we describe shortly these 3 cases (sections) worked in this chapter.

In the first case was analyzed through AFM, KPFM, SPV and PL measurements the effective control of the interface between the metal cathode and the electron transport layer ETL because is critical for achieving high performance p-i-n planar heterojunction perovskite solar cells PSCs. Systematically were explored the effects of the interface modification of the Ag/ETL interface on PSCs using rhodamine 101 as a model molecule. By the insertion of rhodamine 101 as an interlayer between Ag and fullerene derivatives (PC60BM and PC70BM) ETLs improve the PCE. AFM characterization reveals that rhodamine passivates the defects at the PCBM layer and reduces the band bending at the PCBM surface. In consequence, charge transfer from the PCBM towards the Ag

electrode is enhanced leading to an increased FF resulting in a PCE up to 16.6% (The devices analyzed in this subsection were fabricated by John Ciro). Additionally, was found the work function of the metal cathode remains more stable due to the rhodamine incorporation. Consequently, a better alignment between the quasi-Fermi level of PCBM and the Ag work function is achieved minimizing the energy barrier for charge extraction.

The second case, fullerene modification of TiO_2 layers derived from nanoparticles (NPs) inks. Atomic force microscopy characterization reveals that the resulting ETL is a network of TiO_2-NPs interconnected by fullerenes. Interestingly, this surface modification enhances the bottom interface of the perovskite by improving the charge transfer as well as the top perovskite interface by reducing surface trap states enhancing the contact with the p-type buffer layer. As a result, rigid PSCs reached a 17.2% PCE (The devices analyzed in this subsection were fabricated by Jhon Ciro).

As the last case were studied the influence of MACl treatment on the film formation of $CH_3NH_3PbI_3$ by using acetonitrile (ACN) crystallization method. This method not require vacuum process neither solvent engineering, which make it one of the most promising methods to produce large scale perovskite solar cell. To understand in deeper, the properties of perovskite films grown by the ACN method and the influence of the MACl on the performance of the perovskite solar cells PSCs, were characterized in detail perovskite layers by different techniques. By AFM and SKPFM we found differences in the morphology and the work function of the perovskite with and without MACl treatment, and how the microstructure present very different behavior, moreover we found high differences in the photoluminescence emission. The perovskite with MACl treatment present a larger emission and it is in agree with their superior photovoltaic parameters. Moreover were made 10x10 cm mini modules and were compared them with ones by the solvent engineering route showing that the ACN route allow homogenous perovskite films and as a result better performance in the perovskite solar modules.

In the Appendix A is shown a description of the parameters used for the optimized films, solutions, and colloidal dispersions. Moreover, I describe shortly the methods for characterization of the layers and the PSCs and the used parameters.

Because of the importance of the AFM related techniques used in this work, is described in the Appendix B their fundamentals, and its operation. Moreover, as were used some novel techniques on perovskite is a mandatory reason to make a section with this topic.

In the Appendix C is presented a summarize of the general photovoltaics characteristics of a solar cell, and their basic working principles.

Chapter 2

Influence of Device Architecture and Different Selective Contacts in Perovskite Solar Cells

In this chapter is analyzed the influence of the buffer layers and architecture in the morphological and electronic properties of the $CH_3NH_3PbI_3$ films, and how this can influence in the performance of the devices.

2.1 Introduction

In spite of this rapid evolution, there is not a total understanding of the perovskite behavior in each configuration and its interaction with the rest of the other layers in the cell [31]. To design the cell, the choice of buffer layers, and using either planar or mesoporous structure with adequate physical properties is an important aspect in order to be able to approximate to the predicted theoretical efficiency based on detailed balance limits [32]. Perovskite solar cell optimization has overwhelmingly focused on improvements in the active layer including approaches to reach radiative efficiency limits via grain boundary studies [33, 34], understanding diffusion lengths [25, 35, 36], and crystallization engineering [37, 38]. However, as it is well known, the contacts and buffer layers have a critical role in reaching efficiency limits regardless of active layer engineering. For example, in inverted architectures p-i-n, some groups have worked with many hole transporting layer HTL showing improved performance [37, 39–42]. Particularly for a p-i-n, materials such as PEDOT:PSS, CuO, Cu_2O, CuSCN, CuI and NiO_x have been implemented. Additionally, many groups have shown how the surface modification and doping level can improve the conductivity of films and the performance

of the cells [41, 43, 44], although other papers have demonstrated that very compact and thin insulators such as $SrTiO_3$ can be used if the band alignment is good enough [45]. The inclusion of the mesoporous scaffold with Al_2O_3 and TiO_2 in n-i-p configuration has been one of the most studied, and many works have shown that these scaffolds improve crystallization and reduce shunt paths in that structure [29, 46–48].

While the TiO_2 or Al_2O_3 scaffold induces more crystalline grain formation and thereby increases the shunt resistance, Leijtens et al [25] used XPS to show a change in the Fermi level position of the perovskite active layer. In that work, they hypothesized that the scaffold fills trap states in the boundaries and thereby changes the electronic structure of the perovskite and its work function. Similarly, Ramirez et al found via Surface PhotoVoltage SPV and Transient Photoluminescence (TPL) changes in the surface charge and in the recombination lifetime due to the Al_2O_3 scaffold. In other work Sibel et al [49] showed how the surface electronic behavior is influenced drastically by the facets in the grains by locally mapping the parameters that determine PV device performance and showing the facet performance-dependence [49], Dequilletes et al showed the impact of the microstructure in the carrier generation through local PL measurements [34]. Therefore, local probes that target the interaction of the HTL and the MAPI layer are necessary to understand how to better engineer the contact in perovskite devices.

In order to understand the influence of the buffer layer and the scaffold in the cell in this work, were measured different properties of the MAPI films when it is grown on three different architectures (1) MAPI deposited directly on the glass/ITO substrate as a âhole freeâ structure (HF) (2) a p-i-n structure comprising MAPI on buffer HTL and as last was implemented a mesoporous structure with a insulator scaffold for the MAPI film.

As the buffer layers were implemented CuO_x, CuSCN and NiO_x. These HTL were chosen because in previous theoretical and experimental reports [50–52] were described as promising because their physical properties allow them to have good compatibility with the lead halide perovskite, particularly with the MAPI. The CuO_x inks and films were made by the route described elsewhere [53]. This CuO_x synthesis route was chosen because is possible have different coppers oxides, from Cu_2O to CuO (and in this way can be differentiated from the previous works [51, 52]) at different annealing temperatures, but as is difficult to be sure only one phase is present, we called it CuO_x. In spite of that, were got differentiated phases at 210°C and 270 °C. The CuSCN is a ionic material that dissolves in dipropil-sulfide solvent and beyond their physical properties, is very easy to obtain, and good quality films make it very attractive to use as a HTL. Additionally were implemented bilayers of CuO_x and CuSCN trying to combine the best properties of each layer.

The NiO_x, beyond their high band gap (3.6 eV) and transport properties, it was chosen because it is possible to make colloidal dispersions in water, which allows have films at low temperature, and is easy to get reproducible results as was reported previously by our group [54].

In this work, the performances was relatively low, PSCs with CuO_x, CuSCN and their bilayers, contrary to the results obtained by PSCs with NiO_x. To understand the different performances with the different buffer layers, morphological and surface electronic properties with the perovskite were analyzed with AFM and KPFM. Those results were correlated with the different photovoltaic parameters.

In order to analyze the influence of the structure (HF, p-i-n, mesostructured), was chosen the NiO_x as the HTL because it allows us to get an almost ideal buffer layer (and get good comparative results). In this chapter the p-i-n cells with NiO_x as HTL are called the samples (NO).

MAPI infiltrated in a Al_2O_3 scaffold structure with two thicknesses (100 and 200 nm, hereafter AO1 and AO2, respectively) deposited on NiO_x were fabricated. In that way was shown how the architecture of the cell allows different behavior in the MAPI film itself and how it affected the photovoltaic parameters and their performance. To study how the local electronic properties affect the resulting device metrics, we use SKPM techniques including surface photovoltage (SPV) and IMSKPM to explore the kinetics behavior in the scale of μs and ms that is the scale of the trapping and detrapping of charge in perovskite. Moreover were combined our AFM methods with spatially-resolved PL measurements to explore changes in the local emission in the perovskites. Additionally were used different spectroscopic and structural techniques as UV-VIS, XRD, and stationary PL measurement to correlated the local behaviors with the macro properties.

2.2 Results

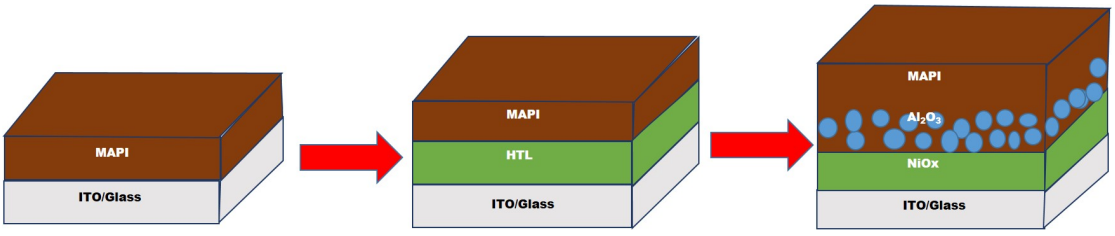

FIGURE 2.1: Schematic of the architectures from a hole free architecture to a mesoporous

In the Figure 2.1 we show an evolution scheme of the architectures discussed here. It starts with a HF structure follow with a p-i-n structure and finished with an Al_2O_3 mesoporous one. The Appendix A presents a description of the fabrication methods for the MAPI, buffer layers (NiO_x, CuO_x CuSCN), Al_2O_3, silver electrodes, and their respective thickness.

But, before getting this performances data with NiO_x as the HTLs, were fabricated devices with another HTL as CuO_x, CuSCN and their bilayers.

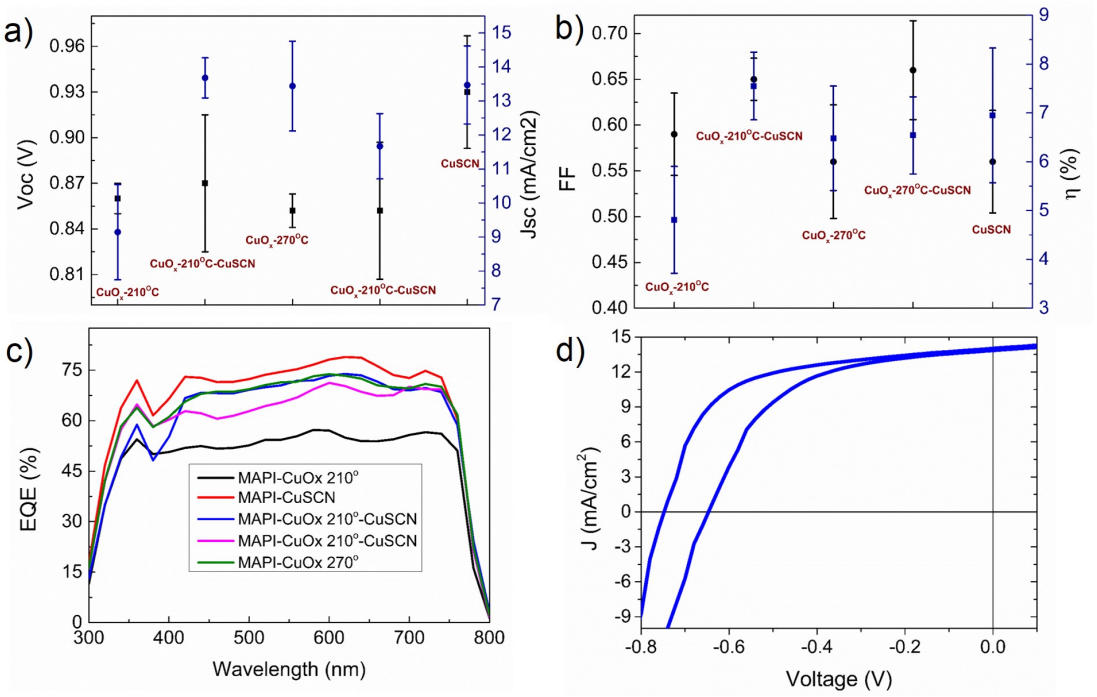

FIGURE 2.2: (a) Jsc and Voc statistics of MAPI on CuO_x at 220°C and 270°C, CuSCN, and their respective bilayers. (b) FF and η statistics. (c) EQE curves of the best devices on the different buffer layers. (d) Best photovoltaic response with CuSCN as HTL

The statistical data for those devices is shown in the Figure 2.2. All the photovoltaic parameters have poor values, the maximum PCE reached was smaller than 9% Figure 2.2b, the highest Voc was less than 1 V 9% Figure 2.2a, the FF did not reach 80% Figure 2.2b and Jsc values were smallest than 15 mA/cm^2 (see Figure 2.2a). The EQE on the different samples are shown on the Figure 2.2c, there, can be observed than any of the cells with CuO_x, CuSCN or their bilayers reach values over 75%, which make a limit for the Jsc, moreover the CuO_x is not transparent in the visible spectrum (it has a gap less than 2.23 eV, see Figure 2.6a) decreasing the photogenerated current as it can be observed in the EQE, region below 600nm. In Figure 2.2d are shown a typical I-V curve for the cells with CuSCN, is presented. The Voc is poor, and the shape does not allow good FF values which is an indication of shunt and series problems, besides its

poor photovoltaic parameters this device present a high hysteresis which is a not desired feature in PSCs. To get more insights of the bad photovoltaic performance when this buffer layers are implemented, were studied the CuO_x and CuSCN films by AFM and KPFM.

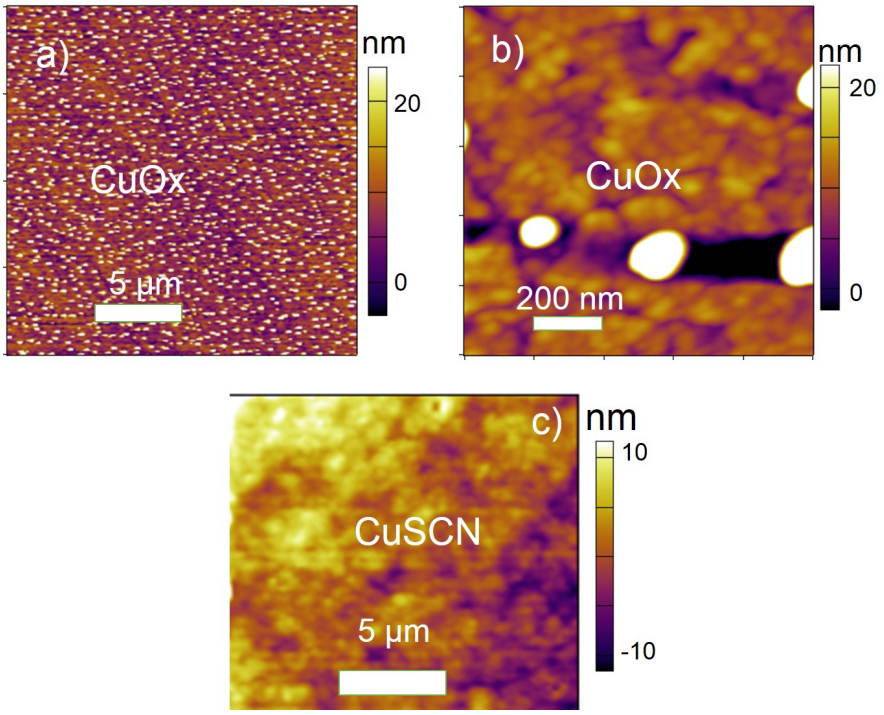

FIGURE 2.3: (a) AFM 20X20 μm topographic image of CuO_x thin films, (b) AFM topographic image of CuO_x 1x1 μm, and (c) CuSCN 1.5x1.5 μm topographic image

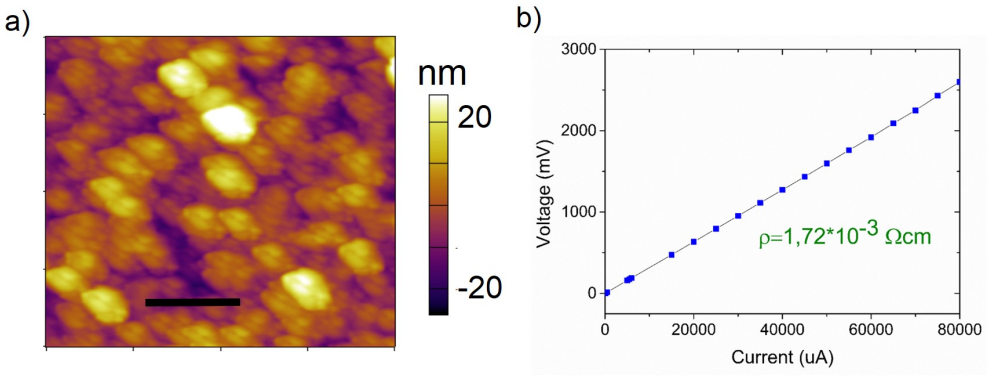

FIGURE 2.4: (a) Topographic AFM image of the NiO_x film, scale bar 500 nm. (b) IvsV curve for the NiO_x film on ITO/glass substrate.

In the AFM images Figure 2.3 a, b some defects are found for the CuO_x films (See appendix B for details of the technique, and appendix A for the used parameters). Some white points are visualized between a homogeneous matrix, it is hypothesized that this points are particle formations from the precursor solution. This particles were possible

CuO precipitations between a CuO_x matrix, which evidently affected the morphology, but also can affect the electronic properties of the film because its different surface potential (different work function). These particles, are points of bad contact for the MAPI films, around them the effect of electron blocking is affected. These defects affect all the photovoltaic parameters as shown in Figure 2.2, including the Jsc, that in the first instance must depend on the properties of the perovskite. The CuO_x films do not only decrease the performance of the cells but also affected the perovskite itself. As a strong prove of this, previous to the growing of the MAPI on the CuO_x was necessary an UV ozone treatment on the CuO_x to improve the wettability and can get films of MAPI on CuO_x, this is an indication of non coordinate species in the CuO_x (In many reports have been studied the surface oxygenation in polymers and oxides [55–57]), which which besides of do not allow the film formation of the MAPI without UV-ozone treatment, give insights of some chemical reaction of CuO_x with the MAPI, this interaction can produce decrease in the the Voc and the FF (additional work with another techniques is necessary to prove these hypothesis).

As a contrast, in Figure 2.4a the morphology of NiO_x film is shown, grains are composed by particles, as expected due to the precursor solution composition as a dispersion of Nanoparticles (NPs) (See Appendix A for precursor preparation details). The agglomeration of the particles after drying, and their good coalescence, allow high quality films with very few pinholes.

In the Figure 2.4b is presented the I-V curve to the ITO/NiO_x. From this curve is calculated the resistivity of the NiO_x on ITO. As is expected in a good buffer layer, the NiO_x film have a value of the resistivity that is very close to that one of ITO itself, which is an indication that the NiO_x film does not get an additional series resistance to the device (see Appendix C for details of the meaning of all photovoltaic parameters, including series resistance). On the other side in the 4 point resistivity measurements on CuO_x and CuSCN, the compliance of the equipment did not allow take the data, but let us conclude that the resistivity of those films is higher than 10^9 , giving an additional serie resistance to the cell and affecting the FF.

In the Figure 2.5 were observed the difference in the Vcpd between the buffer layers and the ITO (See appendix B for details of the KPFM technique, and appendix A for the used parameters). This value is the differences in their work functions (Energetic difference between the vacuum and Fermi levels). In the Figure 2.5a a difference of 50 meV is found for the CuO_x with 210°C of annealing, in the Figure 2.5b a similar result of 60 meV was obteined for 270°C sample, and a difference of 500 meV for CuSCN. With this relations can be estimated the difference between the the Fermi levels of this HTLs and the perovskite. There is some position in the Fermi level than allows a perfect

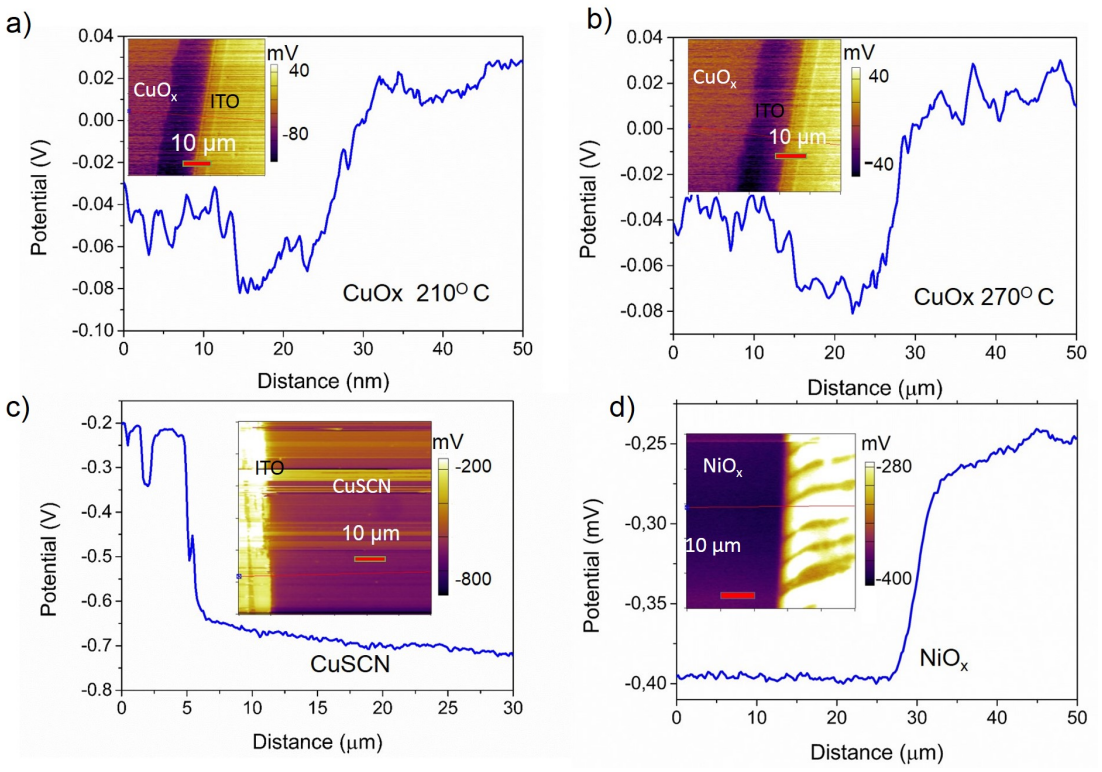

FIGURE 2.5: (a) Profile of Vcpd between CuO_x with annealing proces at (a) 210 °C (b) 270 °C and ITO, and (c) CuSCN and ITO, (d) NiO_x and ITO

band alignment with the MAPI, some deviations gives some energetic losses if after the equilibrium (alignment of the Fermi levels) the valance band of the buffer layer is higher than the perovskite, or not blocking electrons if the buffer band is under the perovskite band. This two possible results will be reflected in the photovoltaics parameters. In the first case a loss in the Voc is presented, and in the second case, the FF and Jsc will be affected. In the case of CuO_x both at annealing of 220°C and 270°C, big losses in the Voc should be present as is proved in the device statistics, but in the case of CuSCN there is not a efficient blocking of electrons, which do not allow better performance.

Sample	SPV (respect-ITO) meV	Eg (eV)
NiO_x	150	3.64 [58]
CuO_x 210 °	60	2.23
CuO_x 270 °	150	1.76
CuSCN	500	3.6

TABLE 2.1: Surface potential respect ITO and gap of energy of the HTL

In contrast a difference of 150 meV in the work function when the measurement is taken from the NiO_x film to the scratched ITO part was observed Figure 2.5d. This difference produces a minimum loss of energy which results in a small decrease of the Voc as is shown in the Figure 2.6b.

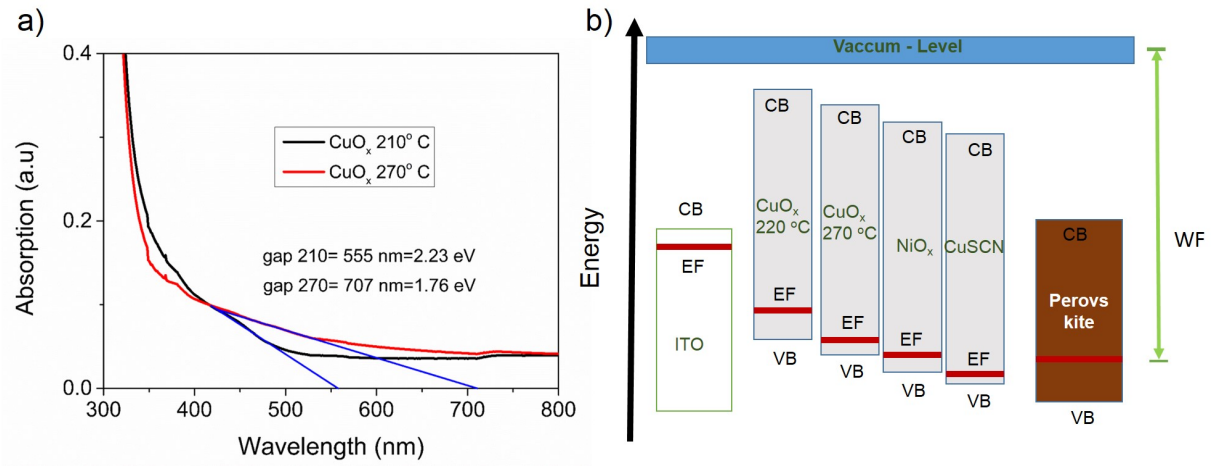

FIGURE 2.6: (a) Absorption of CuO_x with annealing at different temperatures. (b) Comparisson of bands and fermi level of the different buffer layers with the fermi level of the perovskite

As a conclusion the fabricated CuO_x and CuSCN did not work as well as was expected by previous reports. I found several morphological and electronic features that make them not optimal HTL for the p-i-n configuration. On the other hand was found thar NiO_x has almost the ideal morphological and electronic characteristics as a HTL in a p-i-n structure.

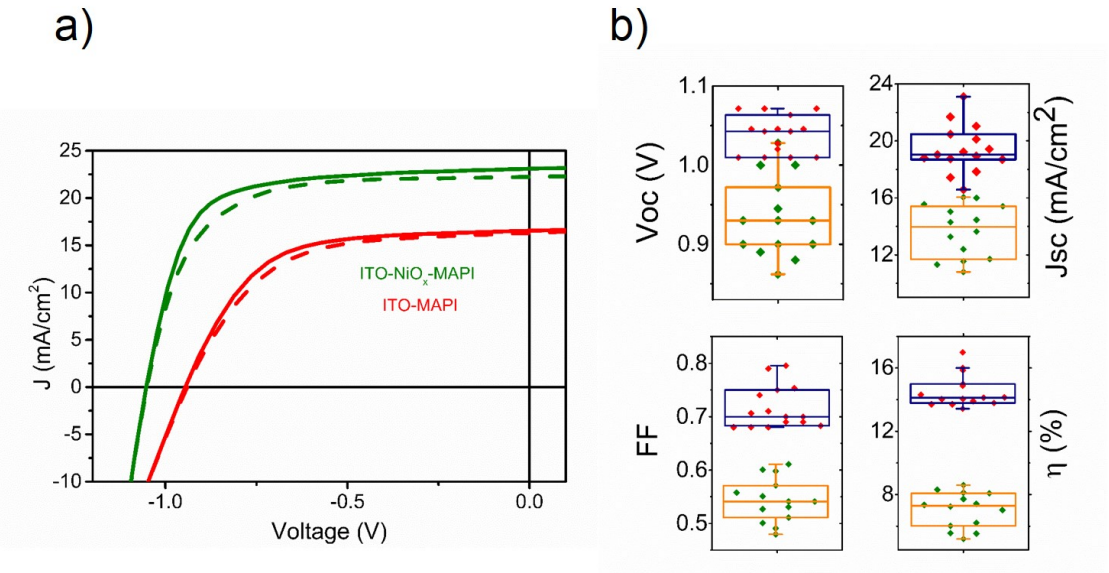

FIGURE 2.7: (a) JV curves of the best devices for the samples HF and NO, the continuous lines are the measurements in forward and the dashed lines in reverse. (b) Statistics for the photovoltaic parameters of the planar structures, green points samples HF and red points samples NO with the mean value s in the center of the box

Now that were analyzed the possible causes of the better performances of the cells with

NiO_x with respect to the other buffer layers, it is possible to discuss the influence of the structure (with a good HTL as NiO_x) in the PSCs.

The performance of the best HF and NO based devices is presented in the Figure 2.2a, statistical data for those samples is shown in Figure 2.2b. The results 8% for HF and 17% for NO, are comparable with the best results obtained by other groups [54, 59]. The photovoltaic parameters of the mesoporous structures were taken from a work made by (Ramirez et al). In the structures were observed differences in the performance due to changes in the photovoltaic parameters Voc, Jsc and FF when was included a high quality film of NiO_x.

The increase in the Voc when NiO_x is include (evolution from a HF structure to a NO) can be attributed to a misalignment in the bands of the perovskite and the ITO in the HF configuration as was shown in Figure 2.6, which was confirmed through Kelvin probe microscopy measurement KPFM (see Figure 2.6d). Moreover the ITO can receive both electrons and holes from the perovskite and the diode behavior is decreased as is proved in the FF and Jsc values.

In order to explore morphological changes in MAPI films in different architectures, topographic images are presented in in Figure 2.8 a-d for the samples HF and AO2, AO1, NO respectively and the changes in the local work function through KPFM are presented in the Figure 2.8 e-h for the same samples respectively. A grain structure is observed both for the planar on NiO_x and for the mesostructured film, but a small increase in the grains for the MAPI film in the mesostructured device is observed, it has little grains (200nm) than the film on Al_2O_3 (220 nm) (the diffractograms are shown in the Figure 2.10 and not significant changes in the Full Width at Half Maximum (FWHM) or preference growing in some direction are visualized).

To confirm that the KPFM image is not a topographic cross talk, it can be observed how the potential in different grains (with numbers) does not follow the topography (some grains with major height present a small potential), this is totally related with different facets present in the surface, as early analyzed by Sybel et al [49], and discussed by Eperon and Ginger [60]. As a hypothesis though the diffraction images looks similar and the morphology only shows a slightly change in the grain size in the different architectures, these little changes makes a difference in the recombination processes in the MAPI as is discussed below.

The SPV mean value at different illumination intensities for the perovskite grown on top of NiO_x, and ITO is observed in Figure 2.11a, and KPFM images at all illumination intensities are presented in Figure 2.9. As was described by Zhang et al [61] the sign is related with the predominant surface states, and its magnitude is related to its density.

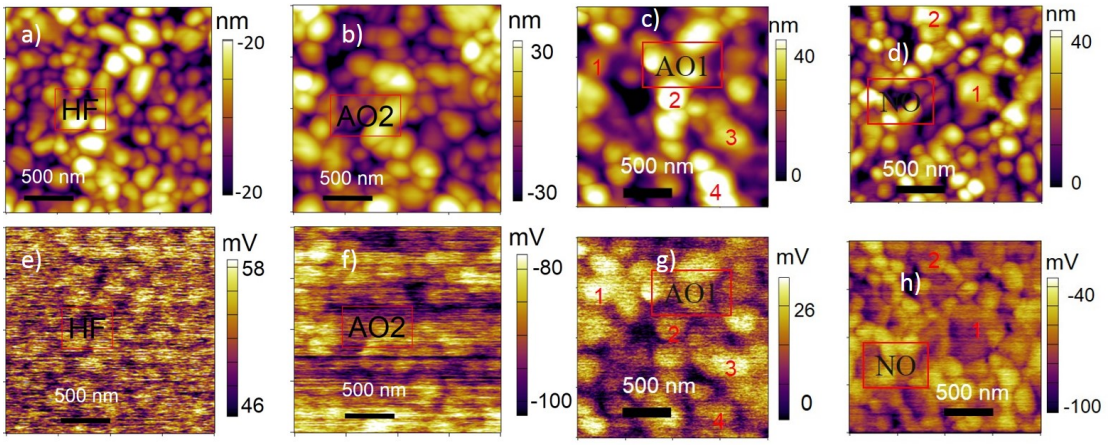

FIGURE 2.8: (a-d) Topographic images of MAPI for the samples HF, AO2, AO1, NO respectively and (e-h) KPFM images for samples HF, AO2, AO1, NO respectively

A negative SPV is an indication of donor states ionization and the band bending should looks as depicted schematically in Figure 2.11b. MAPI grown on NiO_x showed an increase of the bending as light intensity increased, similar to that reported by Ramirez et al for mesostructured cells. However, the HF structure has another behavior. The SPV decreased until the light intensity is 25% before reaching a plateau. The different surface voltage of both can be related to the lack of HTL in the HF sample, which produce a faster saturation of charge in the surface, so this screening do not allow more accumulation of electron in the interface perovskite-tip, so there is saturation of holes near to the bottom of the device, near to the MAPI-ITO interface. This screening at low intensities in the HF architecture means that could be an Schottky potential barrier in the interface MAPI-ITO, it has implications in the low FF reached. Moreover when the NiO_x is include this effect is reduced and the photovoltaic yield is increased.

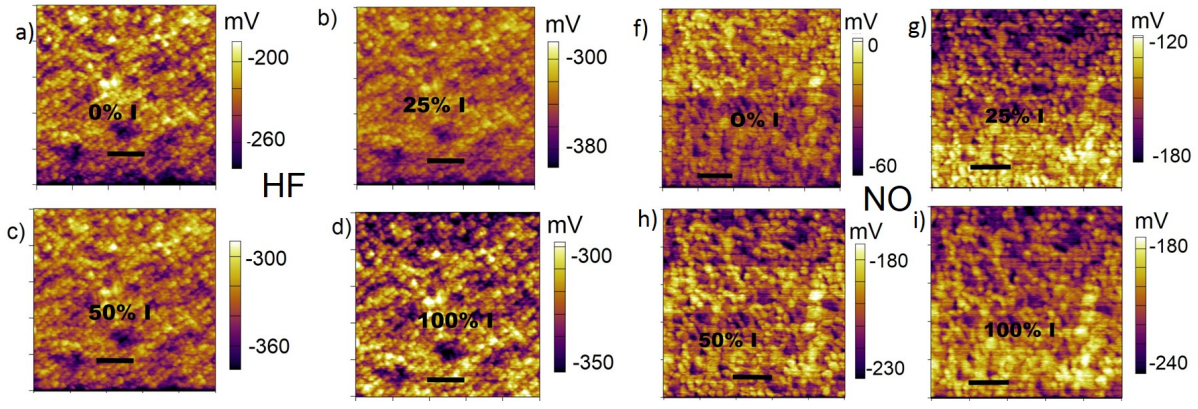

FIGURE 2.9: SPV images for the MAPI on ITO at different intensities (a) dark, (b) 25%, (c)50%, (d) 100%, and MAPI on NiO_x (e) dark (f) 25%, (g)50%, (h) 100%, scale bar 1 μm

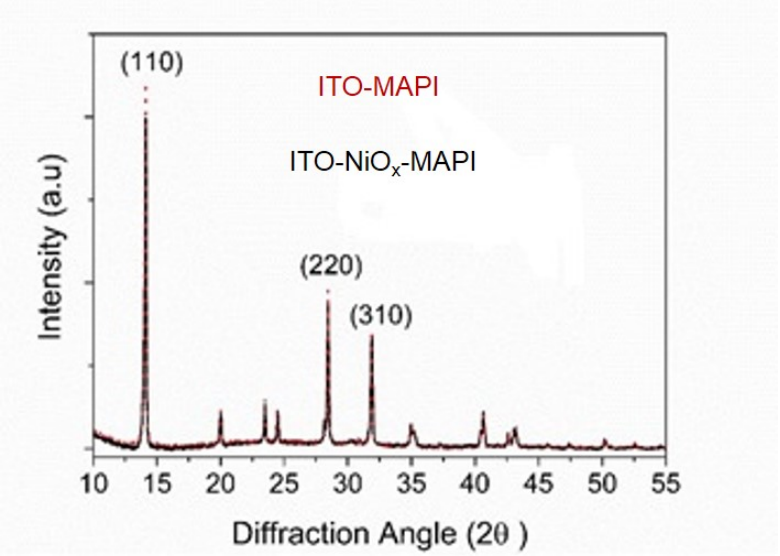

FIGURE 2.10: X-Ray diifraction patterns of the perovskite in hole free and p-i-n structure

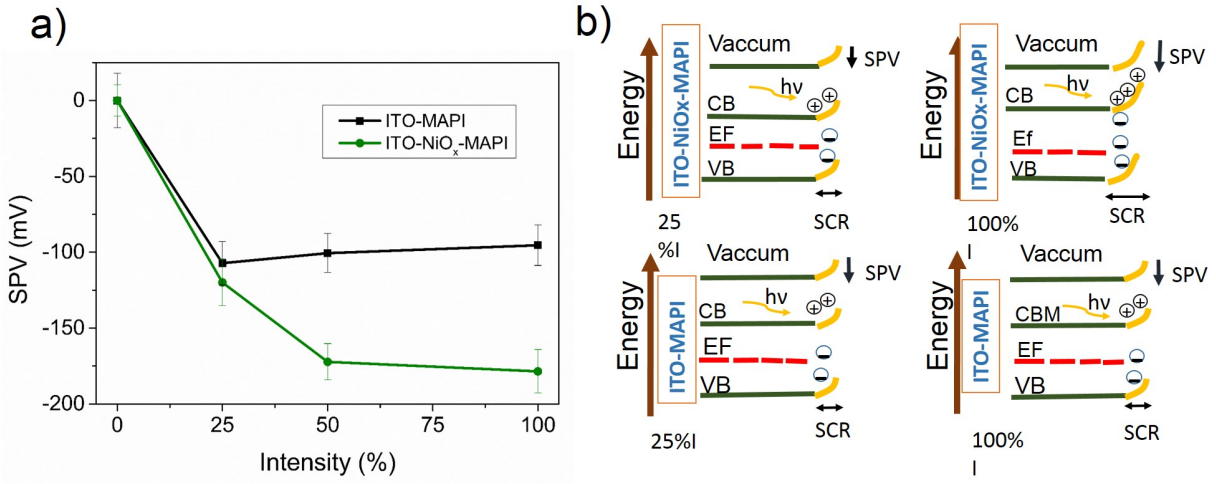

FIGURE 2.11: (a) SPV at different light intensities for the sample HF black, and green, sample NO. (b) Schematic for the band bending in the surface for the samples NO in the top and HF in the bottom, at 25% of the light intensity in the left and 100% in the right

In order to better understand the influence of the architecture in the MAPI non-radiative recombination process, were used IM-SKPFM measurements (See appendix B for details of the technique, and appendix A for the used parameters) to explore the recombination mechanisms present in the order of μs and ms [62–64]. With this technique can be observed the relaxation time τ of the SPV as a laser is pumping from 1 Hz until 7 MHz. Because the dynamic of the recombination systems is influenced by initial free charges, both electrons and holes, we want the device at some particular open voltage circuit

value. In order to do that, recombination measurements with background illumination was taken. To fit the curves we use the relationship of the SPV in the frequency domain [64] (equation 2.1)

$$SPV(f) = \frac{SPV_0}{2} + SPV_0 f(1-\beta)(1-e^{(\frac{1}{2f\tau})}) \tag{2.1}$$

Where SPV_0 is the surface potential under continuous light illumination, f is the frequency and β is the stretching factor. Times observed in Figure 2.12 are in the order of μs. This timescale corresponds more probably to carriers entering trap states because the ion movement is in the order of seconds so it is difficult to see by this technique [35]. The differences in time between the planar and the mesoporous structure is a confirmation that the alumina is not only an insulator scaffold for crystal growth of the perovskite but also changes the electronic structure of the perovskite through gap states.

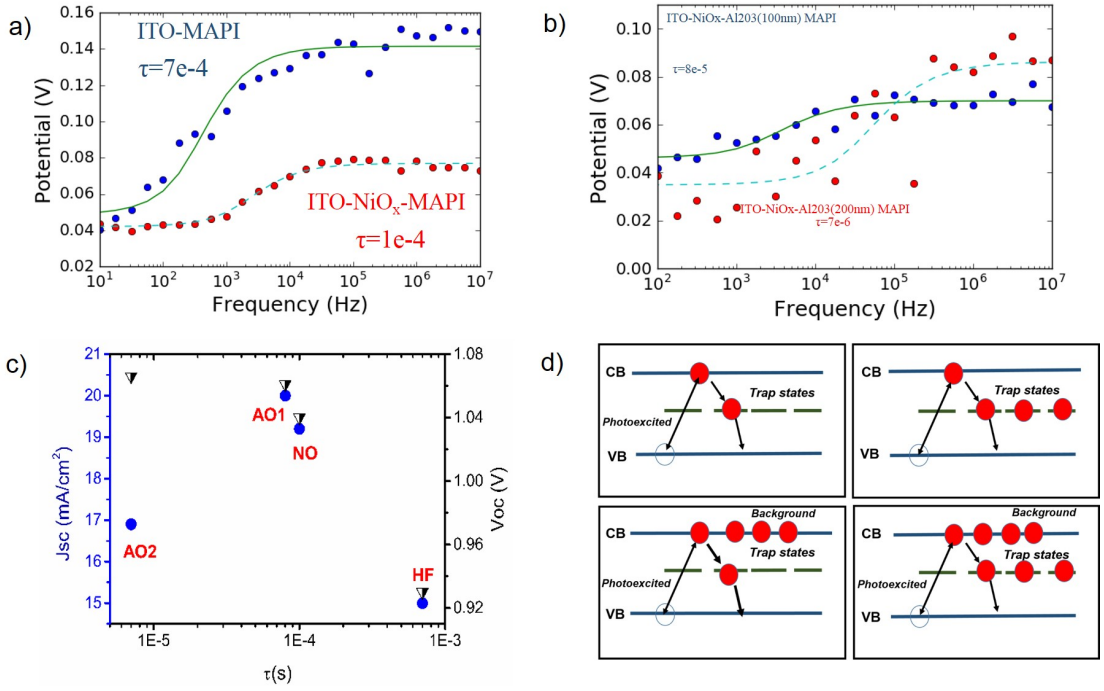

FIGURE 2.12: Average photovoltage at different modulation frequencies under dark (a) planar samples and (b) mesoporous structures, circular points are the experimental values and lines are the fits at the equation 1. (c) Comparison of the pseudo carrier life time of all the samples with the Jsc and the Voc. (d) Left, electronic structure for the planar and in the right for the mesoporous structure

In Figure 2.12c can be observed the relationship between the Voc and the characteristic time τ and how the Voc decreases when the relaxation time increases. This kind of behavior is present in systems with high recombination orders (non-monomolecular) and is related to high carrier dependent mobility previously found in organic semiconductors

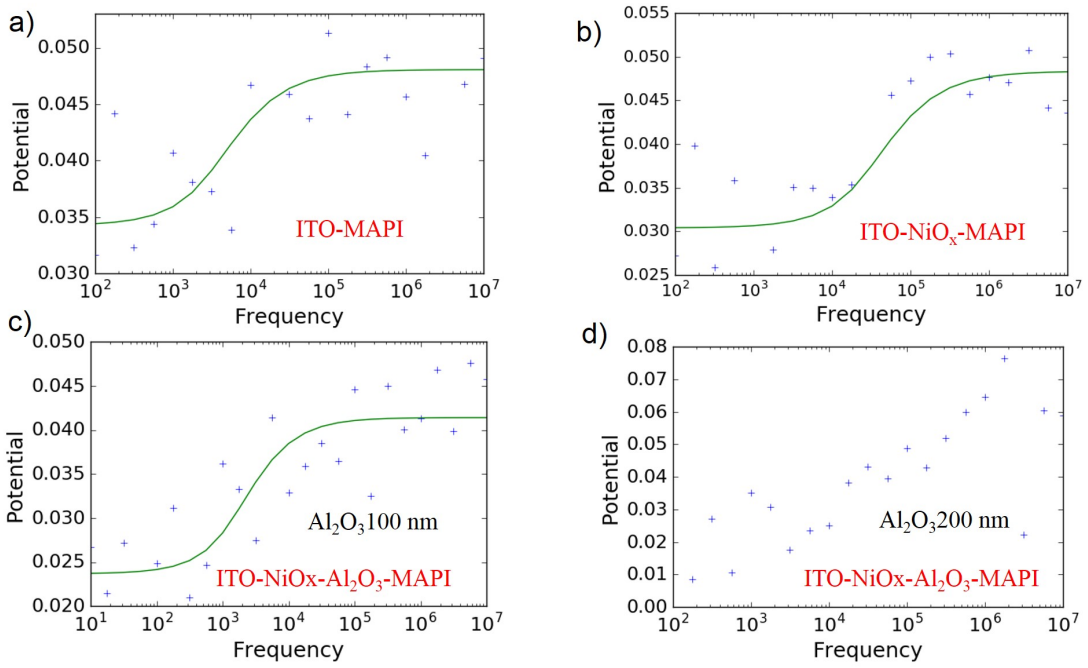

FIGURE 2.13: SPV change in the frequency domain with white light as a background. (a) HF, (b) NO, (c) Al 100, (d) Al 200

[63, 65–67]. In hybrid perovskite this dependence is directly related to trap structure in the sub band gap region [36]. To understand the trap mechanism in the cells is used the sketch in Figure 2.12d. In that diagram is observed in the left the structure for the planar cells and in the right for the mesoporous structures. The top schematics in Figure 2.12d are for the case under dark. In this condition, some traps states in the mesoporous structure are already filled as was hypothesized by Leijtens et al [25], so the recombination process is significantly faster with a rapid band-to-band process involved [35]. In the planar architecture charges first fill the traps and subsequently decay to the valence band, this process is slower by comparison and also produces more charges trapped in mid-gap states as reflected in the Voc discussed previously. With background illumination, the background population of carriers shortens the subsequent recombination lifetime and exceeds the instrumentation response (see Figure 2.13).

In order to explore the local spatial and temporally changes in the MAPI in the different structures located PL was used.

In Figure 2.14 is presented the images of the located photoluminescence PL with the ITO grounded. At the grain structure of the MAPI there is an heterogeneity in the PL spectrum with grain boundary zones without light emission and grains with more PL than others as was reported by Eperon et al [68], they found an anticorrelation between the PL and the conductivity in some grains due to changes in the quenching of the grains [68] . For the Figure 2.14a, corresponding to planar HF, the image turns

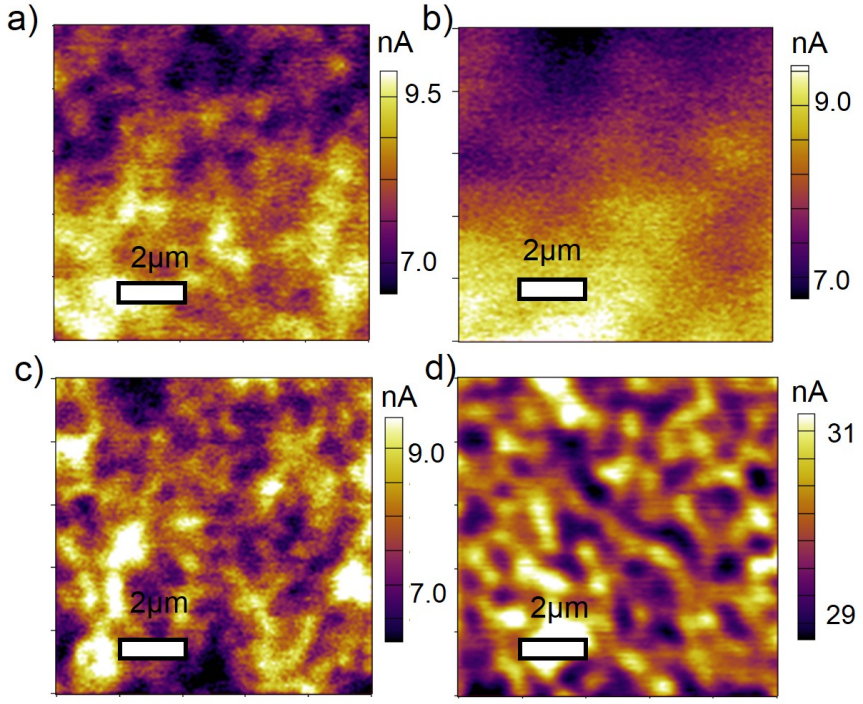

FIGURE 2.14: Local PL (a) sample HF, (b) sample NO, (c) sample AO1, (d) sample AO2, scale bar 2 μm

darkest (lowest PL) with the time under continuous illumination; the PL decreases over time. This behavior is proved further by measuring the time-dependence of the PL in the Figure 2.15c and observed a decrease in PL intensity over time. On the other hand, he PL for the MAPI film on the Al_2O_3 scaffold does not change with the time as it is observed in the Figure 2.14 c for the sample AO2, is hypothesized that the change in time of the PL in the perovskite is due to ion movement because of the seconds-long timescales observed [35, 69]. Ion movement can explain the improvement of the stability by the inclusion of the Al_2O_3 scaffold showed in the work by Ramirez et al, but in order to a better understanding, is required more experiments on that time scale.

Another characteristic observed in the PL images is that the MAPI on AO2 have a clearly stronger intensity (average 30 nA, lock in intensity) compared to the rest of the samples (average 9nA). This highest PL intensity is a product of poor quenching because of the thickness of the entire sample does not allow a good collection of the charges by the HTL (NiO_x in this case). This result is self-consistent with the low Jsc and EQE measurements for scaffolds thicker than 200 nm. E. Figure 2.15 a, b shows EQE, Jsc integrated and the absorption measurements for the planar structures, in the HF structure a decrease of the EQE in the blue region is observed which is an indication of worst minority charge collection to the ITO. This is agree with the fact that the NiO_x improve the alignment and charge collection of the cell. Moreover the absorption measurements shows small difference in the spectrum, probably due to difference in the

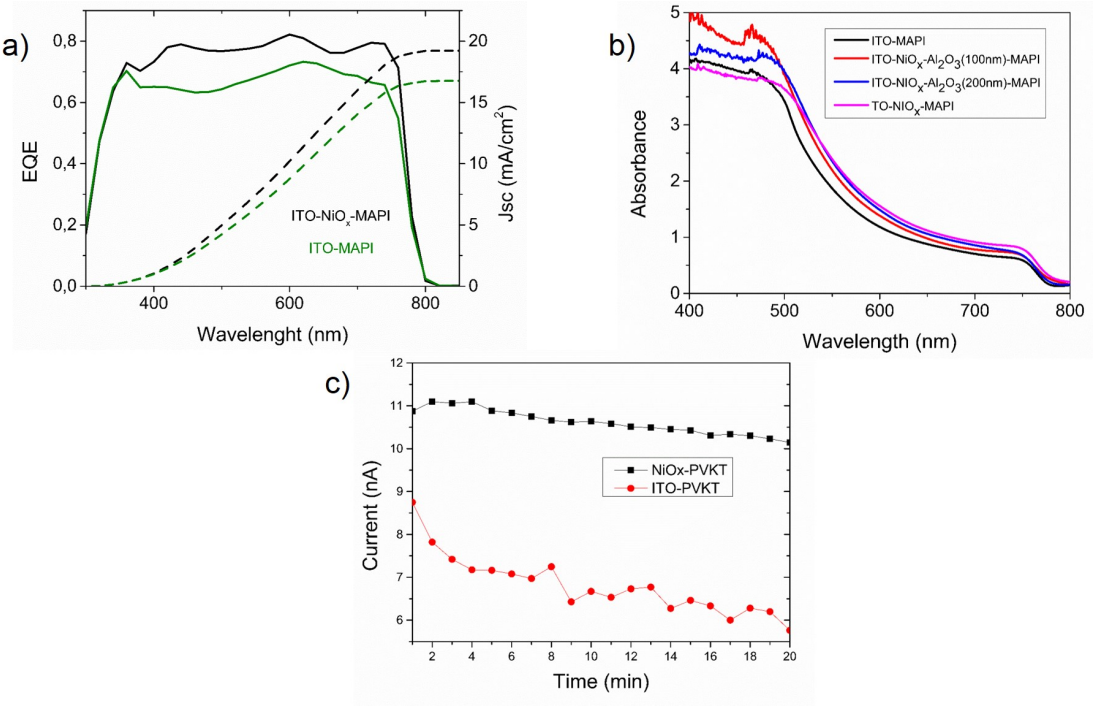

FIGURE 2.15: (a) EQE for the MAPI grown on ITO and ITO-NiO_x. (b) Absorbance curves for the perovskite grown on the different structures, (c) PL on time for the MAPI on ITO, and MAPI on ITO-NiO_x

scattering for all the samples which is evident in the apparently offset. These data show that the change in the photovoltaic parameters is mainly due to recombination process and charge collection affected by different sub gap states as a result of different grain surface formation as was proved.

2.3 Conclusions

Was found through AFM and KPFM how the morphological and electronic (Work function) properties of the HTLs affect drastically the performances of the solar cell. We show how a very compact NiO_x layer allows high performances perovskite solar cells because its morphology avoids shunt paths and its Fermi level position allow a nice band alignment with the MAPI, minimizing loses in the Voc. In contrast poor results were obtained with the HTLs CuO_x and CuSCN, due to problems in morphology, possible chemical reaction with the MAPI and bad band alignment.

Was shown via IM-KPFM, photoluminescence maps and KPFM how the addition of NiO_x as a HTL and Al_2O_3 scaffold insulator change the surface band bending and the recombination properties of the MAPI. We interpret this relationship in terms of the surface structure and conclude by IM-SKPM that in mesoporous architecture the devices

have different electronic dynamics than in the planar and hole free. These films have more stable light emission as was proved by PL over time and exhibiting higher PL intensity.

Future work will focus on particular grains facets to better understand the electronic mechanism in each particular case, and also look the evolution in time of the performance to establish if some facets in the surface are likely to changes in recombination process, degradation and decrease of the performance.

Chapter 3

Influence of Surface Modifications in Selective Layers in Perovskite Solar Cells

Three different types of studies are analyzed. In first section, is studied in a the p-i-n structure, through AFM methods how the a small quantity of Rhodamine modifies the interface between the ETL PCBM and the electrode Ag, and how this can improve the transport properties and the solar cells performances. In the second case, in a n-i-p structure, through photoluminiscence, AFM and KPFM is analized how a TiO_2 layer grown from a nano particle dispersion can be modified by a small quantity of PCBM, and how this affect amazingly the electronic properties and performances of the PSCs. In the third work is analyzed through SPV the influence of MACL in the promessing $CH_3NH_3PbI_3$ acetonitrile crystallization route. Moreover is proved the superior surface properties of this perovskite layer for scaling up process in perovskite solar cells.

3.1 Analysis of modification Ag/PCBM interface by Rhodamine to enhance efficiency of perovskite solar cells

3.1.1 Introduction

Interface engineering in perovskite technology has the potential to lead simultaneously to highly efficient and long-lasting devices [70–72]. In fact, [73, 74] demonstrated that controlling the surface recombination at the top and bottom interfaces of the perovskite

results more relevant than controlling the corresponding recombination in bulk and grain boundaries for reaching high performance devices.

One of the most studied ETLs in p-i-n planar perovskite solar cell (PSC) is PCBM [75–80] this molecule has suitable properties as ETL such as good electron mobility, proper energy alignment with the conduction band level of the perovskite and orthogonal-solvent processability enabling the PCBM film formation on top of the perovskite layer [78, 81–83]. However, several reports show that p-i-n PSCs with a single PCBM layer as ETL have poor PCE being necessary additional ETLs [37, 77, 81]. The poor performance of single layer PCBM has been attributed to the ineffective control of the properties at the metal-cathode/organic-semiconductor interface [84]. For instance, metals of high work function, such as aluminum or silver, present high energy mismatch with the quasi-Fermi level of PCBM resulting in poor device performance [84]. Although low WF metals such as Calcium (Ca) form good contact with organic semiconductors, its instability under environmental conditions hampers its practical application. In general, the optimized electron transporting layer (ETL) is composed by a multilayer stack where each material has a specific function [83, 85–88]. These interlayers must adjust the WF of the cathode to improve the contact with PCBM and must possess solvent orthogonality to allow film formation atop the PCBM layer. With this objective, several authors have explored different molecules such as Rhodamine [89, 90], C60 [72, 86], lithium fluoride [72, 83], bathocuproine[91], alcohol soluble titanium chelate TIPD (titanium (diisopropoxide) bis(2,4-pentanedionate) [92] and fullerenes derivatives [54, 72, 93]. Moreover, even polymer isolators have been incorporated as part of the device structure intended for creating physical barriers against ambient degradation[94, 95]. In particular, Rhodamine 101 possesses an intrinsic dipole moment and does not diffuse under electric field enabling a broad tuning of the work function in metals and also in transparent conductive oxides [85, 90]. In addition, its processability in anhydrous alcohols makes it compatible with PCBM. As a result, [80] 25 % efficiency in p-i-n PSCs has been demonstrated. However, the physical mechanism behind the improvement associated to the Rhodamine incorporation has not been yet fully proved.

In this section, is demonstrated the role of Rhodamine in enhancing the PCE in p-i-n planar PSCs. As demonstrated by a surface photovoltage analysis, Rhodamine modified the band bending at the PCBM surface and homogenization of of the surface potential of PCBM leading to a small improvement of Voc. Moreover is shown a change of the work function of silver electrode as a consequence of its interaction with Rhodamine, improving the band alignment and the conduction path of electrons, producing a clear improvement of the FF.

3.1.2 Results

The ETL/metal interface of a p-i-n planar PSCs was effectively improved by incorporating Rhodamine 101 in the basic device structure. Were analyzed cells p-i-n planar PSCs fabricated in the group using NiO_x as hole-transporting layer, PC60BM or PC70BM as electron-transporting layer and Rhodamine as interlayer between the Ag and the PCBM as shown in Figure 3.1a. In the Appendix A there are the description of fabrication methods for the MAPI, NiO_x-PCBM and Ag electrodes and their respective thickness. The HOMO and LUMO levels of the Rhodamine are depicted in Figure 3.1b . Moreover the modification of the WF of the metal electrode produced by the Rhodamine layer was measured by KPFM. It was found that Rhodamine decreases the WF of silver around 0.18 eV as shown in Table 3.1. Accordingly, Rhodamine is expected to reduce the 0.6 eV energy mismatch between PCBM and the silver cathode Figure 3.1b consequently enhancing the quality of the interfacial contact and the electron collection. Solar cells with the Rhodamine interlayer showed a remarkable improvement of all photovoltaic parameters, in special the FF from 73.03% to 76.16% for PC70BM and from 65.73% to 73.18% for PC60BM, with respect to the devices without it as presented in Figure 3.1c.

Sample	ΔV	ΔWf
Glass/Ag (Reference)	0C	0
Glass/Ag/Rhodamine	413	-0.43
Glass/Rhodamine/Ag	307	-0.30
Glass/ITO/NiOx/Perovskite/PC70BM/Ag	26	-0.04
Glass/ITO/NiOx/Perovskite/PC70BM/Rhodamine/Ag	152	-0.18

TABLE 3.1: Changes in the work function of the Ag

A careful analysis of the topography and surface potential allowed determining the central role of the Rhodamine in the the PCBM-silver interface. Topography analysis (Figure 3.2, Figure 3.3) show that the perovskite film is composed by large grains of about 270 nm with clearly delimited boundaries and large height fluctuations (roughness = 9.1 nm). Similarly, PC70BM layers are formed by well-connected grains of about 220 nm with low height fluctuations (roughness = 2.4 nm). PC70BM layers exhibit densely packed grains with less differentiated grains and a low roughness remaining almost unmodified upon the addition of Rhodamine. On the other hand, the surface potential at the grain boundaries of the perovskite layer shows high fluctuations as shown in Figure 3.2d. These fluctuations are related to under-coordinate chemical bonds at the semiconductor surface that in some cases can act as charge trapping states. Therefore, the perovskite layer can exhibits a high density of surface trap states potentially leading to non-radiative recombination centers.

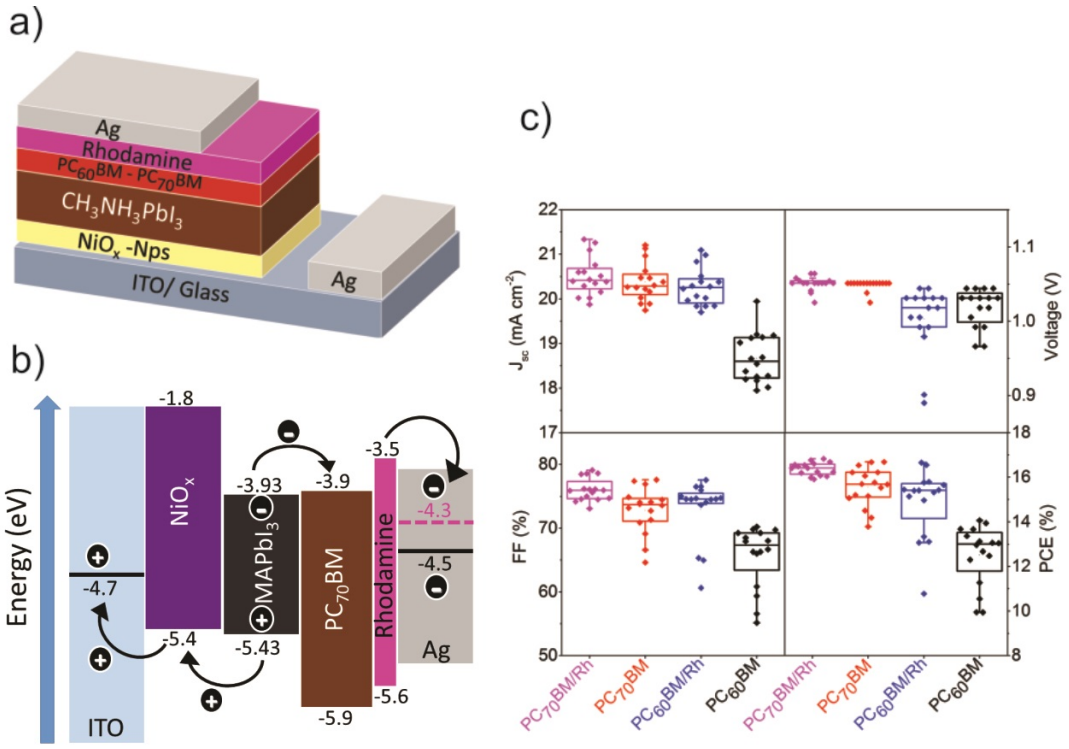

FIGURE 3.1: Interface engineering of the ETL-cathode interface by employing Rhodamine 101. (a) Studied device configuration. (b) Energy diagram for the constituent layers, along with electron and hole transfer pathways. The WF of silver in the device with Rhodamine changed by -0.18 eV (pink dashed line). (c) Box charts associated to the photovoltaic parameters of the fabricated solar cells, the statistical analysis was performed including both forward and reverse scans (This image was taken work made by the authors of [96])

Similarly, the PC70BM films (Figure 3.2e) present important variations in the surface potential along the entire layer. Interestingly, the Rhodamine inclusion represented a strong reduction in the variation of the surface potential as evidenced in Figure 3.2f. Since the spatial uniformity of the surface potential can be associated to the passivation of defects in organic semiconductors [97, 98], the Rhodamine interlayer induces a lower accumulation of defects right before the metal cathode enhancing the charge transfer. Moreover the surface potential uniformity allows uniformity in in the Fermi Level and as a result an uniform band alignment, this is particularly evident in the improvement of the statistics of all photovoltaic parameters.

PL measurements Figure 3.4 show that Rhodamine does not affect the PL emission intensity of perovskite/PCBM layers. Therefore, Rhodamine has no effect on the radiative recombination of the perovskite. Thus, the improve charge transfer should be attributed to lower accumulation of defects as discussed before.

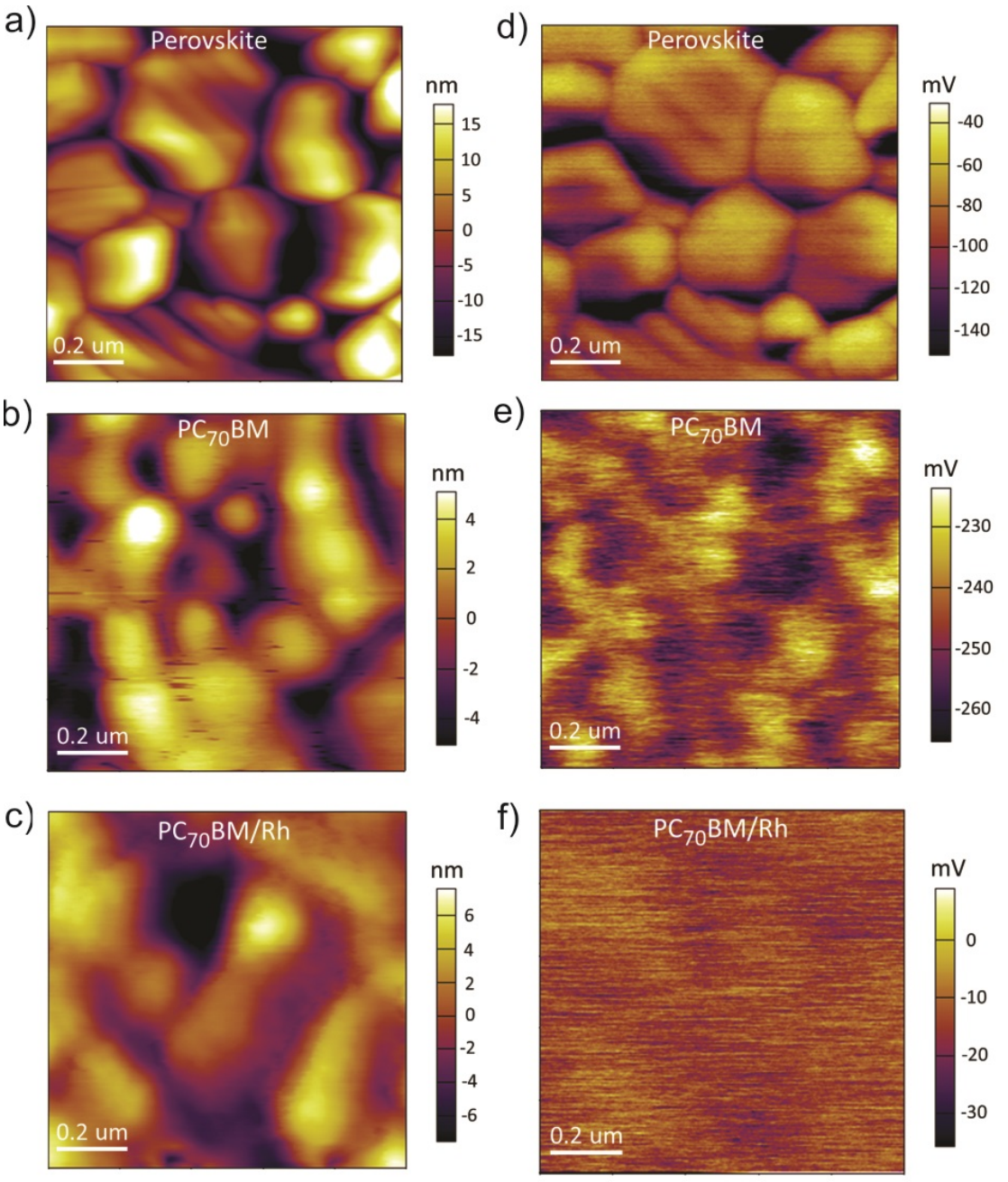

FIGURE 3.2: (a-c) Topography and (d-f) surface potential maps of the (a, d) perovskite layer on NiO_x (b, e) PC70BM layer on perovskite and (c, f) PC70BM / Rhodamine layer on perovskite. The electronic effect of the Rhodamine in stabilizing the surface potential is apparent

3.1.3 Conclusions

Has been analyzed the role of the Rhodamine interfacial layer on the enhancement of PCE of p-i-n planar PSCs. On the other hand, AFM characterization allowed us to explain the effect of Rhodamine on the improvement of the photovoltaic parameters of PSCs. Despite that Rhodamine has little impact on the topography of the PCBM

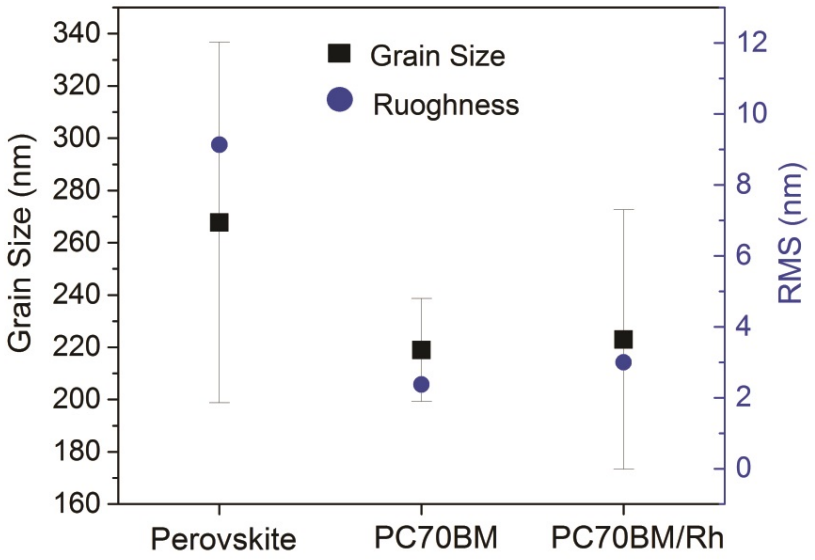

FIGURE 3.3: Grain size (black squares) and roughness (blue circles) of perovskite (PVKT), PC70BM and PC70BM/Rhodamine (Rh) surfaces

layers, it induces an important change on its surface electronic properties. Surface potential measurements demonstrate that Rhodamine passivates surface trap states leading to reduced non-radiative recombination. Moreover the Rhodamine layer changes the electrode work function allowing a better mismatch with the ETL. Accordingly, p-i-n planar PSCs including Rhodamine achieved the highest reported PCE up to 16.8%, for this type of architecture. This section contributes to a better understanding of the operational mechanisms of PSCs, specifically about the role of silver-electrode/organic-semiconductor interface

3.2 Analysis of fullerene surface modification of the titanium dioxide as electron transport layer in a n-i-p perovskite solar cell

3.2.1 Introduction

Most efficiency perovskite solar cells PSCs have been reached implementing the regular n-i-p device structure [99] with TiO_2 representing the typical ETL due to its low cost, phase stability and effective carrier dynamics control when employed as scaffold [100–104]. However, the advancement towards planar n-i-p devices has not been easy making

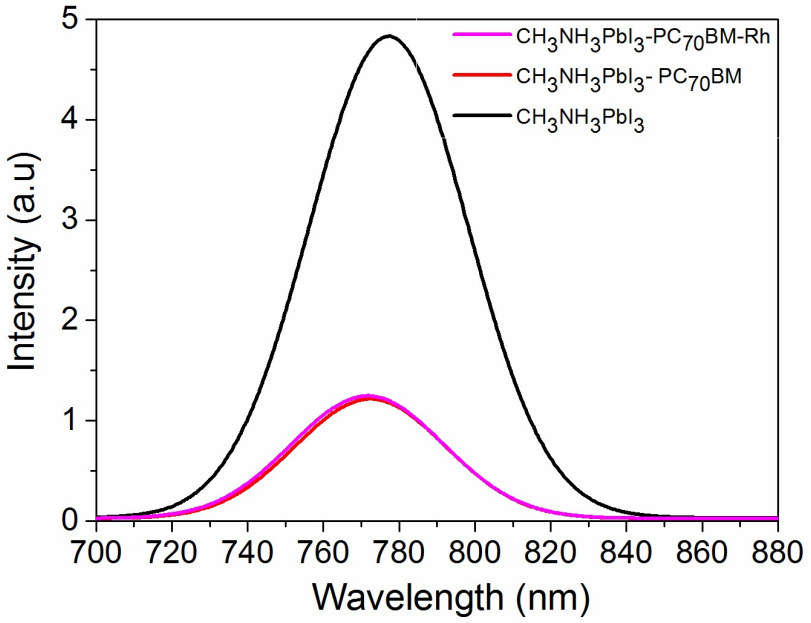

FIGURE 3.4: Photoluminescence spectra of Perovskite samples on glass with or without ETL layers

apparently due to the need to accomplish a precise control of the TiO_2/perovskite interface. This objective is transversal to all the perovskite photovoltaic research since Yang et al [73] recently demonstrated that recombination in the top and bottom surfaces of the perovskite is more important than even the recombination intra- and inter-perovskite grains. Two main strategies have been explored for effectively controlling the TiO_2/perovskite interfaces: growing the TiO_2 using a more controlled deposition method or incorporating specific interlayers. In the first approach, TiO_2 growing methods such as sputtering, [103] e-beam [100] or atomic layer deposition [105] led to a good device performance. Actually PCE ranged from 12.2% to 17.6% but were essentially limited by the relatively complex deposition methodology. The second strategy, based on optimizing the interface between TiO_2 and the perovskite absorber, [100, 102, 103, 106–112] has been more successful. Very recently, the designing of chlorine-capped TiO_2 nanocrystals demonstrated an unprecedented 20.9% stabilized PCE [110]. A slightly simpler strategy consists in incorporating interlayers such as ionic-liquids [103, 113] or fullerene derivatives [101, 102, 106–108, 114–116]. Although this latter case has been specially studied, it is hard to preserve the integrity of the fullerene layer because of its partial solubility in the solvents used for perovskite deposition [115]. As a result, several alternatives including depositing the perovskite by thermal evaporation [101, 107, 108], chemically modifying the fullerene [102, 114, 115], or depositing additional protective layer atop the fullerene [106] have been studied. A very complete explanation of the fullerene effect on the perovskite p-i-n structure was recently reported [117]. Fullerene

derivatives can act in different ways, firstly suppressing hysteresis, slightly increase the Voc and improve stability in such configuration. On the other hand, when considering flexible n-i-p PSC, the polymeric substrate imposes a sub 150°C restriction on the processing temperature. In that context, the best reported flexible devices relied on a sputtered TiO_2 layer [118, 119]. Strategies employing solution-processed low temperature TiO2 have reached around 10% PCE [120–122]. In both rigid and flexible n-i-p devices, the surface engineering of the TiO_2 is intended for passivating surface defects and suppressing ion migration, which is ultimately critical to achieve highly efficient and hysteresis-free n-i-p devices [110].

In this work, is analized a new method for tratment of the surface of nanoparticle-based solution-processed TiO_2 layer (TiO_2-NP) leading to a unique simultaneous passivation of the top and bottom interfaces of the perovskite n-i-p device structure. Through AFM techniques, we show that this specific modification simultaneously improves the charge transfer from the bottom perovskite contact to the TiO_2 as well as reduces surface trap states enhancing the top perovskite contact with the p-type buffer layer. The developed TiO_2-NP:PC70BM layer is a network of TiO_2 nanoparticles interconnected by fullerene clusters. Due to the particular topography of this layer, fullerene is not dissolved by the perovskite precursor solution [123].

3.2.2 Results

The effective surface modification of a TiO_2-NP layer with the fullerene derivative PC70BM (referred in the following as TiO_2-NP:PC70BM) configures a novel ETL enabling a champion 18.4% PCE in a planar n-i-p PSC Figure 3.5a (The devices of this section were fabricated by John Ciro). In the Appendix A there are the description of fabrication methods for the MAPI, buffer layers TiO_2, TiO_2-pcbm, Spiro-ometad and silver electrodes and their respective thickness. Since non-sintered TiO_2-NPs were implemented, the layer on top is expected to infiltrate. Accordingly, when depositing perovskite directly onto the TiO_2-NP, the perovskite layer is likely to have a direct contact with the ITO semitransparent electrode in detriment of the device photovoltaic parameters. Such is the case for devices without PC70BM as shown in Figure 3.5b. The broad distribution in the statistics of the photovoltaic parameters, particularly in the PCE when the device is fabricated without PC70BM is due to that in some cases, several cells can be in places without pinholes, reaching values as high as 16.6 %. For this sample was not possible determine its stabilized power output (SPO) This behavior has been already reported for devices with severe hysteresis [124, 125]. Incorporating PC70BM into the TiO_2-NP layer strongly enhanced the device.

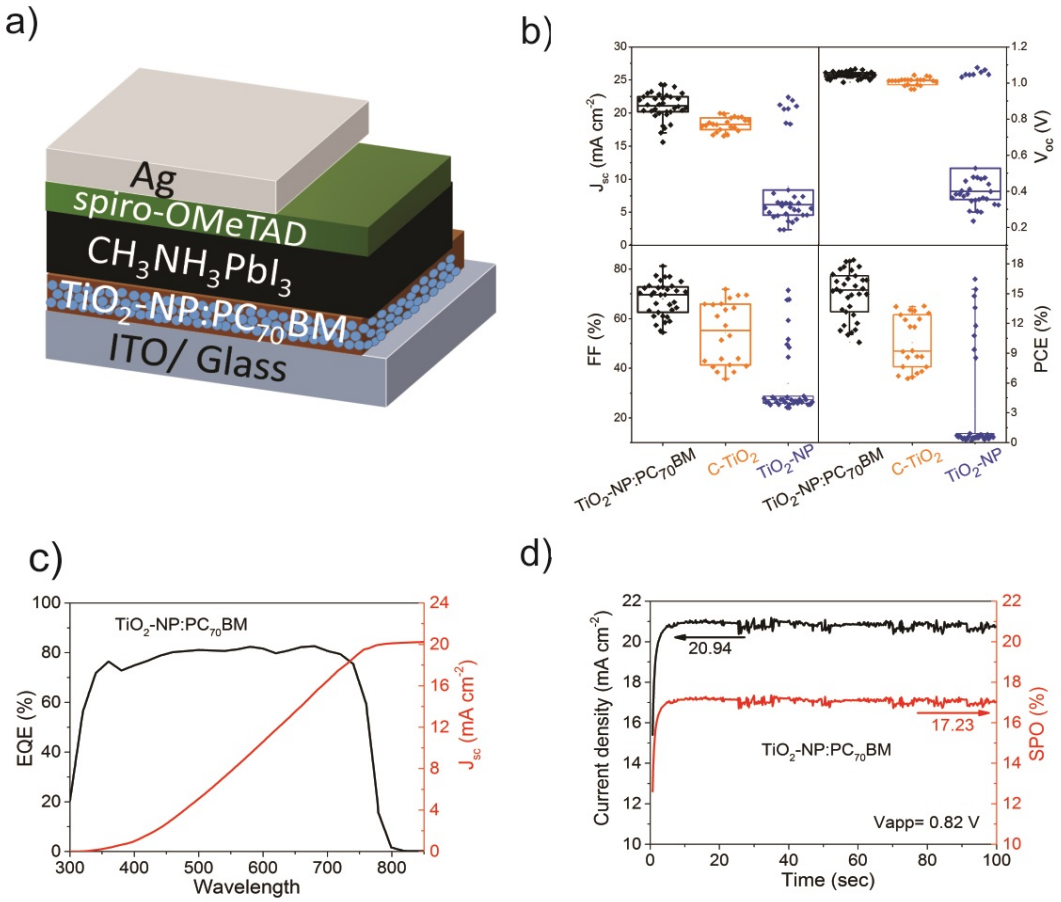

FIGURE 3.5: Enhanced planar perovskite solar cell based on a TiO_2-NP electron transporting layer surface modified with PC70BM reaching a champion 18.4% efficiency. (a) Planar n-i-p device structure. (b) Statistical dispersion of the obtained photovoltaic parameters. (c) EQE and integrated Jsc. (d) Resulting 17.2% stabilized power output.(Image realized by the group for the paper [123])

PC70BM provided compactness to the TiO_2 layer, which is analyzed thoroughly later, enabling devices with high external EQE and SPO reaching 17.2% as shown in Figure 3.5c and Figure 3.5d, respectively. Therefore, the TiO_2-NP:PC70BM layer enabled a significant reduction of hysteresis in the J-V curve of the optimized devices. Previously, the origin of the hysteresis in planar n-i-p solar cells based on TiO_2 was attributed to a contact resistance for electron transfer between perovskite and TiO2 [124]. Here, we observed the same phenomena for solar cells based on TiO_2 -NPs. However, modification of TiO_2 with PC70BM leaded to solar cells with reduced hysteresis.

The optimal performance of the device using a low concentrated PC70BM (3 mg/mL) indicates a successful surface modification of the TiO_2 -NP layer without using PC70BM in excess. Conversely, PC70BM was able to cover possible pinholes in the bare TiO_2-NP surface, which results in an improved interface with the perovskite. This result is

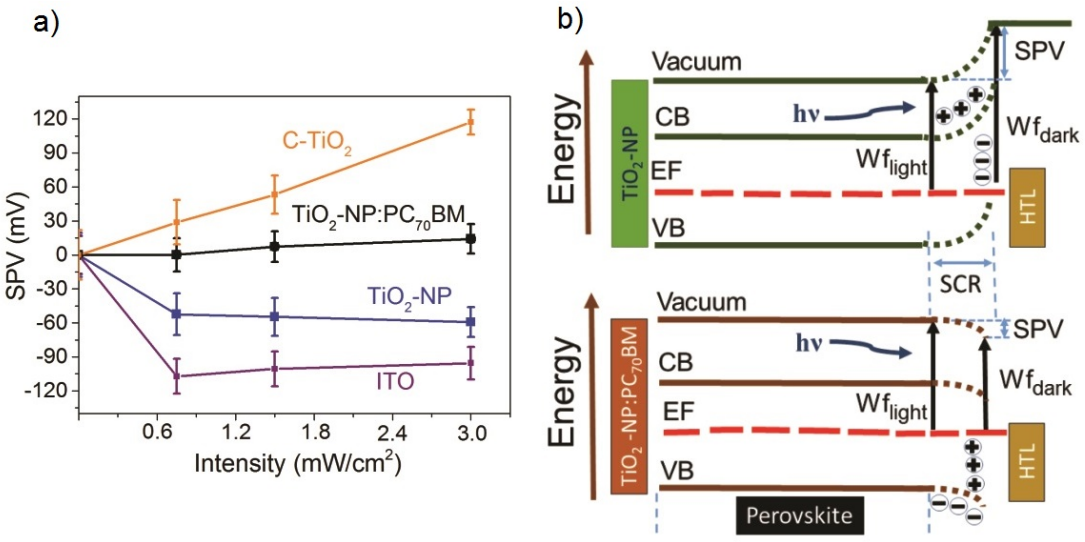

FIGURE 3.6: Effect of the ETL on the superficial electronic properties of the perovskite. Photocurrent of the perovskite deposited on (a) TiO_2-NP:PC70BM and (b) TiO_2-NP layers, respectively. c) Dependence of SPV with light intensity for perovskite films grown on different ETLs. d) Schematic of the band bending at the surface space charge region (SCR) of the perovskite depending on the underlying ETL

consistent with the report by TiO_2-NP Conings et al [126], who state that fullerene is able to infiltrate a nanoporous SnO_2 layer leading to passivation of the metal oxide and the blockage of possible shunt paths [126].

Besides modifying the surface properties of the TiO_2 layer, the PC70BM implementation also enhances the electronic properties of the perovskite grown atop. In fact, the charge extraction at the ETL/perovskite interface was enhanced by the TiO_2:PC70BM layer while simultaneously the resulting grown perovskite exhibited surface donor states on its top interface. As a result, there is a subsequent accumulation of holes at the perovskite surface facilitating charge transfer towards the atop hole transporting layer (HTL) it was proved thorough PL measurements Figure 3.8 showing higher quenching of perovskite PL signal when it is grown over the TiO_2-NP:PC70BM layer. Accordingly, the PC70BM modification of the TiO_2 surface contributes to maintaining photocurrent uniformity all over the perovskite interface.

This result is consistent with results by Wojciechowski et al [102], who found improved electron extraction from the perovskite as a result of fullerene modification of TiO_2 [102]. On the other hand, SPV analysis revealed the changes of the band bending at the surface of the perovskite. Variation of the SPV with the light intensity is shown in Figure 3.6a. As described elsewhere[61, 127] the SPV sign is related to the type of surface states while its magnitude relates to the density of states. A positive SPV corresponds to donor states (surface downward band bending) which accumulate positively charge surface donors at

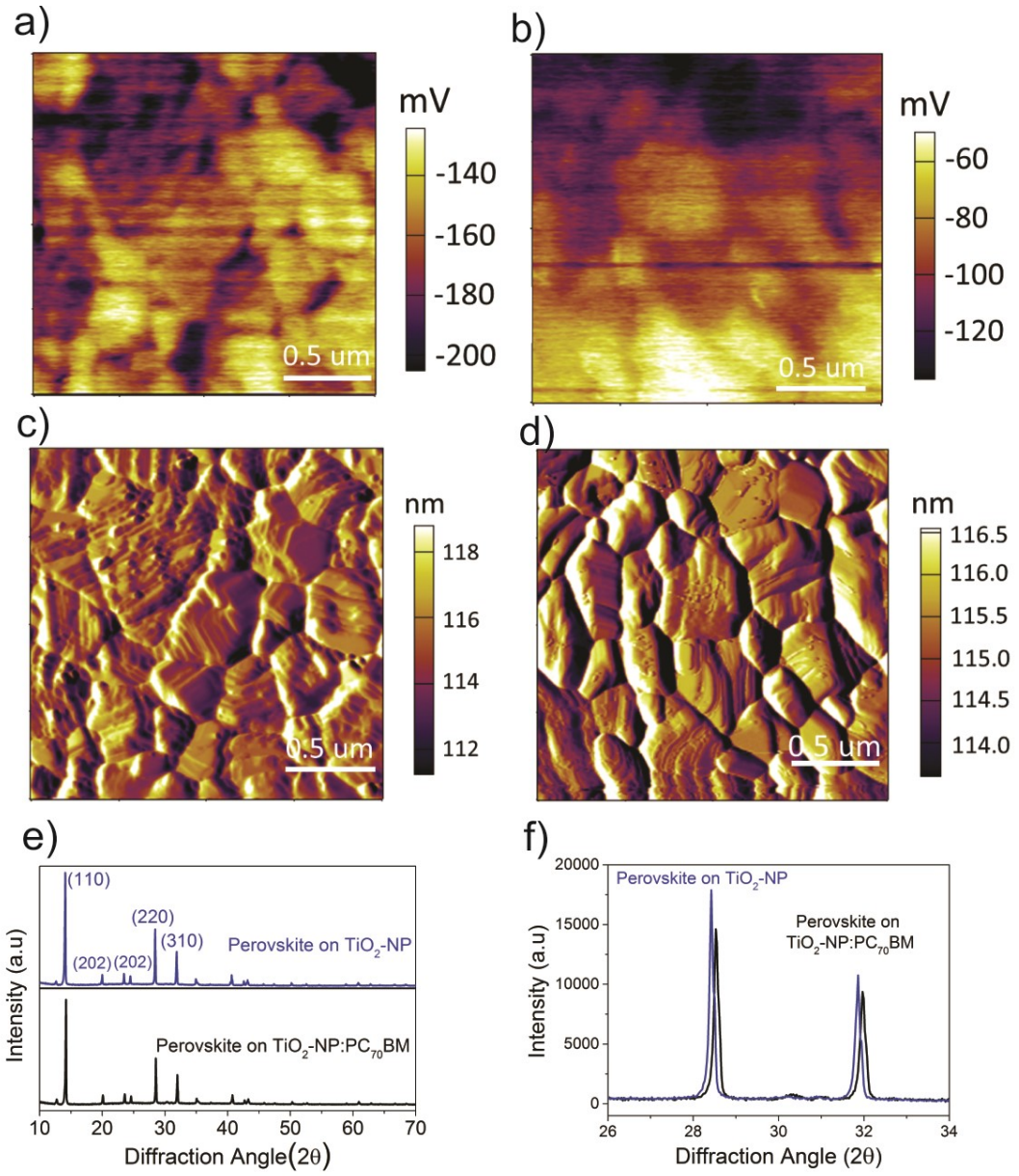

FIGURE 3.7: Electronic and morphologic properties of the grown perovskite depending on the underlying ETL. Contact voltage and retrace amplitude of the perovskite deposited on (a), (c) TiO_2-NP:PC70BM layer and (b), (d) TiO_2-NP layer. (e) Difractogram of the perovskite. (f) Zoom of the overlaid difractograms

the semiconductor surface, while a negative SPV corresponds to acceptor states (surface upward band bending) that accumulate electrons, as shown schematically in Figure 3.6b. In the case of the perovskite grown on TiO_2-NP:PC70BM, positively charged surface donors accumulated at the top perovskite surface which is convenient for the subsequent hole transfer towards the Spiro-MeOTAD HTL because electrons are transferred from the HTL valence band to the surface donor states and from there to the valence band of the

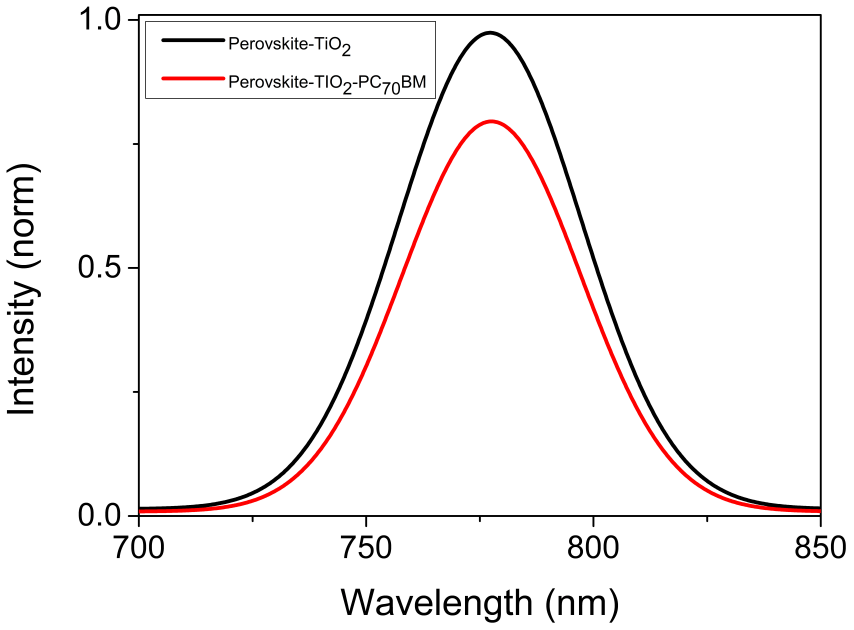

FIGURE 3.8: Steady-state photoluminescence (PL) spectra of the perovskite on TiO_2-NP and TiO2-NP:PC70BM.

perovskite. An opposite behavior was found for the perovskite grown on bare TiO_2-NP where electrons are accumulated in acceptor surface states. Consequently, effective hole transfer at the Spiro-MeOTAD/perovskite interface is hampered by the accumulation of negative charge on the perovskite surface. These changes in the perovskite SPV can be explained by the morphological and superficial differences of the underlying layer. As shown in Figure 3.6a, perovskite grown on bare TiO_2-NP and ITO has negative SPV values, indicating presumably that pinholes on the TiO_2-NP layer allows the contact of perovskite with the ITO electrode. In contrast, an almost flat SPV response was found for the perovskite grown on the TiO_2-NP:PC70BM layer which also happened for the perovskite grown on the pin-hole free C-TiO_2 layer confirming the influence of getting compact ETLs. Hence, the TiO_2-NP:PC70BM layer effectively blocks the contact of perovskite with ITO and change the direction of the surface band bending of the perovskite. Moreover, the lower magnitude of the SPV for the perovskite grown on TiO_2-NP:PC70BM indicated a reduction of surface trap density within the perovskite absorber. This flattening of the perovskite bands reduce the electrostatic barrier for hole transfer across the perovskite/HTL interface [102]. These features have been pointed out as key factors to achieve highly efficient and hysteresis-free PSC [103]. In order to provide insight into the physical mechanism behind the modifications in the electronic properties of the perovskite grown on TiO_2-NP:PC70BM, the perovskite morphology and grain boundaries were evaluated. In first place, the resulting perovskite facets and crystalline structure depended on the underlying ETL, as shown in Figure 3.7.

Since facets are closely related to the photovoltage mapping [49] modifications in the perovskite electronic behavior are clearly anticipated. On the other hand in the net section we verified how the grain boundaries have particular behaviors depending on the sample conditions.

Accordingly, it is not possible to assign a particular charge accumulation at the grain boundaries. From the resulting photovoltaic performance, we corroborate the influence of the TiO_2-NP:PC70BM interface in determining a perovskite with higher optoelectronic quality. In summary, the PC70BM incorporation engineered both interfaces of the perovskite towards enhancing simultaneously the electron and hole extraction, which explains the achieved good performance of the device.

3.2.3 Consclusions

In summary, was analized the surface modification of a TiO_2 layer derived from an ink of dispersed NPs and processed at low temperature (150°C). With the AFM measurements and SPV measurements was showed that fullerene interconnect the TiO_2 NPs in the resulting TiO_2-NP:PC70BM composite layer. Since fullerene results physisorbed into a network of TiO_2 NPs, the perovskite precursor solvent does not remove it. To understand the origin of this high PCE, SPV analysis of the perovskite surface was determinant. We demonstrate that surface modification of TiO_2 not only influence the properties at the ETL/perovskite interface but determines a proper hole transport layer HTL/perovskite interface. It was found that PC70BM surface modification change the direction of the surface band bending within the perovskite semiconductor and reduce its density of trap-states at the interface with the HTL layer. As a consequence, TiO_2 modification by fullerenes enables better charge transfer towards the n-type and p-type buffer layers improving the PCEs until PCEs up to 18.4% and SPO of 17.23%.

Planar PSC devices based on the TiO_2-NP:PC70BM layer reached PCEs up to 18.4% and SPO of 17.23%

3.3 MACl treatment in easy processable perovskite solar cell

3.3.1 Introduction

In recent years, new methods for fabrication of PSCs have been proposed [37, 128–132]. One of the challenge is to produce low-roughness and high quality films, with great

coverage area and large grains to avoid shunt paths and get better transport and optical properties. In spite of the success of most of these methods there are still some issues to be solved. One of the problems, is that due to the grain structure of perovskite films, their boundaries are a source of defects that work as trap states into the band gap limiting the performance of the cell [33, 34, 68, 133, 134]. Other issue to be considered, is that usually these fabrication methods have many difficulties for scaling up and are useful in proof-of-concept devices [135].

In order to solve the first issue, several groups have used Lewis bases such as pyridine [136] and thiopheness [133, 136] to passivate the grain boundaries in the perovskite films, reducing the non-radiative recombination paths leading to increase the open circuit voltage (Voc). In spite of these good results, passivating compounds as pyridine, are very toxic [137] and its use in scaling-up processes is very complicated. Moreover, the thiopheness are usually dissolved in chloro-benzene which difficult the ulterior deposition of electron transporting layers (ETLs) such as PCBM.

The other problem is to find a suitable method to scaling up. There have been several alternatives recently reported. Noel et al [128] developed a new film deposition method based in low boiling point solvents (acetonitrile ACN deposition route). This method does not require additional solvents nor vacuum flash nor gas annealing. In spite of their great advantages to get high efficiency and easy fabricated solar cells, this technique requires the addition of MACl in order to get high performance solar cells.

To explore the influence of the MACl in the bulk and micro-scale properties of the $CH_3NH_3PbI_3$ grown by the ACN deposition route, it is combined steady state PL, AFM, KPFM, and SPV. Based on these measurements, we propose a mechanism of reduction of electron barriers when the light interact with the MACl modified film. Additionally, we proved how the ACN route produce very homogeneous perovskite films in comparison with layers fabricated by the solvent engineering (SE) method. As a result, high-quality pin-hole free perovskite layers could be deposited in large area substrates opening a new route for the fabrication of efficient solar cell modules.

3.3.2 Results

In order to see the difference of the solar cell performances due to the MACl treatment on the $CH_3NH_3PbI_3$ perovskite, were fabricated PSCs in a p-i-n configuration. Glass-ITO was used as substrate, nickel oxide (NiO_x) as HTL, PCBM as ETL, and silver as metal electrode (See Appendix C for experimental details).

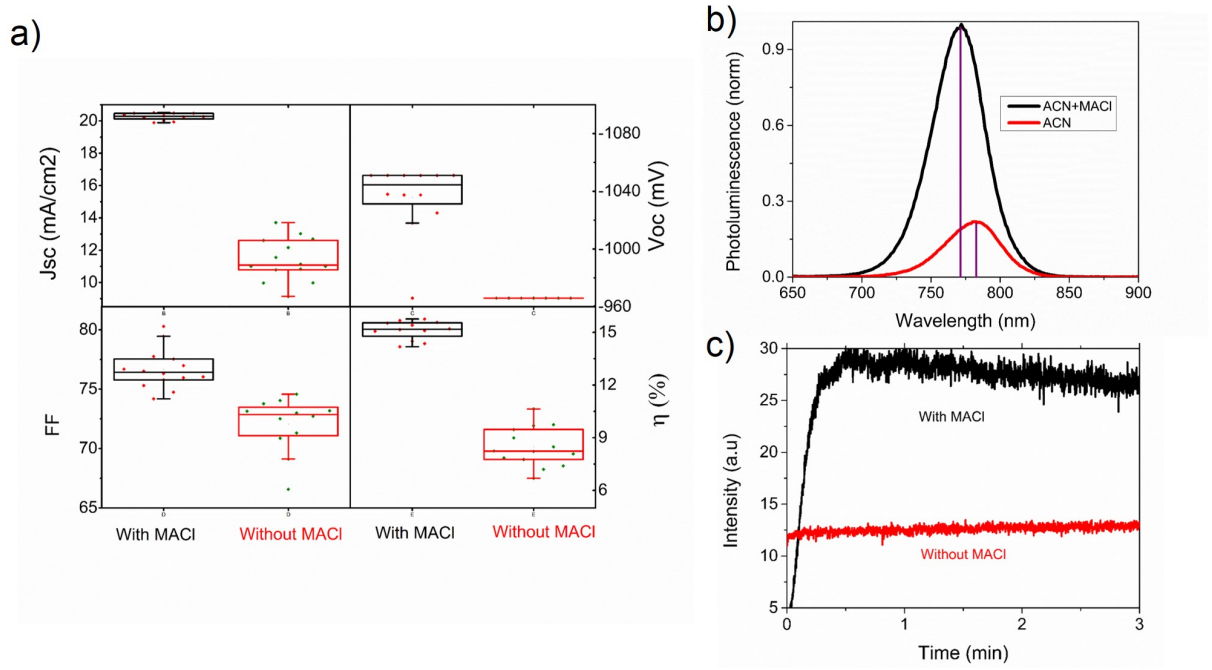

FIGURE 3.9: Enhancement of photovoltaic and optical properties by MACl treatment of perovskite layers. a) Statistical dispersion of photovoltaic parameters. Steady-state (b) and (c) transient photoluminescence of $CH_3NH_3PbI_3$ perovskite layers

	Jsc (mA/cm^2)	Voc (mV)	FF (%)	η (%)
Forward (With MACl)	20.17 ±0.2	1048.6 ±6	73.0 ±1.1	15.41 ±0.3
Reverse (With MACl)	20.4 ±0.1	1040.8 ±11	70.5 ±2.8	14.8 ±1.3
Forward (Without MACl)	10.97 ±1.2	965.9 ±21.9	76.7 ±6.27	8.5 ±1.1
Reverse (Without MACl)	10.9 ±1.3	932.5 ±24.3	56.0 ±5.48	5.7 ±1.1

TABLE 3.2: Photovoltaic parameters of PSC produced by the ACN method with and without MACl

Figure 3.9a shows the statistical dispersion of the photovoltaic parameters of PSCs fabricated from the ACN precursor with and without MACl. There are clearly improvements in the short circuit current density (Jsc) and in the open circuit voltage (Voc) when MACl is added. There is also a slightly enhancement in the fill factor (FF). The mean and champion values of the fabricated devices are shown in Table 3.2 whereas the champion device J-V curves are depicted in Figure 3.10a, b. It is notable how the cells without MACl present significant hysteresis which is significantly suppressed when the additive is included. The EQE and their respective integrate current density for the perovskite with and without treatment are shown in the Figure 3.10c. The EQE exhibited an almost flat response along the absorption band of the perovskite resulting in an integrated 19 mA/cm^2 short-circuit current for the perovskite with MACl treatment, without the MACl treatment the integrated current is 17.9 cm^2. This value without MACl is higher than the Jsc obtained of the J-V measurements. The EQE is taken

with an lower intensity than the solar simulator, and as was demonstrated with the SPV measurements, the transport properties of the perovskite changes with the light intensity. Particularly as the light intensity is increased the perovskite without MACl decrease their transport properties, but with MACl treatment an increase in the light intensity improve their transport properties.

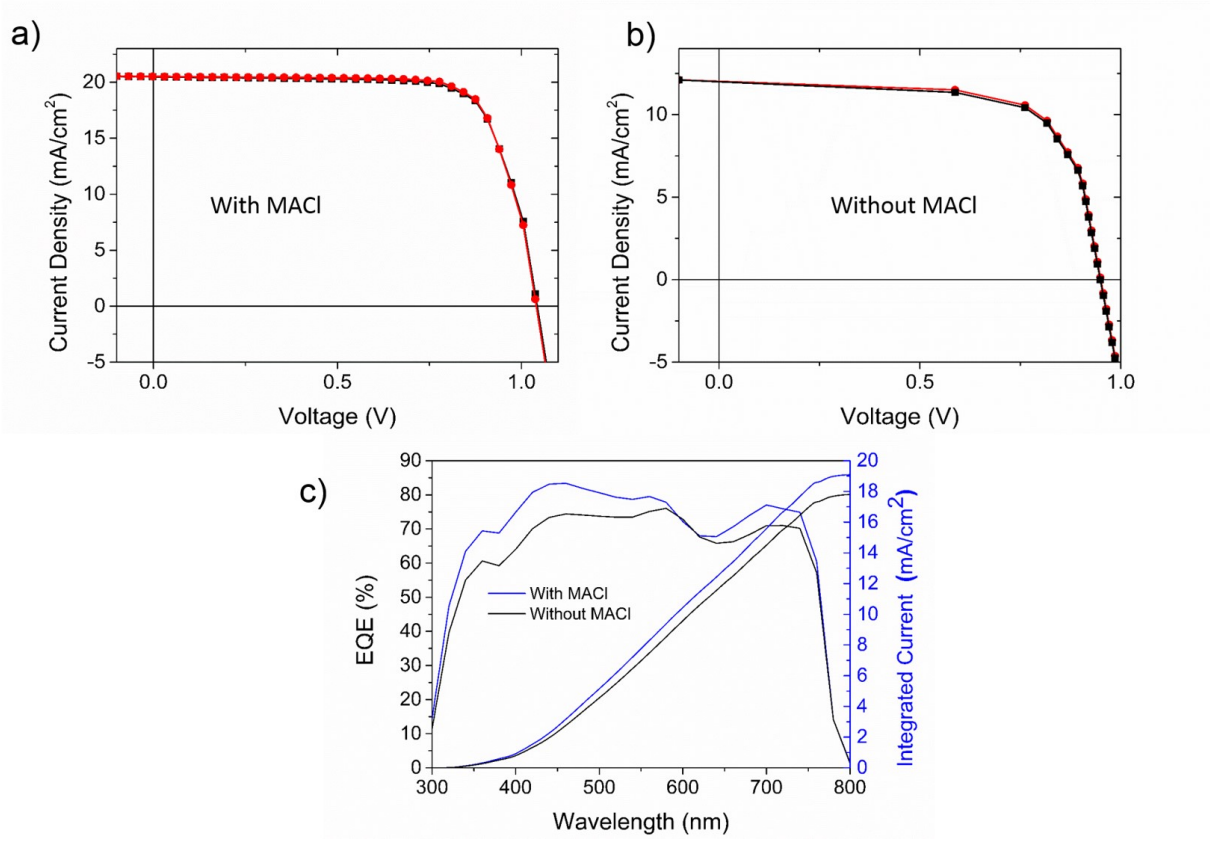

FIGURE 3.10: J-V curves of the champion device under forward and reverse scans (a) with MACl, (b) Without MACl, and (c) EQE spectra of the devices with and without MACl surface treatment.

The differences in all the photovoltaic parameters of the perovskite with and without MACl should be attributed to changes both in the physical or chemical properties of the perovskite. Chemical changes could be due to stoichiometric changes produced by the incorporation of the MACl in the perovskite structure as mentioned later in the XRD analysis. Physical changes should be mainly due to improvements in the optical or transport properties as consequence of higher crystallinity, enhanced morphology as well as defects passivation. In the following will be discuss each of these factors.

In order to explore what kind of optical process are improved by the MACl treatment we performed steady-state and transient PLmeasurements. Figure 3.9b shows PL spectra of perovskite films with and without MACl. Clearly, the MACl treatment produce a significant increase in the PL intensity. Thus, perovskite films with MACl have bigger

radiative recombination than those without MACl, implying that the surface treatment reduce the non-radiative recombination. This behavior is a consequence of reduction of trap states which should be reflected in the increase of Voc (Figure 3.9a)[25, 36]. Moreover, it is observed a change in the position of the PL maximum, as the onset in the absorption spectrum does not have changes [138] (see Figure 3.11)a this indicate differences in stokes shift of the perovskite. This result can be explained because photo-generated carriers relax into lower energy states and predominately emit from the lowest bandgap domains [139]. In Figure 3.9b transient PL is reported. It can be observed that films without MACl do not reach the PL maximum. Previously, the longer transient response of PL was assigned to a stabilization of the system as a product of trap state filling. Hence, the films without MACl do not reached a stabilization which is an indication that different kinetics and trap states control the process in longer periods of time [35].

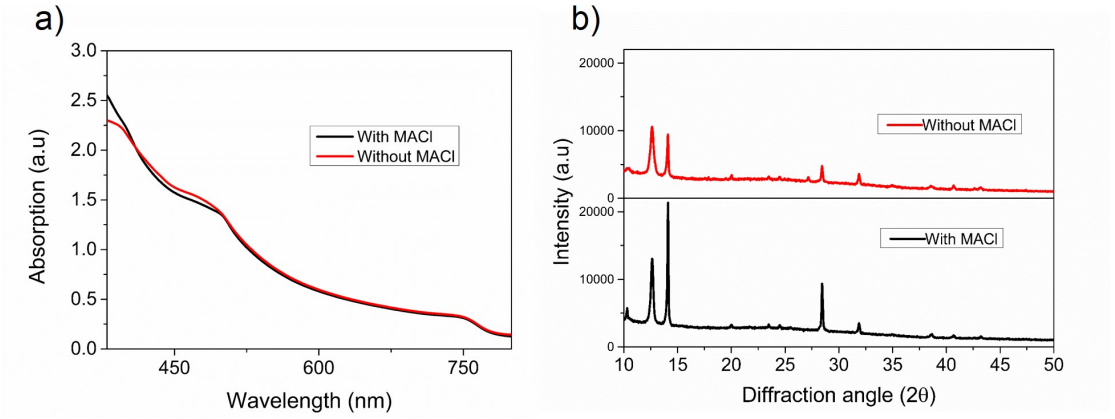

FIGURE 3.11: Absorption spectra of the perovskite films with and without MACl treatment

Figure 3.13 shows the morphology and the surface potential of perovskite layers fabricated by the ACN route. It is observed a big change in the morphology of films with and without MACl treatment. Layers without MACl present similar grain structure to perovskite films fabricated by the solvent engineering method (SE) (Figure 3.14) with average grain size of 250 nm. As MACl is added the morphology changes. Interestingly, the grains are so much bigger and two types of grains were observed; one with a rod shape and average size of 1 μm and other with more symmetrical extension. In order to confirm that these images are not tip artifacts, we took SEM micrographs as shown in Figure 3.14. The effect of grain size on the recombination kinetics was analyzed in previous articles [75]. It was found that perovskite films with bigger grains have longer diffusion length leading to improvement in the current density. Moreover, in the XRD images (Figure 3.11b) is observed an increase in the intensity of the peaks which means more grade of crystallinity along with the decrease in the PbI_2 peak, indicating that

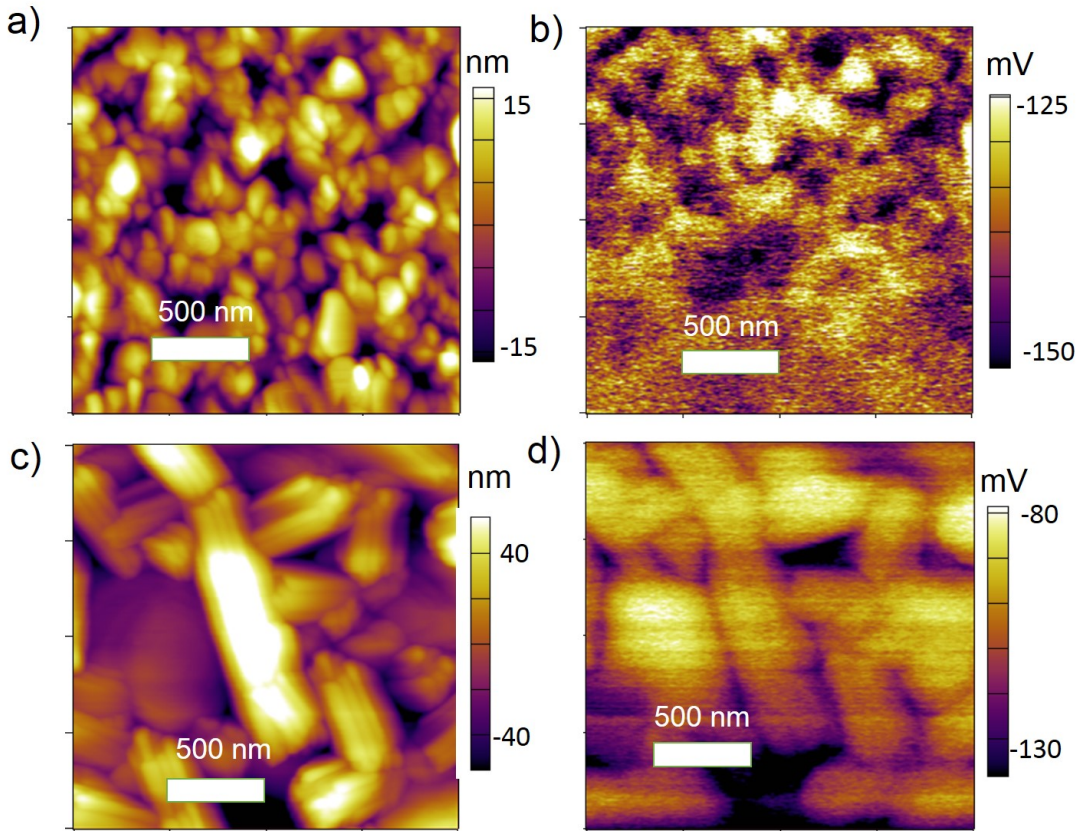

FIGURE 3.12: Topography images (2x2) μm of perovskite layers without (a) or with MACl (c) Surface potential under dark ACN method. Perovskite films without MACl (b), with MACl (d)

MACl helps to complete the stoichiometry of the perovskite . Films without MACl present higher proportion of PbI_2, which is reported to be as harmful to the device performance [140].

The surface photo voltage (Vcpd) of the films with and without MACl treatment are shown in Figure 3.15. The Vcpd images of the films without MACl treatment before illumination and after illumination are displayed in Figure 3.15c and Figure 3.15d respectively. The Vcpd images of the films with MACl treatment in dark and under illumination are shown in Figure Figure 3.15e and Figure 3.15f, respectively.

The average in dark allows to calculate the work function of the films. A potential difference of around 50 mV was found between the perovskite with and without MACl. As the energy is qV, their work functions differences should be 50 meV, this average was taken on 2x2 μm surface potential images in order to have better statistics Figure 3.12. Perovskite surface with MACl has less negative potential (small work function), which means it has more n-type behavior than the perovskite surface without the treatment. This difference in the character of the perovskite should be an indication of differences

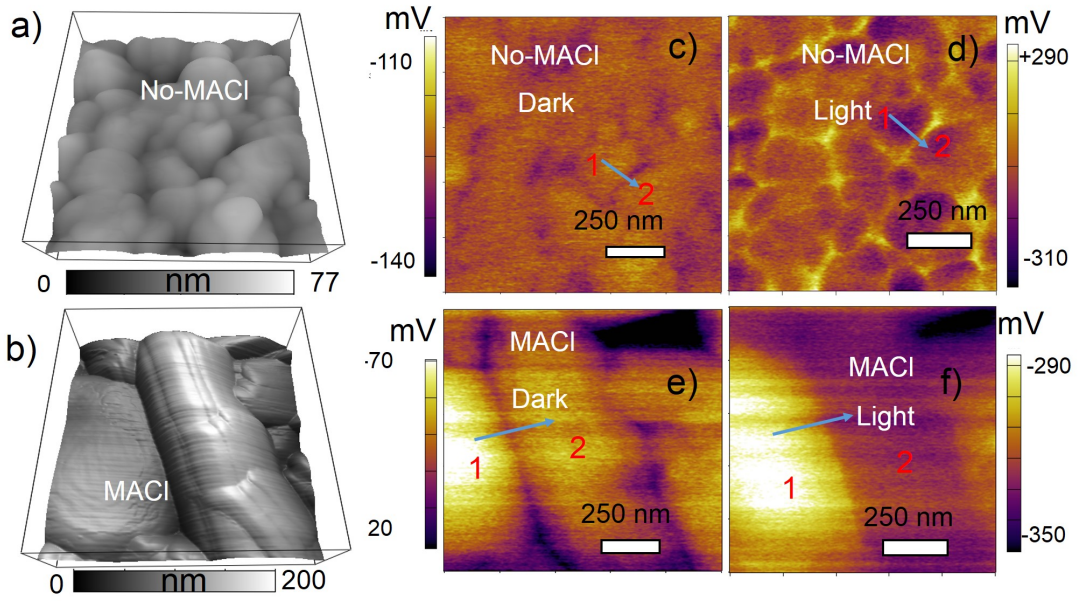

FIGURE 3.13: Topography images of perovskite layers with (a) or without MACl (b) Surface potential and morphology of perovskite layer deposited by the ACN method. Surface potential images (1x1μm) of perovskite layers with (c), (d) and without MACl (e), (f)

of the position of defect levels, showing that without the treatment the defects could be deeper, and after the treatment defects are closer to the band edge, which is in agreement with the improvement observed in the Voc for the MACl treated perovskite. Besides this change in the work function, other electronic changes can be analyzed from the microstructure.

To analyze the influence of the MACl treatment in the microstructure, it is focused on the interface between two characteristic grains. In darkness, the different grains with and without MACl treatment present differences in the surface potential (see Figure 3.13c and Figure 3.13d) as was analyzed in previously reports [49]. Particularly in the MACl treated samples it is clear how the rod shape grains (grains 1) show more negative potential than the most symmetrical shape grains (grains 2). These potential difference between grains can be attributed to different facets of the perovskite structure with each facet having different energetic distance between the vacuum and Fermi level in each direction in the reciprocal lattice. It should be noted that although this fact was analyzed by Sibel et al [49], is more evident in this samples the relation between the possible facets and the surface potential. Additionally the grain boundary shows a more negative potential, and consequently the biggest work function of the film (rode shape grains) show more negative potential than the (symmetric grains) Figure 3.13a and Figure 3.13b. We attribute this potential difference between grains to different facets of the perovskite structure with each facet having different band edges in the K space.

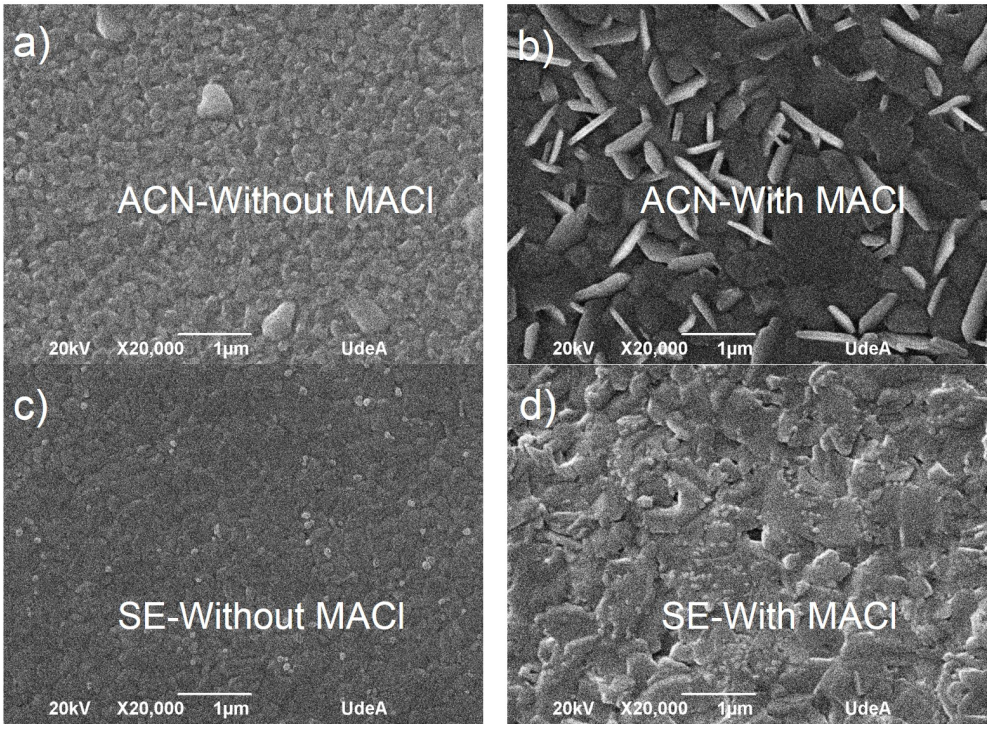

FIGURE 3.14: SEM images of the perovskite fabricated by the ACN route without (a) and with MACl (b), and fabricated by the SE route without (c) and with (d) MACl.

Moreover the work function (WF) of the MACl-treated perovskite is smaller compared to films without MACl. Additionally both samples with and without MACl, the grain boundary shows a more negative potential, and consequently (the biggest work function of the film). This difference in the WF creates an effective electric field between the grains and their boundaries which could influence the transport of carriers and affect the Voc and Jsc by trap states located at grain boundaries defects, and potential barriers, respectively.

So the bigger work function implies a downward band bending of the semiconductor as a product of negative charge accumulation as was explained in the previous sections of this chapter. After illumination, the surface voltage of the grains and their boundaries with and without MACl present a completely different behavior. Without MACl the grain boundaries present a bigger potential than the grain bulk which is an indication of a change in the direction of band bending at the boundaries. In contrast, films with MACl present less pronounced potential differences between the grain bulk and boundaries and therefore a continuous surface photovoltage profile is observed (Figure 3.15b). Thus, MACl surface treatment has a passivating effect of the traps located at the grain boundaries. In order to model the observed surface voltage behavior at the grain bulk and their boundaries is schematized in Figure 3.15c and Figure 3.15d a plausible mechanism of lateral charge transport in the perovskite films. For films with

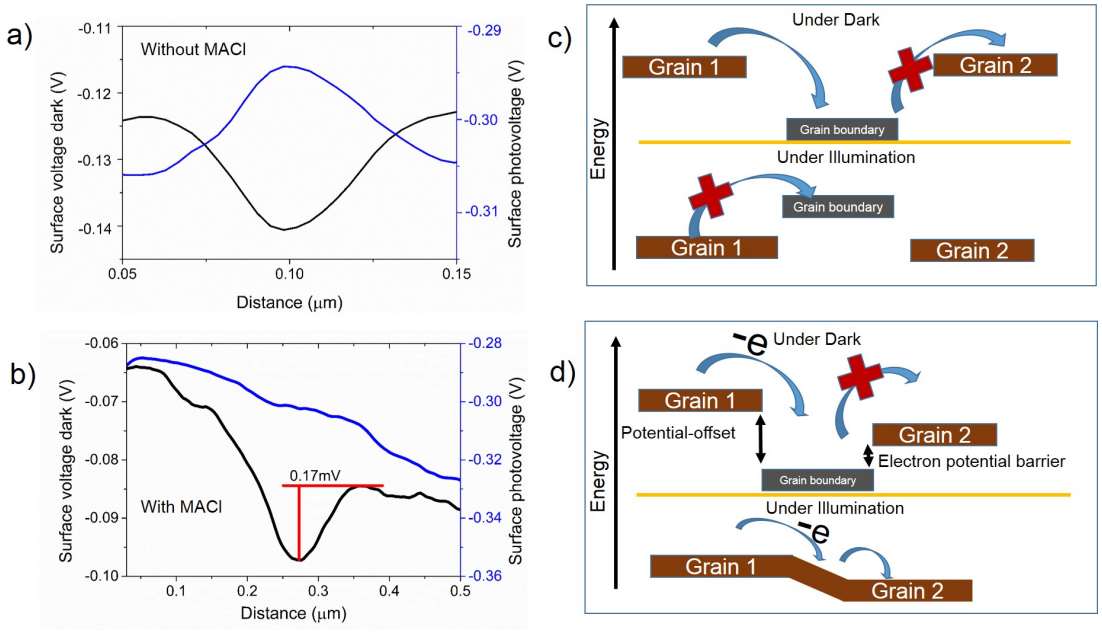

FIGURE 3.15: Spatial variation of surface voltage and photovoltage for perovskite films with (a) or without (b) MACl surface treatment black lines before illumination and blue after illumination. Schematic diagram of charge transfer between grains for perovskite films with (c) or without (d) MACl treatment

MACl, the electrons can be trapped in a potential well at the grain boundaries in dark conditions whereas a good potential junction favorable for charge transfer across the boundaries is formed between the grains under illumination. In contrast, films without MACl treatment display a potential barrier at the grain boundaries under illumination. As a hypothesis the passivation of the grain boundaries along with the elimination of potential barriers in the samples with MACl treatment help to avoid the non-radiative recombination and facilitate the lateral charge transfer. These results of surface photovoltage analysis are in agreement with the increase in the PL signal as well as the improvements of the Voc and Jsc observed in Figure 3.9

After realizing the importance of the MACl treatment in the perovskite by the ACN route in small solar cells, were fabricated 10x10 cm films and mini-modules as the next step in the scaling up process, as shown in Figure 3.16. It is compared the morphology of large area films and performance of the modules with other ones fabricated by the SE route. To see the advantage of the ACN process, were took AFM images in different points of the modules, one at the center of the film and other at a radial distance of 4 cm, to the edges as shown in Figure 3.16c-f. Clearly, films made by the solvent engineering technique present in some place wave-like forms due to difficulties to generate uniform films on large areas by this method. This result demonstrates that this technique has difficulties for scaling up processes. In contrast, the film by the ACN route shows more

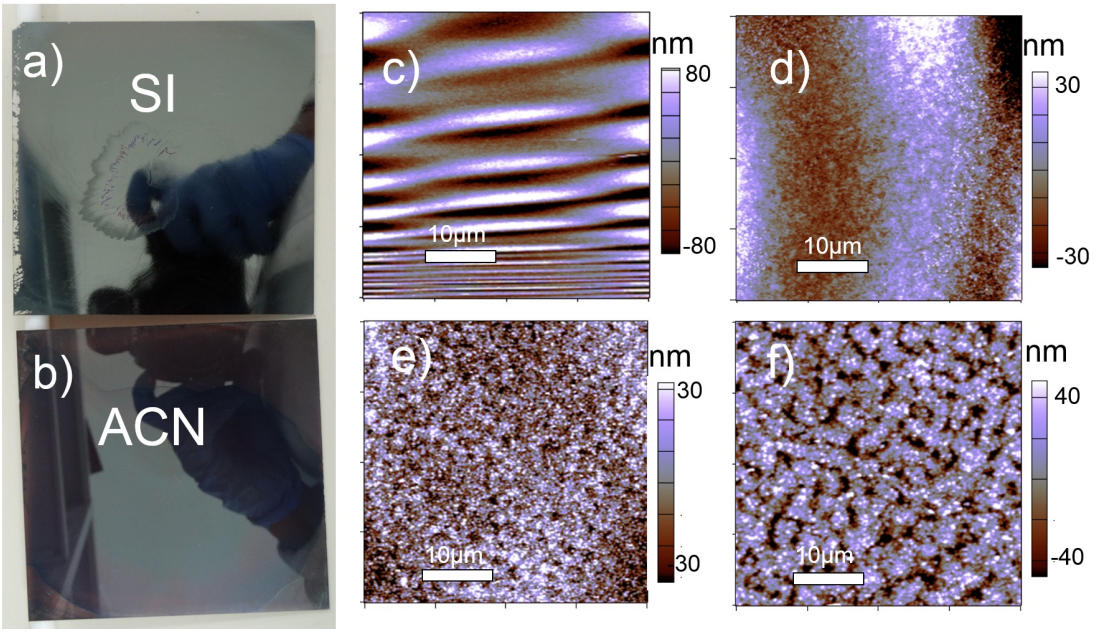

FIGURE 3.16: Characterization of perovskite films on large area substrates (10x10 cm). Photographs of perovskite films deposited by SE (a) and ACN (b) techniques. AFM images of perovskite films deposited by SE (c and d) and the ACN techniques (e and f). The AFM images were took at the center (c and e) and at a distance of 4 cm to the edge of the substrates (d and f)

homogeneity only with small variations in the coverage area near to the edges of the films. Moreover, the reproducibility of the photovoltaic parameters and performances of the modules with the perovskite fabricated by the ACN route is quite superior than the modulus fabricated by the SE technique. This results together with the passivation with MACl shows than the ACN route together with a deposition of a passivating material like MACl are the one of the most promising technique for the scaling up of the $CH_3NH_3PbI_3$ perovskite.

3.3.3 Conclusions

In this section was proved the importance of the MACl treatment in the perovskite fabricated by the ACN route. It was analized the change of the morphology of the perovskite after the MACl treatment, the size increase in the grains, and the passivation of defects in grain boundaries as a product of the interaction with light.

Through surface voltage was found for films with MACl, the electrons can be trapped in a potential well at the grain boundaries in dark conditions whereas a good potential junction favorable for charge transfer across the boundaries is formed between the grains

under illumination. In contrast, films without MACl treatment display a potential barrier at the grain boundaries under illumination.

This changes produce more efficient solar cell as a consequence of increases in the Jsc and the Voc. With this high performance solar cell were fabricated solar cell modules and compared with another modules fabricated by SE route, showing that the ACN route is a very promising technique for the perovskite scaling up due to its homogeneity in the morphology and their passivated grains after their interaction with light.

Chapter 4

Conclusions

4.1 General Conclusion

Was showed through different characterization techniques, particularly by AFM, and their associated techniques the influences of the properties of different buffer layers, their surface modifications in the photovoltaic parameters, and performances of PSCs. Moreover we conclude that the surface and interface interaction between the different layers of the PSCs play a big role in the design and fabrications of the perovskite devices.

4.2 Specific Conclusions

4.2.1 Influence of selective layers and architecture

- Was found through AFM, and KPFM how the morphological and electronic properties of the HTL, CuO_x, CuSCN and NiO_x affect drastically the photovoltaic parameters and the performances of the PSCs. The CuO_x films through the methodology worked, did not present good surface to the perovskite growing, either in the Cu_2O or CuO phase. In spite of CuSCN presented and homogeneous morphology, high performance devices were not achieved. This results is a consequence of negative band misalignment which allow transport of electrons in the CuSCN valence band, and as a consequence decrease in the Jsc and FF. In the other side the NiO_x presented nice morphology, good conductivity, and low band alignment losses, which allow high an increase of all photovoltaic parameters and as a result high performance devices.

- Through IMKPFM, photoluminescence maps and KPFM was shown how the addition of NiO_x as a HTL and Al_2O_3 scaffold insulator change the surface band

bending and the recombination properties of the MAPI. We interpret this relationship in terms of the surface structure and conclude by IM-SKPM that mesoporous structures tend to have more traps. These films are more stable and thus show a resistance to PL degradation over time as was seen on HF films while simultaneously exhibiting higher PL intensity.

4.2.2 Surface modification in selective contacts

- Was analyzed the surface modification of a TiO_2 layer derived from an ink of dispersed NPs and processed at low temperature (150°C). With the Atomic Force microscopy (AFM) measurements and surface photovoltage measurements we show that fullerene interconnect the TiO_2 NPs in the resulting TiO_2-NP:PC70BM composite layer. Since fullerene results physisorbed into a network of TiO_2 NPs, the perovskite precursor solvent does not remove it. To understand the origin of this high PCE, surface photovoltage (SPV) analysis of the perovskite surface was determinant. We demonstrate that surface modification of TiO_2 not only influence the properties at the ETL/perovskite interface but determines a proper hole transport layer (HTL)/perovskite interface. It was found that PC70BM surface modification change the direction of the surface band bending within the perovskite semiconductor and reduce its density of trap-states at the interface with the HTL layer. In consequence, TiO_2 modification by fullerenes enables better charge transfer towards the n-type and p-type buffer layers improoving the PCEs until PCEs up to 18.4% and SPO of 17.23%.

- Was elucidated the role of the Rhodamine interfacial layer on the enhancement of PCE and operational stability of p-i-n planar PSCs. On the other hand, AFM characterization allowed us to explain the effect of Rhodamine on the improvement of the photovoltaic parameters of PSCs. Despite that Rhodamine has little impact on the topography of the PCBM layers, it induces an important change on its surface electronic properties. Surface potential measurements demonstrate that Rhodamine passivates surface trap states leading to reduced non-radiative recombination. Moreover the Rhodamine layer changes the electrode work function allowing a better miss-match with the ETL. Accordingly, p-i-n planar PSCs including Rhodamine achieved the highest reported PCE up to 16.8%. This section contributes to a better understanding of the operational mechanisms of PSCs, specifically about the pivotal role of proper interfacial engineering at the metal-cathode/organic-semiconductor interface.

- We showed the importance of the MACl treatment in the perovskite fabricated by the ACN route, we proved how the morphology of the perovskite change after the

MACl treatment, the grains increase the size, and there is passivation of defects in grain boundaries as a product of the interaction with light. This changes produce more efficient solar cell as a product of increases in the Jsc and the Voc. With this high performance solar cell we fabricated solar cell modules and we compared with another modules fabricated by SE route, showing that the CAN route is a very promising technique for the perovskite scaling up due to its homogeneity in the morphology and their passivated grains after their interaction with light.

Chapter 5

Perspectives

As a mandatory perspective is the implementation of another CuO_x precursor method, and films fabrication, in order to have better CuO_x films and try to grow this material at low temperatures. Another approximation is a surface modification of this film, similar to that we used in the TiO_2-PCBM treatment, or the rhodamine-PCBM modification

Future work will focus on particular grains facets to better understand the electronic mechanism in each particular case, and also look the evolution in time of the performance to establish if some facets in the surface are likely to changes in recombination process, degradation and decrease of the performance.

As future interesting work is the understanding of the difference in ion movement when is used different structures and different Buffer layers. Moreover how the structure and the buffers help or limit this movement when we applied an external electric field. This can be studied through KPFM and impedance techniques.

Appendix A

Experimental Methods

In this chapter we describe the different experimental methods to make and characterized the samples.

A.1 Solutions and Films deposition

The perovskite technology as a 3 generation solar cells, fundamentally requires that almost all the layers that conform the cell should be fabricated by solution processing methods. Particularly, in this work almost all the layers were fabricated by spin coating process that is on of the best technique to prove concepts previous to a scaling up process. As a advantage of this work, the fabrication of all the layers did not require the use of glove-box camera (in spite that we have it) and the cells are fabricated in air with a control of humidity with a dehumidifier system. The home made chamber with the humidity control is shown in the Figure A.1. Moreover in the Figure A.2 is shown the most used characterization devices used in this work as the AFM, Solar simulator, semiconductor Keithley device, UV-VIS and PL system, EQE and profile-meter system.

The photograph of our standard device composed by 8 subcells of 9 mm^2 is presented in the Figure A.3

Below we describe in a list, the parameters used for the preparation of the precursor solutions or colloidal dispersions, fabrication of the films, and parameters used in characterization of the materials and films.

- **Clean substrate and treatment process**

  The substrates for the P-I-N structure were ITO coated glass from (Naranjo Company). The substrates were washed in the usually 3 steps ultrasonic bath of 5

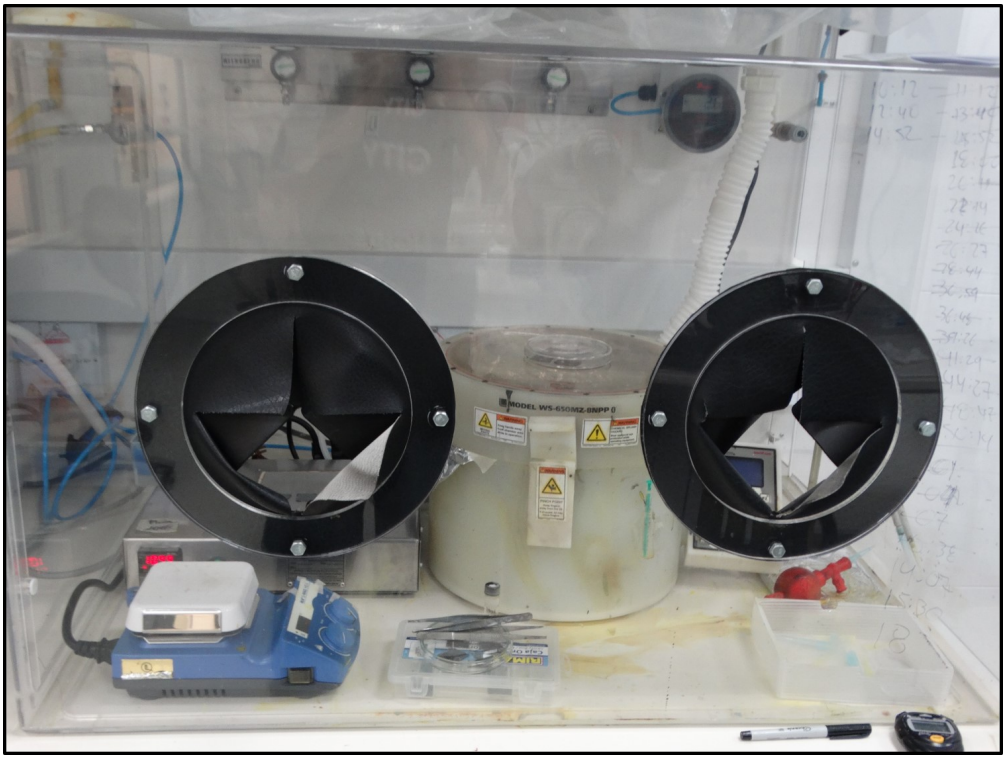

FIGURE A.1: Spin coater device and home made chamber for the humidity control

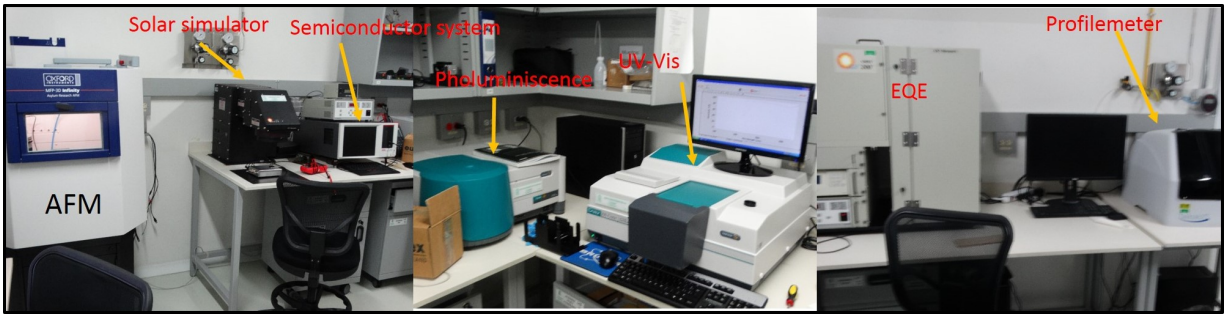

FIGURE A.2: The most used device system for characterization of solar cells and films

minutes with the solvent (water, acetone, isopropanol). Then, ultraviolet ozone (UVO) treatment was done for 5 min at 100°C.

- **NiO_x films**

  The NiO_x hole transporting material was synthesized by using the precipitation method, previously reported by the group [58].

  $Ni(NO_3)_2{\cdot}_6H_2O$ (1.4g, Merck) was dispersed in 1 mL deionized water to obtain a dark green solution. The pH of the solution was adjusted to 10 by adding a NaOH solution (10 M, Sigma Aldrich). The colloidal precipitation was thoroughly washed with deionized water twice, and dried at 80°C for 12 h. The obtained green powder was then annealed at different temperatures for 3 h to obtain a dark-black

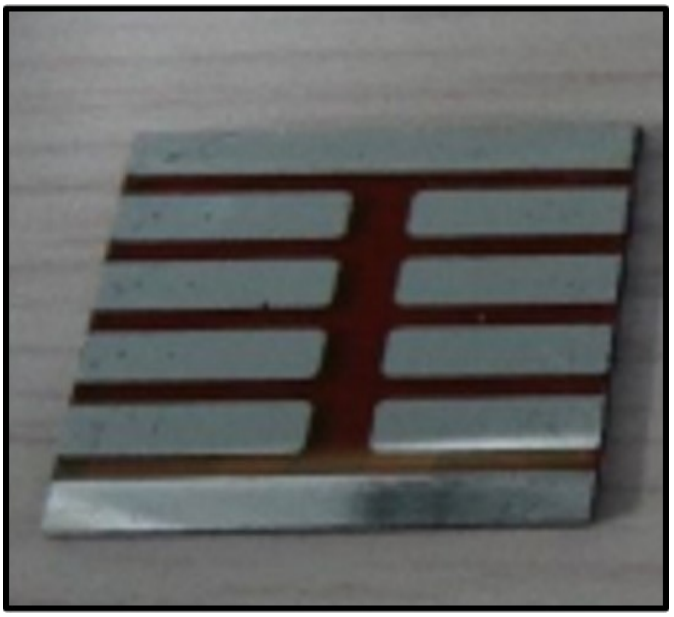

FIGURE A.3: Standard device fabricated in all the work, 8 sub-cells are arranged in one substrete of 1x1 inch

powder.The resulting NiO_x powder was dispersed in deionized (DI) water to a 23 mg/mL and spin coated at 3000 rpm for 30 s with a 3 s ramp.

- **CuO_x films** A mix of 0.02 molar copper acetate monohidrated $Cu(CO_2CH_3)_2 \cdot H_2O$ and 0.04 molar glucose $C_6H_{12}O_6$ in 50/50 water 2 propanol is shaked 20 minutes. The films are deposited at 4000 RPM 30 s. The films were annealed at 220, 260 or 280 ^oC for 5 min. The obtained films were around 20 nm measured by profile-meter.

- **CuSCN films**

  To make the precursor solution of Copper thiocyanate CuSCN, 15 mg/ml and 10 mg/ml of CuSCN sigma is prepared dispersing the powders in dipropil-sulfide. The solution is left stirring 24 hours. The layers were fabricated by spin coating at 4000 rpm for 30 s. The films obteined were around 8 and 15 nm of thickness.

- **TiO_2 films**

  The electron-transporting layer was fabricated by spin coating an aqueous 25 mg/mL nanoparticles dispersion (Anatase TiO_2, average diameter of 5 nm purchased from NanoAmor Inc.) at 3000 rpm for 30 s with a 3 s ramp and drying at 100 °C for 20 min.

- **Al_2O_3 films**

  The mesoporous Al_2O_3 layers were deposited by spin-coating solutions of commercial alumina nanoparticles dispersion (50 nm Sigma Aldrich) diluted at 1:5,

1:3 volume ratio of dispersion:isopropanol to give 100 nm and 200 nm films. These films were then dried overnight under ambient conditions.

- **$CH_3NH_3PbI_3$ films**

  To obtain a 400 ± 10 nm perovskite layer, a precursor solution of methylammonium iodide (Dyesol) CH_6IN and lead iodide PbI_2 (Alfa Aesar; 1:1 molar ratio; 55% wt.) in N,N-dimethylformamide (DMF) was deposited by spin-coating at 4000 rpm for 25 s. During spinning, 500 μL of Diethyleter (Aldrich) were dropped on the substrate after 10 seconds and the films were annealed at 65 °C for 1 min and 100 °C for 10 min.

- **ACN perovskite films**

  For the deposition of the perovskite layer with ACN perovskite a 0.5 M solution of 1:1.06 MAI (Dyesol) to PbI2 (99% purity) in the ACN/MA solvent was spincoated onto the substrate at 2000 rpm for 45 s, in dry air, resulting in the formation of a smooth, dense, perovskite layer. A post treatment of methylammonium chloride (MACl) was then carried out by dynamically spincoating 100 ml of MACl (Alfa Aesar, 5 $\frac{mg}{ml}$ in isopropanol). The substrate was then heated at 100 C for 60 mins.

- **PCBM films**

  The phenyl-C61-butyric acid methyl ester (PCBM) (1-Material) was deposited via spin-coating a 20 mg/mL solution in chlorobenzene (CB) at 2000 rpm for 30 s.

- **Rhodamine treatment**

  Rodhamine 101 was deposited on top of the PCBM layer by spin coating a 0.5 $\frac{mg}{L}$ solution at 4000 rpm for 30s

- **Silver electrodes**

  100 nm silver electrodes were thermally evaporated under vacuum (6x10^{-6} mbar) at a deposition rate around 0.1 nm/s .

A.2 Films characterization

- **Atomic Force Microscopy- characterization**

  AFM, KPFM, SPV and IMKPFM measurements.The SPV and topographic 5X5 μm measurements where performed in a MFP-3D AFM (Asylum Research) with the tips used were Silicon Ti-Ir coated (Asyelec-01) with nominal spring constant of 2.89 N/m and resonance frequency of 71.7 KHz. IM-KPFM data were taken with mapped using tapping mode MFP-3D-BIO with Pt 300 KHz resonance frequency

tips. For the local PL and IM-KPFM measurements, were realized by keeping the sample in a flow cell continuously purged with nitrogen gas, a laser of wavelength 488 nm was used. The flow cell sits on a XY piezo stage placed on a Nikon Eclipse T2000-U inverted confocal microscope (MFP-3D-BIO) . The piezo stage is controlled by an Asylum Research MFP-3D AFM controller and software. For PL measurements, a 488nm laser is pulsed at 400 Hz and attenuated using a variable ND filter wheel and then coupled into the confocal microscope using a single mode fiber. While the laser raster scans the sample, a fraction of the fluorescence is collected by the objective and goes through the same beam splitter, the light is then filtered by two 500 nm long pass filters and is collected by a 200 μm diameter fiber connected to a Hammamatsu photosensor module (PMT, H7422P-40). A Stanford Research SR830 lock-in amplifier with current gain of 106 A/V then measures the magnitude of the PMT current signal at the laser reference chopping frequency.

- **UV-Absortion and Photoluminiscence measurements**

  The UV-vis absorption spectrum was taken at room temperature on a UV-vis spectrophotometer (Cary 100 from Varian Inc.) between 300 and 800 nm. The stationary PL and transient spectrum was taken in a Cary 100 eclipse with excitation wavelength of 300 and 500 nm. To take the transient spectrum, first we found the emission peak and subsequently took the data at this point.

- **Current Voltage, and External quantum efficiency measurements**

  Electrical characterization of the devices was performed using a 4200SCS Keithley system at a voltage sweep speed of around 400 mV/s in combination with an Oriel sol3A sun simulator, which was calibrated to AM1.5G standard conditions using an Oriel 91150 V reference cell. The J-V curves were recorded from forward bias (FB) to the short-circuit (SC) condition and vice versa. Devices were masked with a metal aperture of 9 mm^2 to define the active area. No device preconditioning was applied before starting the measurement. An Oriel IQE 200 was used to determine the external quantum efficiency

- **X-Ray diffraction measurements**

  X-ray diffractogram was collected from the obtained powders in a PANalytical diffractometer. The samples were scanned from 2θ= 10° to 60° in a Bragg-Brentano geometry, using Cu-K (1.5408 Å) radiation with a step size of 0.04° and a speed of $5^{\circ}\cdot$ min^{-1}

Appendix B

AFM techniques

In this chapter will be illustrated in detail the fundamentals of the KPFM, SPV and IMKPFM, that was used as the meaning tool to understand the different properties analyzed in this work

B.1 Atomic Force Microscopy (AFM) and Kelvin Probe Force microscopy (KPFM)

A force microscope detects forces (attractive o repulsive forces) acting between a sample surface and a sharp tip which is mounted on a soft leaf spring called cantilever (see Figure). feedback system which controls the vertical z-position of the tip on the sample surface keeps the deflection of the cantilever (and thus the force between the tip and sample) constant. Moving the tip relative to the sample in the (x,y) plane of the surface by means of piezoelectric drives, the actual z-position of the tip can be recorded as a function of the lateral (x, y) position. The obtained three-dimensional data represent a map of equal forces [141].

With the concept described above, it is possible to detect any kind of force as long as the tip is sensitive enough to the interaction, that is, the interaction causes a measurable deflection of the cantilever on which the tip is mounted. Therefore, not only interatomic forces but also long-range forces such as magnetic or electrostatic forces can be detected and mapped. Particularly in the case of detecting the difference of work function of the tip ϕ_{tip} and samples ϕ_{sample}, the kelvin Probe Force Microscopy (KPFM) has been developed. As is described below.

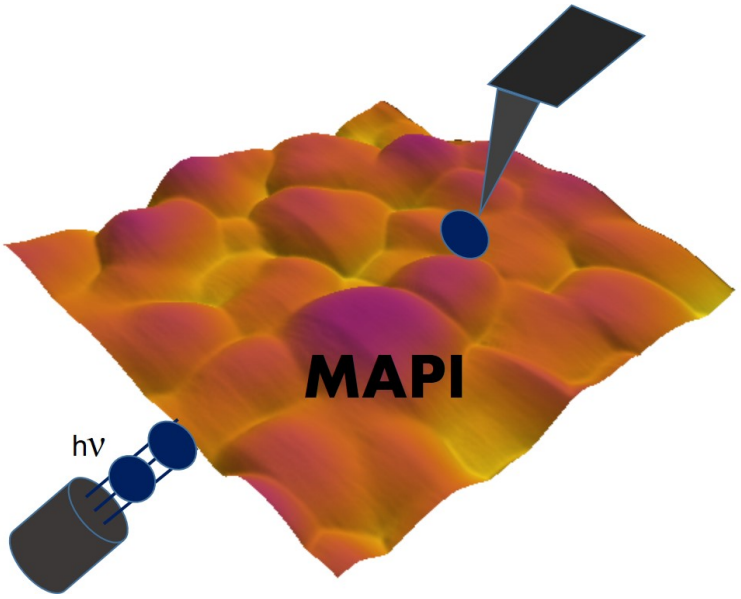

FIGURE B.1: Sketch of a tip scanning a Real 3d MAPI image while is illuminated by a led or laser source

Due to the capacitance between the tip and the sample is produced a net force is in the region near to the contact of the two materials, in the equation below is shown the terms that make part of this force

$$F = -\frac{1}{2}\frac{\partial C}{\partial z}[V_{dc} + V_{CPD} + V_{ac}\sin(\omega_{ac}t)]^2 \tag{B.1}$$

where

$$V_{CPD} = \frac{\phi_{sample} - \phi_{tip}}{e} \tag{B.2}$$

the equation can be written as the addition of different components

$$F_{DC} = -\frac{\partial C}{\partial z}[\frac{1}{2}(V_{dc} - V_{CPD})^2 + \frac{(V_{ac})^2}{4}] \tag{B.3}$$

$$F_{\omega} = -\frac{\partial C}{\partial z}[\frac{1}{2}(V_{dc} - V_{CPD})V_{ac}\sin(\omega_{ac}t)] \tag{B.4}$$

$$F_{2\omega} = \frac{\partial C}{\partial z}\frac{V_{ac}^2}{4}\sin 2(\omega_{ac}t) \tag{B.5}$$

The first one F_{DC} is the contribution to the topography, F_{ω} gives information about the V_{cpd} and $F_{2\omega}$ is used for capacitance microscopy.

[142]

There are two ways of take the measurements of the V_{cpd}, AM-KPFM and FM-KPFM, because in this work we used the first one, we will describe the mechanism of working in that way.

Basically in AM mode, is detected the change in the amplitude of cantilever oscillation at some frequency ω_{ac} of the ac force, Recording Vdc while scanning the topography, an image of the CPD is obtained. Many KPFM systems use this technique with ac-frequencies of several kHz to several tens of kHz.

In our case we use a two steps mode. In the first pass the scan line topography is recorded, and to the second pass the tip is lifted up a a small distance (delta high - around tens of nm)relative from the first pass. Then a ac-voltage atωr is applied with a amplitude necessary to minimize the force as was describe in the equations, detecting in this way the V_{cpd}. So the KPFM use a system to compensate the electrostatic force between the AFM-tip and sample, using a dc-bias which should match with the V_{cpd}. As this signal is very small a lock-in amplifier is necessary.

B.2 Surface Photovoltage (SPV)

Due to a incident illumination in a some sample or device (Metal-semiconductor or insulator) is produced the photovoltaic. Usually the result is some charge transfer and/or redistribution within the device. A specific variant of the photovoltaic effect is the surface photovoltaic effect [143]. The surface photovoltage (SPV) is defined as the illumination-induced change in the V_{cpd}. This effect, observed at at first in Si and Ge surfaces, was reported in a short note by Brattain, and later used in many materials including inorganic organic and perovskites [144–147].

We concentrate on the SPV induced at the free surface of a semiconductor sample with a grounded Ohmic back contact. In many SPV theories it is (explicitly or implicitly) assumed that no appreciable voltage drop develops on the quasi-neutral bulk even under illumination, as depicted schematically in for the case of depletion. In the absence of an external field, the charge neutrality rule, must remain valid regardless of illumination but the absorbed photons induce the formation of free carriers by creating electronâhole pairs via band-to-band transitions (typically dominant for super-bandgap photons (photons with energy over band gap energy)) and/or release captured carriers via trap-to-band transitions (typically dominant for sub-bandgap photons). Thus, a significant amount of charge may be transferred from the surface to the bulk (or vice versa) and/or re-distributed within the surface or the bulk [143]. Since the electric potential and the

charge distribution are inter-dependent through the Poisson and continuity equations, the potential drop across the surface space charge region SCR (although in the neutral region can still produce a potential drop), and hence the surface potential,changes. It is important to note that the formation of a SPV occurs only if carrier generation per se is followed by net charge redistribution. The detailed analysis of the SPV depends strongly on whether the incident photon energy is super-bandgap or sub-bandgap [143].

B.3 Intensity Modulated Kelvin Probe Force Microscopy (IMKPFM)

One method of measuring local recombination is intensity modulated scanning Kelvin probe microscopy (IM-SKPM), which can measure carrier lifetimes with resolution below the optical diffraction limit. IM-KPM is a frequency-domain measurement that uses the slow response of a standard SKPM feedback loop to measure the time averaged contact potential difference V_{CPD} between the tip and sample in response to a modulated illumination source Figure B.1. As the experimental modulation frequency increases, the average V_{CPD} will also increase because recombination is too slow to decay completely during a single cycle the rate at which average V_{CPD} evolves as a function of modulation frequency thus reflects the carrier lifetime in the film [148].

Appendix C

Photovoltaic Characteristics of Solar Cells

The solar cells can be defined as a battery which works while a illumination source is acting on it. The typical shape of the IV-curve of a solar cells under external pole in dark conditions is the curve of a diode which shows the rectification properties of the cell, and under illumination conditions a photovoltage and photocurrent is acquired. The intersection with the current edge gives the short circuit current (Jsc) and the intersection with the voltage edge gives the open circuit voltage(V). As their names indicate the Jsc gives the current without any load connected to the cell, and the Voc gives the voltage with a infinite load connected. A difference of a traditional electrochemist battery their current and voltage characteristics are almost independent of the load, but its current density is dependent of the light intensity (photocurrent). In order to see the dependence of the current density with the incident spectrum is needed the concept of quantum efficiency QE which is the probability that an incident photon of energy E will deliver one electron to the external circuit([1])

$$J_{sc} = q \int b_s QE(E) dE \tag{C.1}$$

here b_s is the photon flux density and represent the number of photons of energy in the range E to E+ dE. In other way the QE(E) depends on the absorption coefficient of the absorber material, the efficiency in the charge separation and collection but is independent of the solar spectrum.

In a common way the solar cells behave like a diode, if a load is present a potential difference is created between the electrodes of the cell. This voltage or an applied external pole produce a current which acts in the opossite direction to the fotocurrent. So taking the same model of an ideal diode the dark density current $J_{dark}(V)$ is

$$J_{dark}(V) = J_0(e^{\frac{qV}{KT}} - 1) \tag{C.2}$$

Where K is the boltzmann constant, T the is the temperature, and J_0 is a constant. If we take the sum of the of the dark current and the short circuit photocurrent in a linear response we get the current-voltage characteristic, this is called the superposition approximation that is expressed in the next equation.

$$J(V) = J_{sc} + J_{dark}(V) \tag{C.3}$$

If there is not connection(open circuit), the potential difference has a maximum value V_{oc}, In this point the dark and short circuit current cancel out and we get a relationship between the J_{sc} and the V_{oc}

$$V_{oc} = \frac{KT}{q} \ln \frac{J_{sc}}{J_0} + 1 \tag{C.4}$$

With this concepts in mind the efficiency of a solar could be defined, because the cell delivers power in a range of 0 to V_{oc}. So the power is

$$P = JV \tag{C.5}$$

This power reaches a maximum power point in some place in the range before mentioned this point has maximum voltage V_m and a maximum density current J_m. So if the light power density is P_s the efficiency η of a solar cell is defined as

$$\eta = \frac{J_m V_m}{P_s} \tag{C.6}$$

If it is defined the fill factor FF as

$$\eta = \frac{J_m V_m}{J_{sc} V_{oc}} \tag{C.7}$$

This fill factor describe how good diode is the cell or its squareness. Then the efficiency can be expressed in the following way

$$\eta = \frac{J_{sc} V_{oc} FF}{P_s} = PCE \tag{C.8}$$

In this expression are key parameters that characterized a solar cell, but they should be defined under some particular illumination condition. As a standard test condition a Air Mass 1.5 spectrum, and incident density power of 1000W m^{-2} and a temperature of 25 °C is taken. Almost all the physics characteristics of a solar cell are reflected in on of these four parameters, so any change in the fabrications conditions and materials will change the J-V curve.

Moreover to take in count a complete description of the cell in a diode way model a parasitic resistances could be included in order to include the effect of the contacts and interfaces. This parasitic resistances are the series resistance R_s and the the parallel or shunt resistance R_{sh}, the series resistance arise when the the contacts have a high resistance or some of the buffer layer in the cell has not enough conductivity, in other way the shunt resistance decrease when there is a leakage current as a product around the edges or there exist not good rectification in any of the layers in the cell. Taking in count this two parameters the relationship between the density current and voltage present the next form

$$J(V) = J_{sc} - J_0(e^{q(V+JAR_s)/KT} - 1) - \frac{V + JAR_S}{R_{sh}} \tag{C.9}$$

$$J(V) = J_{sc} - J_0(e^{q(V)/mKT} - 1)$$

where m is ideality factor.

Bibliography

[1] Jenny Nelson. *PHYSICS OF SOLAR CELLS*. 2004. ISBN 1860943403.

[2] Martin A. Green, Yoshihiro Hishikawa, Wilhelm Warta, Ewan D. Dunlop, Dean H. Levi, Jochen Hohl-Ebinger, and Anita W.H. Ho-Baillie. Solar cell efficiency tables (version 50). *Progress in Photovoltaics: Research and Applications*, 25(7):668–676, jul 2017. ISSN 10627995. doi: 10.1002/pip.2909. URL http://doi.wiley.com/10.1002/pip.2909.

[3] Yoshihiro Hamakawa. *Thin-Film Solar Cells: Next Generation Photovoltaics and Its Applications*. Number 1. Springer, Berlin, 2003. ISBN 9780874216561. doi: 10.1007/s13398-014-0173-7.2.

[4] Junfeng Yan and Brian R. Saunders. Third-generation solar cells: a review and comparison of polymer:fullerene, hybrid polymer and perovskite solar cells. *RSC Adv.*, 4(82):43286–43314, sep 2014. ISSN 2046-2069. doi: 10.1039/C4RA07064J. URL http://xlink.rsc.org/?DOI=C4RA07064J.

[5] Woon Seok Yang, Byung-wook Park, Eui Hyuk Jung, and Nam Joong Jeon. Iodide management in formamidinium-lead-halide- based perovskite layers for efficient solar cells. *Science*, 356:1376–1379, 2017.

[6] J P Correa-Baena, M Saliba, T Buonassisi, M Gratzel, A Abate, W Tress, and A Hagfeldt. Promises and challenges of perovskite solar cells. *Science*, 358(6364): 739–744, 2017. doi: 10.1126/science.aam6323. URL https://www.ncbi.nlm.nih.gov/pubmed/29123060.

[7] Juan-Pablo Correa-Baena, Antonio Abate, Michael Saliba, Wolfgang Tress, T. Jesper Jacobsson, Michael Grätzel, and Anders Hagfeldt. The rapid evolution of highly efficient perovskite solar cells. *Energy & Environmental Science*, 10(3): 710–727, mar 2017. ISSN 1754-5692. doi: 10.1039/C6EE03397K. URL http://xlink.rsc.org/?DOI=C6EE03397K.

[8] Henry J Snaith. Perovskites: The Emergence of a New Era for Low-Cost , High-. *J. Phys. Chem. Lett*, 4:3623–3630, 2013. ISSN 1948-7185. doi: 10.1021/jz4020162.

[9] Martin a. Green, Anita Ho-Baillie, and Henry J. Snaith. The emergence of perovskite solar cells. *Nature Photonics*, 8(7):506–514, 2014. ISSN 1749-4885. doi: 10.1038/nphoton.2014.134. URL http://www.nature.com/doifinder/10.1038/nphoton.2014.134.

[10] Martin a. Green and Thomas Bein. Photovoltaics: Perovskite cells charge forward. *Nature Materials*, 14(6):559–561, 2015. ISSN 1476-1122. doi: 10.1038/nmat4301. URL http://www.nature.com/doifinder/10.1038/nmat4301.

[11] Víctor Luaña, Aurora Costales, and A Martín Pendás. Ions in crystals: The topology of the electron density in ionic materials.II. The cubic alkali halide perovskites. *Physical Review B*, 55(7):4285–4297, feb 1997.

[12] Kai Zhu, Tsutomu Miyasaka, Jin Young Kim, and Iván Mora-Seró. Trend of Perovskite Solar Cells: Dig Deeper to Build Higher. *The Journal of Physical Chemistry Letters*, 6(12):2315–2317, 2015. ISSN 1948-7185. doi: 10.1021/acs.jpclett.5b01033. URL http://pubs.acs.org/doi/abs/10.1021/acs.jpclett.5b01033.

[13] Hui-Seon Kim, Sang Hyuk Im, and Nam-Gyu Park. Organolead Halide Perovskite: New Horizons in Solar Cell Research. *The Journal of Physical Chemistry C*, 118(11):5615–5625, 2014. ISSN 1932-7447. doi: 10.1021/jp409025w. URL http://www.scopus.com/inward/record.url?eid=2-s2.0-84897879784{&}partnerID=tZOtx3y1.

[14] T. Jesper Jacobsson, Meysam Pazoki, Anders Hagfeldt, and Tomas Edvinsson. Goldschmidt's Rules and Strontium Replacement in Lead Halogen Perovskite Solar Cells: Theory and Preliminary Experiments on CH3NH3 SrI3. *The Journal of Physical Chemistry C*, page acs.jpcc.5b06436, 2015. ISSN 1932-7447. doi: 10.1021/acs.jpcc.5b06436. URL http://pubs.acs.org/doi/10.1021/acs.jpcc.5b06436.

[15] Feng Hao, Constantinos C. Stoumpos, Duyen Hanh Cao, Robert P. H. Chang, and Mercouri G. Kanatzidis. Lead-free solid-state organicâinorganic halide perovskite solar cells. *Nature Photonics*, 8(6):489–494, 2014. ISSN 1749-4885. doi: 10.1038/nphoton.2014.82. URL http://dx.doi.org/10.1038/nphoton.2014.82{%}5Cnhttp://www.nature.com/doifinder/10.1038/nphoton.2014.82.

[16] Nakita K Noel, Samuel D Stranks, Antonio Abate, Christian Wehrenfennig, Simone Guarnera, Amir-Abbas Haghighirad, Aditya Sadhanala, Giles E Eperon, Sandeep K Pathak, Michael B Johnston, Annamaria Petrozza, Laura M Herz, and Henry J Snaith. Lead-free organic-inorganic tin halide perovskites for photovoltaic applications. *Energy Environ. Sci.*, 7(9):3061–3068, 2014. doi: 10.1039/C4EE01076K. URL http://dx.doi.org/10.1039/C4EE01076K.

[17] Jose Ignacio Uribe, Daniel Ramirez, Jorge Mario Osorio-guille, Jaime Osorio, and Franklin Jaramillo. CH3NH3CaI3 Perovskite: Synthesis, Characterization, and First- Principles Studies. *Journal of Physical Chemistry C*, 120:16393â16398, 2016. doi: 10.1021/acs.jpcc.6b04207.

[18] Giles E. Eperon, Samuel D. Stranks, Christopher Menelaou, Michael B. Johnston, Laura M. Herz, and Henry J. Snaith. Formamidinium lead trihalide: a broadly tunable perovskite for efficient planar heterojunction solar cells. *Energy & Environmental Science*, 7(3):982, feb 2014. ISSN 1754-5692. doi: 10.1039/c3ee43822h. URL http://xlink.rsc.org/?DOI=c3ee43822h.

[19] Xiaofei Zhao, Baohua Zhang, Ruyan Zhao, Bing Yao, Xuejing Liu, Jun Liu, and Zhiyuan Xie. Simple and Efficient Green-Light-Emitting Diodes Based on Thin Organolead Bromide Perovskite Films via Tuning Precursor Ratios and Postannealing Temperature. *Journal of Physical Chemistry Letters*, 7(21): 4259–4266, 2016. doi: 10.1021/acs.jpclett.6b02160.

[20] Chog Barugkin, Jinjin Cong, The Duong, Shakir Rahman, Hieu T. Nguyen, Daniel Macdonald, Thomas P. White, and Kylie R. Catchpole. Ultralow Absorption Coefficient and Temperature Dependence of Radiative Recombination of CH3NH PbI3 Perovskite from Photoluminescence. *The Journal of Physical Chemistry Letters*, 6:767–772, 2015. ISSN 1948-7185. doi: 10.1021/acs.jpclett.5b00044.

[21] Ivano E. Castelli, Kristian S. Thygesen, and Karsten W. Jacobsen. Calculated optical absorption of different perovskite phases. *J. Mater. Chem. A*, 3(23): 12343–12349, 2015. ISSN 2050-7488. doi: 10.1039/C5TA01586C.

[22] Atsuhiko Miyata, Anatolie Mitioglu, Paulina Plochocka, Oliver Portugall, Jacob Tse-wei Wang, Samuel D Stranks, Henry J Snaith, and Robin J Nicholas. Direct measurement of the exciton binding energy and effective masses for charge carriers in organic-inorganic tri-halide perovskites. *Nature Physics*, 11(7): 582–587, 2015. ISSN 1745-2473. doi: 10.1038/nphys3357.

[23] G. Xing, N. Mathews, S. Sun, S. S. Lim, Y. M. Lam, M. Gratzel, S. Mhaisalkar, and T. C. Sum. Long-Range Balanced Electron- and Hole-Transport Lengths in

Organic-Inorganic CH3NH3PbI3. *Science*, 342(6156):344–347, 2013. ISSN 0036-8075. doi: 10.1126/science.1243167.

[24] Samuel D Stranks, Giles E Eperon, Giulia Grancini, Christopher Menelaou, Marcelo J P Alcocer, Tomas Leijtens, Laura M Herz, Annamaria Petrozza, and Henry J Snaith. Electron-hole diffusion lengths exceeding 1 micrometer in an organometal trihalide perovskite absorber. *Science (New York, N.Y.)*, 342(6156): 341–4, oct 2013. ISSN 1095-9203. doi: 10.1126/science.1243982.

[25] Tomas Leijtens, Samuel D Stranks, Giles E Eperon, Rebecka Lindblad, Erik M J Johansson, James M Ball, Michael M Lee, Henry J Snaith, and Ian J Mcpherson. Electronic Properties of Meso-Superstructured and Planar Organometal Halide Perovskite Films : Charge Trapping, Photodoing, and Carrier Mobility. *ACS nano*, (7):7147–7155, 2014. ISSN 1936086X. doi: 10.1021/nn502115k.

[26] Wenchao Yang, Yao Yao, and Chang-Qin Wu. Origin of the high open circuit voltage in planar heterojunction perovskite solar cells: Role of the reduced bimolecular recombination. *Journal of Applied Physics*, 117(9):095502, mar 2015. ISSN 0021-8979. doi: 10.1063/1.4913519. URL http://aip.scitation.org/doi/10.1063/1.4913519.

[27] Huanping Zhou, Qi Chen, Gang Li, Song Luo, Tze-bing Song, Hsin-Sheng Duan, Ziruo Hong, Jingbi You, Yongsheng Liu, and Yang Yang. Interface engineering of highly efficient perovskite solar cells. *Science*, 345(6196):542–547, 2014. doi: 10.1126/science.1254050.

[28] Michael M Lee, Joël Teuscher, Tsutomu Miyasaka, Takurou N Murakami, and Henry J Snaith. Efficient hybrid solar cells based on meso-superstructured organometal halide perovskites. *Science (New York, N.Y.)*, 338(6107):643–7, nov 2012. ISSN 1095-9203. doi: 10.1126/science.1228604. URL http://www.ncbi.nlm.nih.gov/pubmed/23042296.

[29] Daniel Ramirez, Mario Alejandro Mejía Escobar, Juan F. Montoya, and Franklin Jaramillo. Understanding the Role of the Mesoporous Layer in the Thermal Crystallization of a Meso-Superstructured Perovskite Solar Cell. *Journal of Physical Chemistry C*, 120(16):8559–8567, 2016. ISSN 19327455. doi: 10.1021/acs.jpcc.6b02808.

[30] Chuantian Zuo, Henk J. Bolink, Hongwei Han, Jinsong Huang, David Cahen, and Liming Ding. Advances in Perovskite Solar Cells. *Advanced Science*, 3(7): 1500324, jul 2016. ISSN 21983844. doi: 10.1002/advs.201500324. URL http://doi.wiley.com/10.1002/advs.201500324.

[31] Hyun Suk Jung and Nam Gyu Park. Perovskite solar cells: From materials to devices. *Small*, 11(1):10–25, 2015. ISSN 16136829. doi: 10.1002/smll.201402767.

[32] Wei E. I. Sha, Xingang Ren, Luzhou Chen, and Wallace C. H. Choy. The efficiency limit of CH3NH3PbI3 perovskite solar cells. *Applied Physics Letters*, 106(22):221104, 2015. ISSN 0003-6951. doi: 10.1063/1.4922150. URL http://scitation.aip.org/content/aip/journal/apl/106/22/10.1063/1.4922150.

[33] Luis Katsuya Ono and Yabing. Qi. Surface and Interface Aspects of Organometal Halide Perovskite Materials and Solar Cells. *Journal of Physical Chemistry Letters*, 22:4764–4794, 2016. ISSN 1948-7185. doi: 10.1021/acs.jpclett.6b01951.

[34] W Dane, Sarah M Vorpahl, Samuel D Stranks, Hirokazu Nagaoka, Giles E Eperon, Mark E Ziffer, J Henry, and David S Ginger. Impact of microstructure on local carrier lifetime in perovskite solar cells. *Science*, 348(6235):683–686, 2015.

[35] Dane W. DeQuilettes, Wei Zhang, Victor M. Burlakov, Daniel J. Graham, Tomas Leijtens, Anna Osherov, Vladimir Bulović, Henry J. Snaith, David S. Ginger, and Samuel D. Stranks. Photo-induced halide redistribution in organicâinorganic perovskite films. *Nature Communications*, 7(May):11683, 2016. ISSN 2041-1723. doi: 10.1038/ncomms11683. URL http://www.nature.com/doifinder/10.1038/ncomms11683{%}5Cnhttp://arxiv.org/abs/1507.02142{%}5Cnhttp://www.nature.com/doifinder/10.1038/ncomms11683.

[36] Samuel D. Stranks, Victor M. Burlakov, Tomas Leijtens, James M. Ball, Alain Goriely, and Henry J. Snaith. Recombination Kinetics in Organic-Inorganic Perovskites: Excitons, Free Charge, and Subgap States. *Physical Review Applied*, 2(3):1–8, 2014. ISSN 23317019. doi: 10.1103/PhysRevApplied.2.034007.

[37] Rafael Betancur, Daniel Ramirez, Juan F. Montoya, and Franklin Jaramillo. A calorimetric approach to reach high performance perovskite solar cells. *Solar Energy Materials and Solar Cells*, 146:44–50, 2016. ISSN 09270248. doi: 10.1016/j.solmat.2015.10.024. URL http://dx.doi.org/10.1016/j.solmat.2015.10.024.

[38] Jeong-Hyeok Im, In-Hyuk Jang, Norman Pellet, Michael Grätzel, and Nam-Gyu Park. Growth of CH3NH3PbI3 cuboids with controlled size for high-efficiency perovskite solar cells. *Nature nanotechnology*, 9(11):927–932, 2014. ISSN 1748-3395. doi: 10.1038/nnano.2014.181.

[39] Senyun Ye, Weihai Sun, Yunlong Li, Weibo Yan, Haitao Peng, Zuqiang Bian, Zhiwei Liu, and Chunhui Huang. CuSCN-based inverted planar perovskite solar cell with an average PCE of 15.6%. *Nano Letters*, page 150504172654007, 2015. ISSN 1530-6984. doi: 10.1021/acs.nanolett.5b00116. URL http://dx.doi.org/10.1021/acs.nanolett.5b00116.

[40] Chuantian Zuo and Liming Ding. Solution-Processed Cu2O and CuO as Hole Transport Materials for Efficient Perovskite Solar Cells. *Small*, 11(41):5528–5532, 2015. ISSN 16136829. doi: 10.1002/smll.201501330.

[41] Jong H. Kim, Po Wei Liang, Spencer T. Williams, Namchul Cho, Chu Chen Chueh, Micah S. Glaz, David S. Ginger, and Alex K Y Jen. High-performance and environmentally stable planar heterojunction perovskite solar cells based on a solution-processed copper-doped nickel oxide hole-transporting layer. *Advanced Materials*, 27(4):695–701, 2015. ISSN 15214095. doi: 10.1002/adma.201404189.

[42] Minzan Huangfu, Yue Shen, Gongbo Zhu, Kai Xu, Meng Cao, Feng Gu, and Linjun Wang. Copper iodide as inorganic hole conductor for perovskite solar cells with different thickness of mesoporous layer and hole transport layer. *Applied Surface Science*, 357:2234–2240, 2015. ISSN 01694332. doi: 10.1016/j.apsusc.2015.09.215. URL http://dx.doi.org/10.1016/j.apsusc.2015.09.215.

[43] Hirokazu Nagaoka, Fei Ma, Dane W. Dequilettes, Sarah M. Vorpahl, Micah S. Glaz, Adam E. Colbert, Mark E. Ziffer, and David S. Ginger. Zr incorporation into TiO2 electrodes reduces hysteresis and improves performance in hybrid perovskite solar cells while increasing carrier lifetimes. *Journal of Physical Chemistry Letters*, 6(4):669–675, 2015. ISSN 19487185. doi: 10.1021/jz502694g.

[44] Mario Alejandro Mejía Escobar, Sandeep Pathak, Jiewei Liu, Henry J. Snaith, and Franklin Jaramillo. ZrO2/TiO2 electron collection layer for efficient meso-superstructured hybrid perovskite solar cells. *ACS Applied Materials & Interfaces*, page acsami.6b12509, 2016. ISSN 1944-8244. doi: 10.1021/acsami.6b12509. URL http://pubs.acs.org/doi/abs/10.1021/acsami.6b12509.

[45] Ashok Bera, Kewei Wu, Arif Sheikh, Erkki Alarousu, Omar F. Mohammed, and Tom Wu. Perovskite Oxide SrTiO3 as an Efficient Electron Transporter for Hybrid Perovskite Solar Cells. *The Journal of Physical Chemistry C*, 118(49): 28494–28501, 2014. ISSN 1932-7447. doi: 10.1021/jp509753p. URL http://dx.doi.org/10.1021/jp509753p.

[46] E Edri, S Kirmayer, A Henning, S Mukhopadhyay, K Gartsman, Y Rosenwaks, G Hodes, and D Cahen. Why Lead Methylammonium Tri-Iodide Perovskite-Based Solar Cells Require a Mesoporous Electron Transporting Scaffold (but Not Necessarily a Hole Conductor). *Nano Letters*, 14(2):1000–1004, 2014. doi: 10.1021/nl404454h.

[47] James M. Ball, Michael M. Lee, Andrew Hey, and Henry J. Snaith. Low-temperature processed meso-superstructured to thin-film perovskite solar cells. *Energy & Environmental Science*, 6(6):1739, 2013. ISSN 1754-5692. doi: 10.1039/c3ee40810h. URL http://xlink.rsc.org/?DOI=c3ee40810h.

[48] M. M. Lee, J Teuscher, T. Miyasaka, T. N. Murakami, and H. J. Snaith. Efficient Hybrid Solar Cells Based on Meso-Superstructured Organometal Halide Perovskites. *Science*, 338(6107):643–647, nov 2012. ISSN 0036-8075. doi: 10.1126/science.1228604. URL http://www.sciencemag.org/cgi/doi/10.1126/science.1228604.

[49] Sibel Y. Leblebici, Linn Leppert, Yanbo Li, Sebastian E. Reyes-Lillo, Sebastian Wickenburg, Ed Wong, Jiye Lee, Mauro Melli, Dominik Ziegler, Daniel K. Angell, D. Frank Ogletree, Paul D. Ashby, Francesca M. Toma, Jeffrey B. Neaton, Ian D. Sharp, and Alexander Weber-Bargioni. Facet-dependent photovoltaic efficiency variations in single grains of hybrid halide perovskite. *Nature Energy*, 1(8):16093, 2016. ISSN 2058-7546. doi: 10.1038/nenergy.2016.93. URL http://www.nature.com/articles/nenergy201693.

[50] Hossain Mohhamad, Fahhad H.Alharbi, and NouarTabet. Copper oxide as inorganic hole transport material for lead halide perovskite based solar cells. *Solar Energy*, 120:370–380, oct 2015. ISSN 0038-092X. doi: 10.1016/J.SOLENER.2015.07.040. URL http://www.sciencedirect.com/science/article/pii/S0038092X15004119.

[51] Soumyo Chatterjee and Amlan J. Pal. Introducing Cu2O Thin Films as a Hole-Transport Layer in Efficient Planar Perovskite Solar Cell Structures. *The Journal of Physical Chemistry C*, 120(3):1428–1437, jan 2016. ISSN 1932-7447. doi: 10.1021/acs.jpcc.5b11540. URL http://pubs.acs.org/doi/abs/10.1021/acs.jpcc.5b11540.

[52] Bahram Abdollahi Nejand, Vahid Ahmadi, Saba Gharibzadeh, and Hamid Reza Shahverdi. Cuprous Oxide as a Potential Low-Cost Hole-Transport Material for Stable Perovskite Solar Cells. *ChemSusChem*, 9(3):302–313, feb 2016. ISSN 18645631. doi: 10.1002/cssc.201501273. URL http://doi.wiley.com/10.1002/cssc.201501273.

[53] Tsuyoshi Kosugi and Shoji Kaneko. Novel Spray-Pyrolysis Deposition of Cuprous Oxide Thin Films. *Journal of the American Ceramic Society*, 81(12): 3117–3124, dec 1998. ISSN 0002-7820. doi: 10.1111/j.1151-2916.1998.tb02746.x. URL http://doi.wiley.com/10.1111/j.1151-2916.1998.tb02746.x.

[54] J. Ciro, R. Betancur, S. Mesa, and F. Jaramillo. High performance perovskite solar cells fabricated under high humidity and sub 100°C processing conditions. *Solar Energy Materials & Solar Cells*, 163:38–42, 2017. ISSN 09270248. doi: 10.1016/j.solmat.2017.01.004.

[55] Bai Gongjian, Weng Yunxuan, and Hu Xingzhou. Surface modification of polyolefine by UV light/ozone treatment. *Journal of Applied Polymer Science*, 60 (13):2397–2402, jun 1996. ISSN 0021-8995. doi: 10.1002/(SICI)1097-4628(19960627)60:13⟨2397::AID-APP11⟩3.0.CO;2-2. URL http://doi.wiley.com/10.1002/{%}28SICI{%}291097-4628{%}2819960627{%}2960{%}3A13{%}3C2397{%}3A{%}3AAID-APP11{%}0.CO{%}3B2-2.

[56] D. O. H. Teare, C. Ton-That, and R. H. Bradley. Surface characterization and ageing of ultraviolet-ozone-treated polymers using atomic force microscopy and x-ray photoelectron spectroscopy. *Surface and Interface Analysis*, 29(4):276–283, apr 2000. ISSN 0142-2421. doi: 10.1002/(SICI)1096-9918(200004)29:4⟨276::AID-SIA740⟩3.0.CO;2-P. URL http://doi.wiley.com/10.1002/{%}28SICI{%}291096-9918{%}28200004{%}2929{%}3A4{%}3C276{%}3A{%}3AAID-SIA740{%}3E0.CO{%}3B2-P.

[57] Weijun Ke, Guojia Fang, Jiawei Wan, Hong Tao, Qin Liu, Liangbin Xiong, Pingli Qin, Jing Wang, Hongwei Lei, Guang Yang, Minchao Qin, Xingzhong Zhao, and Yanfa Yan. Efficient hole-blocking layer-free planar halide perovskite thin-film solar cells. *Nature Communications*, 6(1):6700, dec 2015. ISSN 2041-1723. doi: 10.1038/ncomms7700. URL http://www.nature.com/articles/ncomms7700.

[58] John Ciro, Rafael Betancur, Santiago Mesa, and Franklin Jaramillo. High performance perovskite solar cells fabricated under high relative humidity conditions. *Solar Energy Materials and Solar Cells*, 163:38–42, apr 2017. ISSN 09270248. doi: 10.1016/j.solmat.2017.01.004. URL http://linkinghub.elsevier.com/retrieve/pii/S0927024817300041.

[59] Jingbi You, Lei Meng, Tze-Bin Song, Tzung-Fang Guo, Yang (Michael) Yang, Wei-Hsuan Chang, Ziruo Hong, Huajun Chen, Huanping Zhou, Qi Chen, Yongsheng Liu, Nicholas De Marco, and Yang Yang. Improved air stability of

perovskite solar cells via solution-processed metal oxide transport layers. *Nature Nanotechnology*, 11(October):1–8, 2015. ISSN 1748-3387. doi: 10.1038/nnano.2015.230. URL http://www.nature.com/doifinder/10.1038/nnano.2015.230.

[60] Giles E. Eperon and David S. Ginger. Perovskite solar cells: Different facets of performance. *Nature Energy*, 1(8):16109, jul 2016. ISSN 2058-7546. doi: 10.1038/nenergy.2016.109. URL http://www.nature.com/articles/nenergy2016109.

[61] Wei Zhang, Sandeep Pathak, Nobuya Sakai, Thomas Stergiopoulos, Pabitra K. Nayak, Nakita K. Noel, Amir A. Haghighirad, Victor M. Burlakov, Dane W. DeQuilettes, Aditya Sadhanala, Wenzhe Li, Liduo Wang, David S. Ginger, Richard H. Friend, and Henry J. Snaith. Enhanced optoelectronic quality of perovskite thin films with hypophosphorous acid for planar heterojunction solar cells. *Nature Communications*, 6(May):10030, 2015. ISSN 2041-1723. doi: 10.1038/ncomms10030. URL http://www.nature.com/doifinder/10.1038/ncomms10030.

[62] David Moerman, Hyungchul Kim, Adam E. Colbert, Samuel Graham, and David S. Ginger. The impact of ultra-thin titania interlayers on open circuit voltage and carrier lifetime in thin film solar cells. *Applied Physics Letters*, 108 (11), 2016. ISSN 00036951. doi: 10.1063/1.4944049.

[63] Guozheng Shao, Micah S Glaz, Fei Ma, Huanxin Ju, and David S Ginger. Intensity-Modulated Scanning Kelvin Probe Microscopy Intensity-Modulated Scanning Kelvin Probe Microscopy for Probing Recombination in Organic Photovoltaics. (10):10799–10807, 2014. doi: 10.1021/nn5045867.

[64] Masaki Takihara, Takuji Takahashi, and Toru Ujihara. Minority carrier lifetime in polycrystalline silicon solar cells studied by photoassisted Kelvin probe force microscopy. *Applied Physics Letters*, 93(2):1–4, 2008. ISSN 00036951. doi: 10.1063/1.2957468.

[65] C. Deibel, A. Baumann, A. Wagenpfahl, and V. Dyakonov. Polaron recombination in pristine and annealed bulk heterojunction solar cells. *Synthetic Metals*, 159(21-22):2345–2347, 2009. ISSN 03796779. doi: 10.1016/j.synthmet.2009.07.014.

[66] W. F. Pasveer, J. Cottaar, C. Tanase, R. Coehoorn, P. A. Bobbert, P. W M Blom, M. De Leeuw, and M. A J Michels. Unified description of charge-carrier mobilities in disordered semiconducting polymers. *Physical Review Letters*, 94 (20):1–4, 2005. ISSN 00319007. doi: 10.1103/PhysRevLett.94.206601.

[67] C. G. Shuttle, B. O'Regan, A. M. Ballantyne, J. Nelson, D. D C Bradley, J. De Mello, and J. R. Durrant. Experimental determination of the rate law for charge carrier decay in a polythiophene: Fullerene solar cell. *Applied Physics Letters*, 92 (9):2006–2009, 2008. ISSN 00036951. doi: 10.1063/1.2891871.

[68] Giles E. Eperon, David Moerman, and David S. Ginger. Anticorrelation between Local Photoluminescence and Photocurrent Suggests Variability in Contact to Active Layer in Perovskite Solar Cells. *ACS Nano*, 10(11):10258–10266, 2016. ISSN 1936086X. doi: 10.1021/acsnano.6b05825.

[69] Christopher Eames, Jarvist M. Frost, Piers R. F. Barnes, Brian C. O'Regan, Aron Walsh, and M. Saiful Islam. Ionic transport in hybrid lead iodide perovskite solar cells. *Nature Communications*, 6(May):7497, 2015. ISSN 2041-1723. doi: 10.1038/ncomms8497. URL http://www.nature.com/ncomms/2015/150624/ncomms8497/full/ncomms8497.html{%}5Cnhttp://www.nature.com/doifinder/10.1038/ncomms8497.

[70] Peimei Da and Gengfeng Zheng. Tailoring interface of lead-halide perovskite solar cells. *Nano Research*, pages 1–27, 2017. ISSN 19980000. doi: 10.1007/s12274-016-1405-2.

[71] R Steim, F R Kogler, and C J Brabec. Interface materials for organic solar cells. *Journal of Materials Chemistry*, 20(13):2499–2512, 2010. ISSN 0959-9428. doi: 10.1039/b921624c.

[72] Gailan A. Al-Dainya, Shawn E. Bourdoa, Viney Saini, Brian C. Berry, and Alexandru S. Biris. Hybrid Perovskite Photovoltaic Devices: Properties, Architecture, and Fabrication Methods. *Energy Technology*, page Accepted manuscript, 2017. doi: 10.1002/ente.201600486.

[73] Y. Yang, M. Yang, D.T Moore, Y. Yan, E.M Miller, K. Zhu, and M.C Beard. Top and bottom surfaces limit carrier lifetime in Lead Iodide Perovskite Films. *Nature Energy*, 2(January):1–7, 2017.

[74] Juan-Pablo Correa-Baena, Wolfgang Tress, Konrad Domanski, Elham Halvani Anaraki, Silver-Hamill Turren-Cruz, Bart Roose, Pablo P. Boix, Michael Grätzel, Michael Saliba, Antonio Abate, and Anders Hagfeldt. Identifying and suppressing interfacial recombination to achieve high open-circuit voltage in perovskite solar cells. *Energy & Environmental Science*, 10(5):1207–1212, may 2017. ISSN 1754-5692. doi: 10.1039/C7EE00421D. URL http://xlink.rsc.org/?DOI=C7EE00421D.

[75] Wanyi Nie, Hsinhan Tsai, Reza Asadpour, Amanda J Neukirch, Gautam Gupta, Jared J Crochet, Manish Chhowalla, Sergei Tretiak, Muhammad A Alam, and Hsing-lin Wang. High-efficiency solution-processed perovskite solar cells with millimeter-scale grains. *Science*, 347(6221):522–526, 2015.

[76] Olga Malinkiewicz, Aswani Yella, Yong Hui Lee, Guillermo Mínguez Espallargas, Michael Graetzel, Mohammad K Nazeeruddin, and Henk J Bolink. Perovskite solar cells employing organic charge-transport layers. 2014. doi: 10.1038/NPHOTON.2013.341. URL https://www.nature.com/nphoton/journal/v8/n2/pdf/nphoton.2013.341.pdf.

[77] Jian Xiong, Bingchu Yang, Runsheng Wu, Chenghao Cao, Yulan Huang, Chengbin Liu, Zhikun Hu, Han Huang, Yongli Gao, and Junliang Yang. Efficient and non-hysteresis CH3NH3PbI3/PCBM planar heterojunction solar cells. *Organic Electronics*, 24(SEPTEMBER):106–112, 2015. ISSN 15661199. doi: 10.1016/j.orgel.2015.05.028.

[78] Yong Zhang, Xiaotian Hu, Lie Chen, Zengqi Huang, Qingxia Fu, Yawen Liu, Lin Zhang, and Yiwang Chen. Flexible , hole transporting layer-free and stable CH3NH3PbI / PC61 BM planar heterojunction perovskite solar cells. *Organic Electronics*, 30:281–288, 2016. ISSN 1566-1199. doi: 10.1016/j.orgel.2016.01.002.

[79] Qiang Guo, Cong Li, Wenyuan Qiao, Shuang Ma, Fuzhi Wang, Bing Zhang, Linhua Hu, Songyuan Dai, and Zhan'ao Tan. The growth of CH3NH3PbI3 thin film by simplified close space sublimation for efficient and large dimensional perovskite solar cells. *Energy Environ. Sci.*, 9:1486–1494, 2016. ISSN 1754-5692. doi: 10.1039/C5EE03620H.

[80] Cong Li, Qiang Guo, Wenyuan Qiao, Qi Chen, Shuang Ma, Xu Pan, Fuzhi Wang, Jianxi Yao, Chunfeng Zhang, Min Xiao, Songyuan Dai, and Zhan'ao Tan. Efficient lead acetate sourced planar heterojunction perovskite solar cells with enhanced substrate coverage via one-step spin-coating. *Organic Electronics*, 33: 194–200, 2016. ISSN 15661199. doi: 10.1016/j.orgel.2016.03.017.

[81] Long Hu, Jun Peng, Weiwei Wang, Zhe Xia, Jianyu Yuan, and Jialing Lu. Sequential deposition of CH3NH3PbI3 on planar NiO film for efficient planar perovskite solar cells Sequential deposition of CH 3 NH 3 PbI 3 on planar NiO film for efficient planar perovskite solar cells. *ACS Photonics*, 1(7):547–553, jun 2014. ISSN 2330-4022.

[82] Hong Zhang, Hamed Azimi, Yi Hou, Tayebeh Ameri, Thomas Przybilla, and Erdmann Spiecker. Improved High-Efficiency Perovskite Planar Heterojunction

Solar Cells via Incorporation of a Polyelectrolyte Interlayer. *Chemistry of Materials*, (26):5190–5193, 2014. ISSN 0897-4756. doi: 10.1021/cm502864s.

[83] Jangwon Seo, Sangman Park, Young Chan Kim, Nam Joong Jeon, Jun Hong Noh, Sung Cheol Yoon, Sang Il Seok, and Perovskite Solar Cells. Benefits of very thin PCBM and LiF layers for solution-processed pâiân perovskite solar cells. *Energy & Environmental Science*, 7(8):2642, 2014. ISSN 1754-5692. doi: 10.1039/C4EE01216J.

[84] Kuan Sun, Baomin Zhao, Vajjiravel Murugesan, Amit Kumar, Kaiyang Zeng, Jegadesan Subbiah, Wallace W. H. Wong, David J. Jones, and Jianyong Ouyang. High-performance polymer solar cells with a conjugated zwitterion by solution processing or thermal deposition as the electron-collection interlayer. *J. Mater. Chem.,*, 22:24155–24165, 2012. doi: 10.1039/C2JM35221D.

[85] Kuan Sun, Jingjing Chang, Furkan Halis Isikgor, Pengcheng Li, and Jianyong Ouyang. Efficiency enhancement of planar perovskite solar cells by adding zwitterion/LiF double interlayers for electron collection. *Nanoscale*, 7(3): 896–900, 2015. ISSN 2040-3364. doi: 10.1039/C4NR05975A.

[86] Qi Wang, Yuchuan Shao, Qingfeng Dong, Zhengguo Xiao, Yongbo Yuan, and Jinsong Huang. Large fill-factor bilayer iodine perovskite solar cells fabricated by a low-temperature solution-process. *Energy & Environmental Science*, 7(7):2359, jun 2014. ISSN 1754-5692. doi: 10.1039/c4ee00233d.

[87] Weiming Qiu, Marie Buffière, Guy Brammertz, Ulrich W. Paetzold, Ludo Froyen, Paul Heremans, and David Cheyns. High efficiency perovskite solar cells using a PCBM/ZnO double electron transport layer and a short air-aging step. *Organic Electronics*, 26:30–35, 2015. ISSN 15661199. doi: 10.1016/j.orgel.2015.06.046.

[88] Nieves Espinosa, Henrik Friis Dam, David M. Tanenbaum, Jens W. Andreasen, Mikkel Jørgensen, and Frederik C. Krebs. Roll-to-Roll Processing of Inverted Polymer Solar Cells using Hydrated Vanadium(V)Oxide as a PEDOT:PSS Replacement. *Materials*, 4(1):169–182, 2011. ISSN 19961944. doi: 10.3390/ma4010169.

[89] Kuan Sun, Pengcheng Li, Yijie Xia, Jingjing Chang, and Jianyong Ouyang. Transparent Conductive Oxide-Free Perovskite Solar Cells with PEDOT:PSS as Transparent Electrode. *ACS Applied Materials and Interfaces*, 7(28): 15314–15320, 2015. ISSN 19448252. doi: 10.1021/acsami.5b03171.

[90] Kuan Sun, Baomin Zhao, Amit Kumar, Kaiyang Zeng, and Jianyong Ouyang. Highly Efficient , Inverted Polymer Solar Cells with Indium Tin Oxide Modified

with Solution-Processed Zwitterions as the Transparent Cathode. *ACS Appl. Mater. Interfaces*, 4:2009, 2012.

[91] Jiang Liu, Gang Wang, Kun Luo, Xulin He, Qinyan Ye, Cheng Liao, and Jun Mei. Understanding the role of electron transport layer in highly efficient planar perovskite solar cells. *ChemPhysChem*, 2017. ISSN 14394235. doi: 10.1002/cphc.201601245.

[92] Cong Li, Fuzhi Wang, Jia Xu, Jianxi Yao, Bing Zhang, Chunfeng Zhang, Min Xiao, Songyuan Dai, Yongfang Li, and Zhan'ao Tan. Efficient perovskite/fullerene planar heterojunction solar cells with enhanced charge extraction and suppressed charge recombination. *Nanoscale*, 7(21):9771–9778, 2015. ISSN 2040-3364. doi: 10.1039/C4NR06240J.

[93] Chen Tao, Jeroen Van Der Velden, Lydia Cabau, Nuria F. Montcada, Stefanie Neutzner, Ajay Ram Srimath Kandada, Sergio Marras, Luigi Brambilla, Matteo Tommasini, Weidong Xu, Roberto Sorrentino, Andrea Perinot, Mario Caironi, Chiara Bertarelli, Emilio Palomares, and Annamaria Petrozza. Fully Solution-Processed n-i-p Like Perovskite Solar Cells with Planar Junction: How the Charge Extracting Layer Determines the Open-Circuit Voltage. *Advanced Materials*, page 1604493, 2017. ISSN 09359648. doi: 10.1002/adma.201604493.

[94] Qi Wang, Qingfeng Dong, Tao Li, Alexei Gruverman, and Jinsong Huang. Thin Insulating Tunneling Contacts for Efficient and Water-Resistant Perovskite Solar Cells. *Advanced Materials*, pages 6734–6739, 2016. ISSN 15214095. doi: 10.1002/adma.201600969.

[95] Severin N Habisreutinger, Tomas Leijtens, Giles E Eperon, Samuel D Stranks, Robin J Nicholas, and Henry J Snaith. Carbon Nanotube/Polymer Composites as a Highly Stable Hole Collection Layer in Perovskite Solar Cells. 2014.

[96] F Ciro, J; Mesa, S; Uribe, J;Mejia, Mario;Ramirez, Daniel; Betancur, R;Yoo, Seok;Park, Nam-Giu;Jaramillo. Optimization of the Ag/PCBM interface by Rhodamine interlayer to enhance efficiency and stability of perovskite solar cells. *Nanoscale*, 9:9440–9446, 2017. doi: 10.1039/C7NR01678F.

[97] S. Sadewasser. Surface potential of chalcopyrite films measured by KPFM. *Physica Status Solidi (A) Applications and Materials Science*, 203(11): 2571–2580, 2006. ISSN 18626300. doi: 10.1002/pssa.200669573.

[98] S. Sadewasser, Th Glatzel, S. Schuler, S. Nishiwaki, R. Kaigawa, and M. Ch Lux-Steiner. Kelvin probe force microscopy for the nano scale characterization of

chalcopyrite solar cell materials and devices. *Thin Solid Films*, 431-432(03): 257–261, 2003. ISSN 00406090. doi: 10.1016/S0040-6090(03)00267-0.

[99] Juan-Pablo Correa-Baena, Antonio Abate, Michael Saliba, Wolfgang Tress, T. Jesper Jacobsson, Michael Grätzel, and Anders Hagfeldt. The rapid evolution of highly efficient perovskite solar cells. *Energy Environ. Sci.*, 2017. ISSN 1754-5692. doi: 10.1039/C6EE03397K.

[100] Yanbo Li, Jason K. Cooper, Wenjun Liu, Carolin M. Sutter-Fella, Matin Amani, Jeffrey W. Beeman, Ali Javey, Joel W. Ager, Yi Liu, Francesca M. Toma, and Ian D. Sharp. Defective TiO2 with high photoconductive gain for efficient and stable planar heterojunction perovskite solar cells. *Nature Communications*, 7: 12446, 2016. ISSN 2041-1723. doi: 10.1038/ncomms12446.

[101] Chen Tao, Stefanie Neutzner, Letizia Colella, Sergio Marras, Ajay Ram, Srimath Kandada, Marina Gandini, Michele De Bastiani, Giuseppina Pace, Liberato Manna, Mario Caironi, Chiara Bertarelli, and Annamaria Petrozza. 17.6% Stabilized Efficiency in Low-Temperature Processed Planar Perovskite Solar Cells. *Energy Environ. Sci. Energy Environ. Sci*, 8(8):2365–2370, 2015. ISSN 1754-5692. doi: 10.1039/c5ee01720c.

[102] Konrad Wojciechowski, Samuel D. Stranks, Antonio Abate, Golnaz Sadoughi, Aditya Sadhanala, Nikos Kopidakis, Garry Rumbles, Chang-Zhi Li, Richard H. Friend, Alex K.-Y. Jen, and Henry J. Snaith. Heterojunction Modification for Highly Efficient Organic?Inorganic Perovskite Solar Cells. *ACS Nano*, 8(12): 12701–12709, dec 2014. ISSN 1936-0851. doi: 10.1021/nn505723h.

[103] Dong Yang, Xin Zhou, Ruixia Yang, Zhou Yang, Wei Yu, Xiuli Wang, Can Li, Shengzhong (Frank) Liu, and Robert P. H. Chang. Surface optimization to eliminate hysteresis for record efficiency planar perovskite solar cells. *Energy and Environmental Science*, 9:3071–3078, 2016. doi: 10.1039/C6EE02139E10.1039/c6ee02139e.

[104] Alba Matas Adams, Jose Manuel Marin-Beloqui, Georgiana Stoica, and Emilio Palomares. The influence of the mesoporous TiO2 scaffold on the performance of methyl ammonium lead iodide (MAPI) perovskite solar cells: charge injection, charge recombination and solar cell efficiency relationship. *J. Mater. Chem. A*, 3: 22154–22161, 2015. ISSN 2050-7488. doi: 10.1039/C5TA06041A.

[105] Byung-Jo Kim, Dong Hoe Kim, Yoo-Yong Lee, Hee-Won Shin, Gill Sang Han, Jung Sug Hong, Khalid Mahmood, T. Ahn, Young-Chang Joo, Kug Sun Hong, Nam-Gyu Park, Sangwook Lee, and Hyun Suk Jung. Highly efficient and

bending durable perovskite solar cells: toward wearable power source. *Energy Environ. Sci.*, 8(3):Advance, 2015. ISSN 1754-5692. doi: 10.1039/C4EE02441A.

[106] Weiran Zhou, Jieming Zhen, Qing Liu, Zhimin Fang, Dan Li, Pengcheng Zhou, Tao Chen, and Shangfeng Yang. Successive surface engineering of TiO2 compact layers via dual modification of fullerene derivatives affording hysteresis-suppressed high-performance perovskite solar cells. *J. Mater. Chem. A*, 5(4):1724–1733, 2017. ISSN 2050-7488. doi: 10.1039/C6TA07876A.

[107] Jay B Patel, Jennifer Wong-Leung, Stephan Van Reenen, Nobuya Sakai, Jacob Tse Wei Wang, Elizabeth S Parrott, Mingzhen Liu, Henry J Snaith, Laura M Herz, and Michael B Johnston. Influence of Interface Morphology on Hysteresis in Vapor-Deposited Perovskite Solar Cells. *Advanced Electronic Materials*, page 1600470, 2016. doi: 10.1002/aelm.201600470.

[108] Konrad Wojciechowski, Tomas Leijtens, Svetlana Siprova, Christoph Schlueter, Maximilian T. Hörantner, Jacob Tse Wei Wang, Chang Zhi Li, Alex K Y Jen, Tien Lin Lee, and Henry J. Snaith. C60 as an efficient n-type compact layer in perovskite solar cells. *Journal of Physical Chemistry Letters*, 6(12):2399–2405, 2015. ISSN 19487185. doi: 10.1021/acs.jpclett.5b00902.

[109] Ludmila Cojocaru, Satoshi Uchida, Yoshitaka Sanehira, Jotaro Nakazaki, Takaya Kubo, and Hiroshi Segawa. Surface treatment of the compact TiO2 layer for efficient planar heterojunction perovskite solar cells. *Chem. Lett.*, 44(5):674–676, 2015. ISSN 0366-7022. doi: 10.1246/cl.150068.

[110] Hairen Tan, Ankit Jain, Oleksandr Voznyy, Xinzheng Lan, F. Pelayo Garcia de Arquer, James Fan, Rafael Quintero-Bermudez, Mingjian Yuan, Bo Zhang, Yicheng Zhao, Fengjia Fan, Peicheng Li, Li Na Quan, Yongbiao Zhao, Zheng-hong Lu, Zhenyu Yang, Sjoerd Hoogland, and Edward H Sargent. Efficient and stable solution-processed planar perovskite solar cells via contact passivation. *Science*, 726(February):722–726, 2017. ISSN 0036-8075. doi: 10.1126/science.aai9081.

[111] Feilong Cai, Liyan Yang, Yu Yan, Jinghui Zhang, Fei Qin, Dan Liu, Yi-bing Cheng, Yinhua Zhou, and Tao Wang. Eliminated hysteresis and stabilized power output over 20% in planar heterojunction perovskite solar cells by compositional and surface modifications to the low-temperature-processed TiO2 layer. *J. Mater. Chem. A*, 5(19):9402–9411, 2017. ISSN 2050-7488. doi: 10.1039/C7TA02317K.

[112] Jiangang Hu, Ronen Gottesman, Laxman Gouda, Adi Kama, Maayan Priel, Shay Tirosh, Juan Bisquert, and Arie Zaban. Photovoltage Behavior in

Perovskite Solar Cells under Light-Soaking Showing Photoinduced Interfacial Changes. *ACS Energy Letters*, 2(5):950–956, may 2017. ISSN 2380-8195. doi: 10.1021/acsenergylett.7b00212.

[113] Qiliang Wu, Weiran Zhou, Qing Liu, Pengcheng Zhou, Tao Chen, Yalin Lu, Qiquan Qiao, and Shangfeng Yang. Solution-Processable Ionic Liquid as an Independent or Modifying Electron Transport Layer for High-Efficiency Perovskite Solar Cells. *ACS Applied Materials & Interfaces*, page acsami.6b12683, 2016. ISSN 1944-8244. doi: 10.1021/acsami.6b12683.

[114] Agnese Abrusci, Samuel D. Stranks, Pablo Docampo, Hin Lap Yip, Alex K Y Jen, and Henry J. Snaith. High-performance perovskite-polymer hybrid solar cells via electronic coupling with fullerene monolayers. *Nano Letters*, 13(7): 3124–3128, 2013. ISSN 15306984. doi: 10.1021/nl401044q.

[115] Konrad Wojciechowski, Ivan Ramirez, Therese Gorisse, Olivier Dautel, Raghunath Dasari, Nobuya Sakai, Josue Martinez Hardigree, Seulki Song, Seth Marder, Moritz Riede, Guillaume Wantz, and Henry J. Snaith. Cross-Linkable Fullerene Derivatives for Solution-Processed n-i-p Perovskite Solar Cells. *ACS Energy Letters*, 1(4):648–653, oct 2016. ISSN 2380-8195. doi: 10.1021/acsenergylett.6b00229.

[116] Marta Valles-Pelarda, Bruno Clasen Hames, Ines Garcia-Benito, Osbel Almora, Agustin Molina-Ontoria, Rafael S. Sanchez, German Garcia-Belmonte, Nazario Martin, and Ivan Mora-Sero. Analysis of the Hysteresis Behavior of Perovskite Solar Cells with Interfacial Fullerene Self-Assembled Monolayers. *Journal of Physical Chemistry Letters*, 7(22):4622–4628, 2016. ISSN 19487185. doi: 10.1021/acs.jpclett.6b02103.

[117] Yanjun Fang, Cheng Bi, Dong Wang, and Jinsong Huang. The Functions of Fullerenes in Hybrid Perovskite Solar Cells. *ACS Energy Letters*, 2(4):782–794, apr 2017. ISSN 2380-8195. doi: 10.1021/acsenergylett.6b00657.

[118] Dong Yang, Ruixia Yang, Jing Zhang, Zhou Yang, Shengzhong (Frank) Liu, and Can Li. High efficiency flexible perovskite solar cells using superior low temperature TiO2. *Energy Environ. Sci.*, 8(11):3208–3214, 2015. ISSN 1754-5692. doi: 10.1039/C5EE02155C.

[119] Francesco Di Giacomo, Azhar Fakharuddin, Rajan Jose, and Thomas M Brown. Progress, challenges and perspectives in flexible perovskite solar cells. *Energy Environ. Sci.*, 9(9):3007–3035, 2016. ISSN 1754-5692. doi: 10.1039/c6ee01137c.

[120] Seungchan Ryu, Jangwon Seo, Seong Sik Shin, Young Chan Kim, Nam Joong Jeon, Jun Hong Noh, and Sang Il Seok. Fabrication of metal-oxide-free CH3NH3PbI3 perovskite solar cells processed at low temperature. *Journal of Materials Chemistry A*, 3(7):3271–3275, 2015. ISSN 2050-7496. doi: 10.1039/C5TA00011D.

[121] Yasmina Dkhissi, Fuzhi Huang, Sergey Rubanov, Manda Xiao, Udo Bach, Leone Spiccia, Rachel a. Caruso, and Yi Bing Cheng. Low temperature processing of flexible planar perovskite solar cells with efficiency over 10%. *Journal of Power Sources*, 278:325–331, 2015. ISSN 03787753. doi: 10.1016/j.jpowsour.2014.12.104.

[122] Hasitha C. Weerasinghe, Yasmina Dkhissi, Andrew D. Scully, Rachel a. Caruso, and Yi Bing Cheng. Encapsulation for improving the lifetime of flexible perovskite solar cells. *Nano Energy*, 18:118–125, 2015. ISSN 22112855. doi: 10.1016/j.nanoen.2015.10.006.

[123] John Ciro, Santiago Mesa, Juan Felipe Montoya, José Ignacio Uribe, Rafael Betancur, and Franklin Jaramillo. Simultaneous Top and Bottom Perovskite Interface Engineering by Fullerene Surface Modification of Titanium Dioxide as Electron Transport Layer. *ACS Applied Materials & Interfaces*, 9(35): 29654–29659, sep 2017. ISSN 1944-8244. doi: 10.1021/acsami.7b06343. URL http://pubs.acs.org/doi/abs/10.1021/acsami.7b06343.

[124] Henry J Snaith, Antonio Abate, James M Ball, Giles E Eperon, Tomas Leijtens, Nakita K Noel, Samuel D Stranks, Jacob Tse-wei Wang, Konrad , and Wei Zhang. Anomalous Hysteresis in Perovskite Solar Cells. *The Journal of Physical Chemistry Letters*, 5:1511–1515, 2014.

[125] J.A Christians, J.S Manser, and P.V Kamat. Best Practices in Perovskite Solar Cell E fficiency Measurements. Avoiding the Error of Making Bad Cells Look Good. *J. Phys. Chem. Lett*, 6:852–857, 2015. doi: 10.1021/acs.jpclett.5b00289.

[126] Bert Conings, Aslihan Babayigit, Matthew T. Klug, Sai Bai, Nicolas Gauquelin, Nobuya Sakai, Jacob Tse Wei Wang, Johan Verbeeck, Hans Gerd Boyen, and Henry J. Snaith. A Universal Deposition Protocol for Planar Heterojunction Solar Cells with High Efficiency Based on Hybrid Lead Halide Perovskite Families. *Advanced Materials*, pages 1–9, 2016. ISSN 15214095. doi: 10.1002/adma.201603747.

[127] Jing Liqiang, Sun Xiaojun, Shang Jing, Cai Weimin, Xu Zili, Du Yaoguo, and Fu Honggang. Review of surface photovoltage spectra of nano-sized semiconductor and its applications in heterogeneous photocatalysis. *Solar Energy*

Materials and Solar Cells, 79(2):133–151, 2003. ISSN 09270248. doi: 10.1016/S0927-0248(02)00393-8.

[128] Nakita K. Noel, Severin N. Habisreutinger, Bernard Wenger, Matthew T. Klug, Maximilian T. Hörantner, Michael B. Johnston, Robin J. Nicholas, David T. Moore, and Henry J. Snaith. A low viscosity, low boiling point, clean solvent system for the rapid crystallisation of highly specular perovskite films. *Energy Environ. Sci.*, 10(1):145–152, 2017. ISSN 1754-5692. doi: 10.1039/C6EE02373H. URL http://xlink.rsc.org/?DOI=C6EE02373H.

[129] Nirmal Adhikari, Ashish Dubey, Eman A. Gaml, Bjorn Vaagensmith, Khan Mamun Reza, Sally Adel Abdelsalam Mabrouk, Shaopeng Gu, Jiantao Zai, Xuefeng Qian, and Qiquan Qiao. Crystallization of a perovskite film for higher performance solar cells by controlling water concentration in methyl ammonium iodide precursor solution. *Nanoscale*, 8(5):2693–2703, 2016. ISSN 2040-3364. doi: 10.1039/C5NR06687E. URL http://xlink.rsc.org/?DOI=C5NR06687E.

[130] Namyoung Ahn, Dae Yong Son, In Hyuk Jang, Seong Min Kang, Mansoo Choi, and Nam Gyu Park. Highly Reproducible Perovskite Solar Cells with Average Efficiency of 18.3% and Best Efficiency of 19.7% Fabricated via Lewis Base Adduct of Lead(II) Iodide. *Journal of the American Chemical Society*, 137(27): 8696–8699, 2015. ISSN 15205126. doi: 10.1021/jacs.5b04930.

[131] Yani Chen, Yixin Zhao, and Ziqi Liang. Non-thermal annealing fabrication of efficient planar perovskite solar cells with inclusion of NH4Cl. *Chemistry of Materials*, 27(5):1448–1451, 2015. ISSN 15205002. doi: 10.1021/acs.chemmater.5b00041.

[132] Nam Joong Jeon, Jun Hong Noh, Young Chan Kim, Woon Seok Yang, Seungchan Ryu, and Sang Il Seok. Solvent engineering for high-performance inorganicâorganic hybrid perovskite solar cells. *Nature*, 13(September):897–903, 2014. doi: 10.1038/NMAT4014.

[133] Susanne T Birkhold, Eugen Zimmermann, Tom Kollek, Daniel Wurmbrand, Sebastian Polarz, and Lukas Schmidt-mende. Impact of Crystal Surface on Photoexcited States in Organic-Inorganic Perovskites. *Advanced Functional Materials*, 27:1604995, 2017. doi: 10.1002/adfm.201604995.

[134] Jae S. Yun, Anita Ho-Baillie, Shujuan Huang, Sang H. Woo, Yooun Heo, Jan Seidel, Fuzhi Huang, Yi-Bing Cheng, and Martin A. Green. Benefit of Grain Boundaries in OrganicâInorganic Halide Planar Perovskite Solar Cells. *The Journal of Physical Chemistry Letters*, 6(5):875–880, mar 2015. ISSN 1948-7185.

doi: 10.1021/acs.jpclett.5b00182. URL http://pubs.acs.org/doi/abs/10.1021/acs.jpclett.5b00182.

[135] John Ciro, Mario Alejandro Mejía-escobar, and Franklin Jaramillo. Slot-die processing of flexible perovskite solar cells in ambient conditions. *Solar Energy*, 150:570–576, 2017. ISSN 0038-092X. doi: 10.1016/j.solener.2017.04.071. URL http://dx.doi.org/10.1016/j.solener.2017.04.071.

[136] Dane W. DeQuilettes, Susanne Koch, Sven Burke, Rajan K. Paranji, Alfred J. Shropshire, Mark E. Ziffer, and David S. Ginger. Photoluminescence Lifetimes Exceeding 8 μs and Quantum Yields Exceeding 30% in Hybrid Perovskite Thin Films by Ligand Passivation. *ACS Energy Letters*, 1(2):438–444, aug 2016. ISSN 2380-8195. doi: 10.1021/acsenergylett.6b00236. URL http://pubs.acs.org/doi/abs/10.1021/acsenergylett.6b00236.

[137] Benjamin Calesnick, Jens A. Christensen, and Mabel Richter. Human Toxicity of Various Oximes. *Archives of Environmental Health: An International Journal*, 15(5):599–608, nov 1967. ISSN 0003-9896. doi: 10.1080/00039896.1967.10664975. URL http://www.tandfonline.com/doi/abs/10.1080/00039896.1967.10664975.

[138] Samuel D Stranks, Giles E Eperon, Giulia Grancini, Christopher Menelaou, Marcelo J P Alcocer, Tomas Leijtens, Laura M Herz, Annamaria Petrozza, and Henry J Snaith. Electron-Hole Diffusion Lengths Exceeding. *Science*, 341(2013), 2014. doi: 10.1126/science.1243982.

[139] Eric T Hoke, Daniel J Slotcavage, Emma R Dohner, Andrea R Bowring, Hemamala I Karunadasa, and Michael D Mcgehee. Reversible photo-induced trap formation in mixedhalide hybrid perovskites for photovoltaics. *Chemical Science*, 6:613–617, 2014. ISSN 2041-6520. doi: 10.1039/C4SC03141E. URL http://dx.doi.org/10.1039/C4SC03141E.

[140] Fangzhou Liu, Qi Dong, Man Kwong Wong, Aleksandra B. Djurišić, Annie Ng, Zhiwei Ren, Qian Shen, Charles Surya, Wai Kin Chan, Jian Wang, Alan Man Ching Ng, Changzhong Liao, Hangkong Li, Kaimin Shih, Chengrong Wei, Huimin Su, and Junfeng Dai. Is Excess PbI2 Beneficial for Perovskite Solar Cell Performance? *Advanced Energy Materials*, 6(7):1502206, apr 2016. ISSN 16146840. doi: 10.1002/aenm.201502206. URL http://doi.wiley.com/10.1002/aenm.201502206.

[141] S Amelinckx, D Van Dyck, and J Van Landuyt. *Handbook of Microscopy Methods II*. ISBN 3527292802.

[142] Sascha Sadewasser and Thilo Glatzel. *Kelvin Probe Force Microscopy*, volume 1. 2012. ISBN 978-3-642-22565-9. doi: 10.1007/978-3-642-22566-6. URL http://link.springer.com/10.1007/978-3-642-22566-6.

[143] Leeor Kronik and Yoram Shapira. Surface photovoltage phenomena: theory , experiment , and applications. *Surface Science Reports*, 37:1–206, 1999.

[144] J D Wei, S F Li, A Atamuratov, H Wehmann, and A Waag. Photoassisted Kelvin probe force microscopy at GaN surfaces: The role of polarity Photoassisted Kelvin probe force microscopy at GaN surfaces : The role. *Applied Physics Letters*, 172111:97–100, 2010. doi: 10.1063/1.3511541.

[145] S Saraf and Y Rosenwaks. Local measurement of semiconductor band bending and surface charge using Kelvin probe force microscopy. *Surface Science Letters*, 574:L35–L39, 2005. doi: 10.1016/j.susc.2004.10.042.

[146] T Meoded, R Shikler, N Fried, Y Rosenwaks, T Meoded, R Shikler, N Fried, and Y Rosenwaks. Direct measurement of minority carriers diffusion length using Kelvin probe force microscopy Direct measurement of minority carriers diffusion length using Kelvin probe force microscopy. *Applied Physics Letters*, 2435(1999): 2–5, 2012. doi: 10.1063/1.125039.

[147] Alvin M Goodman. A Method for the Measurement of Short Minority Carrier Diffusion Lengths in Semiconductors. *Journal of Applied Physics*, 2550:2550, 1961. doi: 10.1063/1.1728351.

[148] Rajiv Giridharagopal, Phillip A. Cox, and David S. Ginger. Functional Scanning Probe Imaging of Nanostructured Solar Energy Materials. *Accounts of Chemical Research*, 49(9):1769–1776, 2016. ISSN 15204898. doi: 10.1021/acs.accounts.6b00255.